National Library of Canada
Bibliothèque nationale du Canada

Canadian Theses Service
Service des thèses canadiennes

Ottawa, Canada
K1A 0N4

NOTICE

The quality of this microform is heavily dependent upon the quality of the original thesis submitted for microfilming. Every effort has been made to ensure the highest quality of reproduction possible.

If pages are missing, contact the university which granted the degree.

Some pages may have indistinct print especially if the original pages were typed with a poor typewriter ribbon or if the university sent us an inferior photocopy.

Reproduction in full or in part of this microform is governed by the Canadian Copyright Act, R.S.C. 1970, c. C-30, and subsequent amendments.

AVIS

La qualité de cette microforme dépend grandement de la qualité de la thèse soumise au microfilmage. Nous avons tout fait pour assurer une qualité supérieure de reproduction.

S'il manque des pages, veuillez communiquer avec l'université qui a conféré le grade.

La qualité d'impression de certaines pages peut laisser à désirer, surtout si les pages originales ont été dactylographiées à l'aide d'un ruban usé ou si l'université nous a fait parvenir une photocopie de qualité inférieure.

La reproduction, même partielle, de cette microforme est soumise à la Loi canadienne sur le droit d'auteur, SRC 1970, c. C-30, et ses amendements subséquents.

NL-339 (r. 88/04) c

Canada

UNIVERSITY OF ALBERTA

THE NUMERICAL MODELLING OF SHEAR BANDS IN GEOLOGICAL MATERIALS

BY

© RICHARD G. WAN

A THESIS
SUBMITTED TO THE FACULTY OF GRADUATE STUDIES AND
RESEARCH IN PARTIAL FULFILMENT OF THE REQUIREMENTS FOR
THE DEGREE OF DOCTOR IN PHILOSOPHY

DEPARTMENT OF CIVIL ENGINEERING

EDMONTON, ALBERTA
FALL 1990

National Library of Canada
Bibliothèque nationale du Canada

Canadian Theses Service
Service des thèses canadiennes

Ottawa, Canada
K1A 0N4

The author has granted an irrevocable non-exclusive licence allowing the National Library of Canada to reproduce, loan, distribute or sell copies of his/her thesis by any means and in any form or format, making this thesis available to interested persons.

L'auteur a accordé une licence irrévocable et non exclusive permettant à la Bibliothèque nationale du Canada de reproduire, prêter, distribuer ou vendre des copies de sa thèse de quelque manière et sous quelque forme que ce soit pour mettre des exemplaires de cette thèse à la disposition des personnes intéressées.

The author retains ownership of the copyright in his/her thesis. Neither the thesis nor substantial extracts from it may be printed or otherwise reproduced without his/her permission.

L'auteur conserve la propriété du droit d'auteur qui protège sa thèse. Ni la thèse ni des extraits substantiels de celle-ci ne doivent être imprimés ou autrement reproduits sans son autorisation.

ISBN 0-315-64769-8

Canada

UNIVERSITY OF ALBERTA

RELEASE FORM

NAME OF AUTHOR: Richard G. WAN

TITLE OF THESIS: The Numerical Modelling of Shear-Bands in Geological Materials

DEGREE FOR WHICH THESIS WAS PRESENTED: Doctor of Philosophy

YEAR THIS DEGREE GRANTED: Fall 1990

Permission is hereby granted to THE UNIVERSITY OF ALBERTA LIBRARY to reproduce single copies of this thesis and to lend or sell such copies for private, scholarly or scientific research purposes only.

The author reserves other publication rights, and neither the thesis nor extensive extracts from it may be printed or otherwise reproduced without the author's written permission.

(SIGNED) Richard Wan

PERMANENT ADDRESS:
110-960 TERON Road
KANATA, ONTARIO
K2K 2B6 CANADA

DATE September 18, 1990

THE UNIVERSITY OF ALBERTA

FACULTY OF GRADUATE STUDIES AND RESEARCH

The undersigned certify that they have read, and recommend to the Faculty of Graduate Studies and Research for acceptance, a thesis entitled THE NUMERICAL MODELLING OF SHEAR-BANDS IN GEOLOGICAL MATERIALS submitted by RICHARD G. WAN in partial fulfilment of the requirements for the degree of Doctor of Philosophy.

.....
Dr. D.H Chan (Supervisor)

.....
Dr. N. R Morgenstern (Co-Supervisor)

.....
Dr. D. C Sego

.....
Dr. T. M Hrudey

.....
Dr. F. Ellyin

.....
Dr. S.T. Pietruszczak (External Examiner)

DATE September 14 1990

DEDICATION

To my parents...

ABSTRACT

The process of failure in geomaterials is very often characterized by the localization of inelastic deformations in the form of shear bands for ductile materials (clays) or micro-cracks for brittle materials (rocks and concrete). These aspects form the basis of the present thesis which blends theoretical analysis of rupture as a problem of bifurcation with numerical techniques such as the finite element method for its modelling.

The kinematics of deformation ensuing localization is described by conveniently modifying the variational statement, herein the principle of virtual work, to account for plastic dissipation along an internal discontinuity surface in the soil structure.

The framework, implemented into a finite element program, provides an important tool to model both inception and development of kinematic discontinuity surfaces without the need to re-mesh the grid. Specially designed finite elements with intrinsic discontinuities in their shape functions enhance the modelling of localization modes in the post-failure regime. These represent an improvement over standard finite elements which are notorious for suppressing localization effects such as jumps in field variables.

The numerical method has been tested with reference to benchmark problems. In particular, the problem of the indentation of a semi-infinite body by a rigid flat punch is attempted considering the spreading of a kinematic discontinuity surface. It is seen that bifurcation theory successfully predicts inception and inclination of the shear band. The progression of the shear band as it pervades through the mesh is traced. A simple Coulomb contact law, with the possibility of embracing features such as particle re-orientation or grain crushing, basically governs the shear band behaviour while the ambient material follows a perfectly plastic or softening von Mises type constitutive relationship. It is found that the resulting limit load is very much influenced by the shear band contact behaviour,

herein treated as purely cohesive. A consistently lower value than the one predicted by Prandtl's solution is obtained due to localization effects and discontinuous behaviour.

Finally, it can be said that the proposed method provides a promising framework within which the prediction of shear failure mechanisms in solid continua becomes possible through special finite element algorithms.

ACKNOWLEDGEMENT

I would like to express my deepest gratitude to my supervisors Drs. D.H Chan and N.R Morgernstern for their guidance, encouragement and most valuable advice during the course of this study.

Special thanks are due to my former professors in France and my best friend Dr. Amintore Fusco who opened up my mind to the world of research in engineering mechanics and taught me a discipline in method of working and "Cartesian" thinking.

Most importantly, I wish to thank my parents, for whom I am deeply indepted for their constant love, devotion and encouragement. They always assured me a good education and made lots of sacrifices.

During my stay in Alberta, I met many wonderful people on and off campus, and their friendship and understanding made my days here most memorable. In particular, I would like to thank my colleagues Dr. T. Wong, Prof. S. Tortike, Dr. N. Yoshida, Mr. M. Mathioudakis, Ms. A. Kupper and Dr. Lal Samarasekera.

The present work was funded by the Natural Sciences and Engineering Research Council of Canada and their support is gratefully acknowledged. The computing facilities were provided by the University of Alberta.

TABLE OF CONTENTS

Chapter 1

Introduction

1.1. Background 1

1.1.1. Localized deformation 1

1.1.2. Conventional methods of analysis 4

1.1.3. Bifurcation theory 6

1.2. Objectives and scopes 7

1.3. Organization of thesis 8

Chapter 2

Progressive Failure

2.1. Introduction 10

2.2 Finite element modelling of progressive failure 11

2.3. Rupture surfaces and methods of design 13

2.3.1. Historical background 13

2.3.2. Orientation of rupture/shear bands 16

Chapter 3

Localization as a Problem of Bifurcation

3.1. General 23

3.2 Localization of inelastic deformation 26
3.2.1 Kinematics of a shear band 26
3.2.2 Statical condition 27
3.2.3 Constitutive relationship 27
3.3 Continuous bifurcation 28
3.3.1 Bifurcation directions 29
3.4 Material model 32
3.4.1 Prandtl-Reuss material 33
3.4.2 Mohr-Coulomb material 34
3.4.3 Non-associated flow rule 35
3.5 Simple friction hardening model 36
3.5.1 Hardening law 36
3.5.2 Bifurcation surface 37
3.5.3 Shear band conditions under different stress configurations 39

Chapter 4
Numerical modelling of localization

4.1. Introduction 50
4.2. Softening damage 51
4.2.1 Localization instabilities 52
4.3 Consequences of using ordinary finite elements 53
4.4 Possible remedies 53
4.5 Proposed model 55
4.5.1 Problem formulation 57

4.5.2 Virtual work for displacement discontinuities 58
4.5.3 Incremental virtual work equations 59
4.5.4 Fluid flow through discontinuous medium 60
4.6 Finite element discretization 63
4.6.1 Displacement field interpolation 64
4.6.2 Pore fluid pressure field interpolation 65
4.7 Derivation of discontinuous interpolation functions 65
4.7.1 1-D discontinuous piecewise linear interpolation function 66
4.7.2 4-node discontinuous quadrilateral element QD4 67
4.8 Governing finite element equations 70
4.9 Convergence of enhanced strain field scheme 71
• Proof of stability 73
• Proof of consistency 74

Chapter 5

Constitutive Relationships

5.1. Preliminary Considerations 84
5.2. Rupture interface rheology 85
5.2.1 Experimental observations 85
5.3 Formulation of stress-relative displacement relationship 87
5.3.1 Phenomenological approaches 88
5.4 Plasticity formalism 90
5.4.1 Contact yield and plastic potential functions 90
5.4.2 Evolution rule 91
5.4.3 Elasto-plastic contact constitutive tensor 92

Chapter 6

Numerical Strategies

6.1. Introduction 100

6.2. Issues on model implementation 101

6.3. Compatational aspects of localization 103

6.3.1 Determination of a bifurcation point 106

6.3.2 Test problems 108

6.4 Numerical algorithm 109

Chapter 7

Numerical Results

7.1. Introduction 120

7.2. Numerical assessment of the method 120

7.2.1 Eigenvalue analysis 120

7.2.2 Patch test 123

7.3 Simple boundary value problems 126

7.3.1 Mini-footing problem 126

7.3.2 Mini-embankment problem 127

7.4 Rigid punch problem 128

7.4.1 Continuous case 128

7.4.2 Discontinuous case 129

Chapter 8

Conclusions and Recommendations

8.1 Conclusions.....151

8.2 Recommendations for future work.....153

References.....156

Appendix A

Derivation of Flow and Deformation Equations

A.1. Theory of mixtures.....163

A.2. Flow equations.....165

• Strong form.....165

• Mass conservation:.....165

• Darcean flow:.....166

•Boundary conditions:.....166

• Weak form : Problem statement:.....166

Variational statement:.....167

Appendix B

Numerical Implementation

B.1. Evaluation of composite element stiffness matrix.....169

B.2. Quadrature rule for element stiffness integration.....171

• Bulk stiffness $\mathbf{K}_{\Omega\Omega}^{(e)}$.....172

• Bulk-shear band interaction stiffnesses $\mathbf{K}_{\Omega S}^{(e)}$ and $\mathbf{K}_{S\Omega}^{(e)}$ 173

• Global shear band stiffness $\mathbf{K}_{SS}^{(e)}$ 173

B.3. Calculation of cartesian derivatives of shape functions.....173

B.4. Calculation of interface stiffness 175

B.5 Evaluation of load vectors.....177

LIST OF TABLES

Table 3.1 Direction of plastic strains under different stress conditions 49

Table 6.1 Solution algorithm for quartic equation 107

Table 6.2 J_2 flow plasticity 117

Table 6.3 Flow chart for localization problem algorithm 118

Table 7.1 Patch test solution for Figure 7.3 125

LIST OF FIGURES

CHAPTER 2

Figure 2.1 Stress-strain displacement curve for a direct shear box test.....18

Figure 2.2 Slip surfaces beneath a foundation: modified after Chazy & Habib[1961].....19

Figure 2.3 Lines of zero extension(velocity characteristics) in plane strain conditions.....20

Figure 2.4 Non-coaxiality of principal stress and strain increment directions.....21

Figure 2.5 Variation of dialatancy angle with friction angle for Toyoura sand: modified after Tatsuoka et al. [1990].....22

CHAPTER 3

Figure 3.1 Shear band in 3-D space.....42

Figure 3.2 Bifurcation modes in plane strain conditions for a von Mises material.....43

Figure 3.3 Bifurcation surface in stress space.....44

Figure 3.4 Stress-strain curve using Rowe's stress dilatancy equation.....45

Figure 3.5 Intersection of hardening modulus curve with bifurcation surface.....46

Figure 3.6 Variation of critical hardening modulus with stress ratio.....47

Figure 3.7 Variation of critical shear band orientation with stress ratio.....48

CHAPTER 4

Figure 4.1 Description of motion.....76

Figure 4.2 Fluid flow through discontinuous medium.....77

Figure 4.3 Finite element discretization of domain.....78

Figure 4.4a 1-D discontinuous interpolation function.....79

Figure 4.4b Distribution of displacement across a shear band.....79

Figure 4.5 Geometrical description of 1-D discontinuous interpolation shape function 80
Figure 4.6 Master element configuration for QD4 elements 81
Figure 4.7 Discontinuous shape functions for a 4-node quadrilateral element 82
Figure 4.8 Discontinuous interpolation function for a 3-node triangular element 83

CHAPTER 5

Figure 5.1 - Macroscopic schematization of shear flow inside a shear band 96
Figure 5.2 Non-uniform stress distribution inside a shear box: progressive failure 97
Figure 5.3 Stress-relative displacement relationship in a direct shear box 98
Figure 5.4 Generic representation of shear band in 2-D configuration 99

CHAPTER 6

Figure 6.1 Geometrical representation of shear band in 2-D situation 111
Figure 6.2 Schematic representation of finding shear band inclinations from bifurcation criterion 112
Figure 6.3 Non-uniform shear loading: On element test problem 113
Figure 6.4 Force-displacement curve for non-uniform shear loading 114
Figure 6.5 Evolution of the determinant of the acoustic tensor with loading history 115
Figure 6.6 Evolution of shear strains at Gauss points for homogeneous analysis 116

CHAPTER 7

Figure 7.1 Non-zero eigen-modes for shear band element QD4 (option 1) in plane strain 134
Figure 7.2 Eigen-modes for shear band element QD4 (option 2) 135
Figure 7.3 Patch of triangular discontinuous elements 136

Figure 7.4 Finite element schematization of slippage along shear band 137
Figure 7.5 Condition of displacement field compatibility at the junction between discontinuous and continuum elements.....138
Figure 7.6 Kinematics of embankment under shear band mode of deformation.....139
Figure 7.7 Distribution of internal tractions along shear band.....139
Figure 7.8 Contours of shear strains (%) as computed from proposed formulation.....139
Figure 7.9 Contours of shear strains (%) as computed from conventional finite element method formulation.....139
Figure 7.10 Rigid punch problem: finite element mesh 140
Figure 7.11 Load-displacement curve for rigid footing 141
Figure 7.12 Rigid punch problem: growth of plastic zone.....142
Figure 7.13 Constitutive relationship for strain-softening behaviour.....143
Figure 7.14 Constitutive law for shear band 144
Figure 7.15 Progression of shear band during loading history 145
Figure 7.16 Kinematics of rigid punch problem using proposed method.....146
Figure 7.17 Evolution of slip displacement along shear band with loading history.....147
Figure 7.18 Variation of shear resistance along shear band.....148
Figure 7.19 Load-displacement curve for rigid footing with localization 149
Figure 7.20 Effective plastic strain for element 44 below left hand corner of footing.....150

Appendix B

Figure B.1 Structure of typical stiffness matrix for a shear band element.....179
Figure B.2 Smearing effect for normal quadrature rule 180
Figure B.3 Dual mapping technique for numerical integration 181
Figure B.4 Shear band geometry in global and local coordinate systems 182
Figure B.5 Integration of loads along a discontinuous edge.....183

LIST OF SYMBOLS

$\mathbf{B}^{(\alpha)}$, $\mathbf{B}^{(\beta)}$,	compatibility matrices for continuous and discontinuous interpolation polynomials
$\mathbf{B}^{ll}$	compatibility matrix for pore fluid pressure
c_d	characteristic cohesive strength for discontinuity surface
d_b	shear band thickness
e	void ratio
$\mathbf{E}$	tensor of incremental elastic moduli
F	yield function
F_d	yield function for discontinuity surface
G	plastic potential function
$\mathbf{a}$	vector representing jump in an arbitrary field
g_i	ith component of slip displacement
g_n^p, g_t^p	normal and tangential plastic slip displacements
G_d	elastic shear modulus for discontinuity
$\mathbf{H}$	matrix of interpolation polynomials for pore fluid pressure
H	plastic hardening modulus
H_{cri}	critical plastic hardening modulus
K_d	elastic bulk modulus for discontinuity
L_{ijkl}	(i,j,k,l)-component of fourth order tensor for stress-strain relationship
$\mathcal{L}_1$, $\mathcal{L}_2$, $\mathcal{L}_3$	area coordinates for triangular element mapping
$\mathbf{n}$	normal vector to a given plane in space
$\mathbf{N}^{(\alpha)}$, $\mathbf{N}^{(\beta)}$,	matrices of continuous and discontinuous interpolation polynomials for the displacement field

$\mathbf{P}, \mathbf{Q}$	metric tensors representing plastic strain directions and normals to yield surface respectively
s_{ij}	(i,j)-component of deviatoric stress tensor
t_i^1	internal stress vector at surface discontinuity
$\mathbf{t}^{\prime 1}$	*effective* internal stress vector at surface discontinuity
$u_{i,j}$	(i,j)-component of displacement gradient tensor
v_i	i^{th} component of fluid velocity

Greek symbols

α	Biot's coefficient representing degree of pore fluid saturation
α_f	bedding plane angle with respect to minor in-situ principal stress direction
δ_{ij}	Kronecker delta
ε_{ij}	(i,j)-component of strain tensor
$\dot{\varepsilon}_1, \dot{\varepsilon}_2, \dot{\varepsilon}_3$	principal strain rates
$\bar{\varepsilon}^p$	effective plastic strains
$\dot{\boldsymbol{\varepsilon}}^p$	plastic strain rate
Γ_{sb}	surface area delimiting shear band
$\boldsymbol{\gamma}$	gravity force vector
γ^p	accumulated plastic strains
φ	friction angle
φ_d	characteristic friction angle for discontinuity surface
φ_m , φ_f , φ_{cv}	mobilized, failure, and constant volume friction angles
η_{ij}	(i,j)-component of second order contact constitutive tensor for discontinuity surface
k_{ij}	(i,j)-component of fluid conductivity tensor

$\Lambda,$	Lame's coefficient
ν	Poission ratio
π	pore fluid pressure
$\overline{\pi}, \pi^*$	nodal and hydraulically admissible pore fluid pressures
σ_{ij}	(i,j)-component of stress tensor
σ'_{ij}	(i,j)-component of the *effective* stress tensor
σ_{kk}	trace of stress tensor
σ_y^0	uniaxial yield strength
$\sigma_1, \sigma_2, \sigma_3$	principal stress tensor
ξ, η	natural coordinates for finite element mapping
Ω	elemental volume
ω	bifurcation direction
Ψ	dilatancy angle
Ψ_d	characteristic dilatancy angle for discontinuity surface

Chapter 1

Introduction

1.1. Background

1.1.1. Localized deformation

The localization of deformation is both a fascinating and widely observed phenomenon occurring in the behaviour of engineering materials. The study of this behaviour is of particular interest in geotechnical engineering since the development of shear bands of concentrated deformation leads to sudden failure and collapse of the structure. Also, interest in localization stems from the fact that it occurs in a diverse range of solids comprising ductile single crystals, structural metals, saturated clays, rocks, concrete and even cereal grains.

In the realm of geotechnical engineering, discrete surfaces with controlling kinematic discontinuities manifest themselves at both field and laboratory scales. Well known practical examples for instance involve failure governed by the initiation and propagation of rupture surfaces or shear/slip bands in slopes, foundations, boreholes and underground openings. In the area of laboratory testing, a similar phenomenon is observed when imposing a uniform stress or strain field on an almost homogeneous soil sample. In fact, as external boundary conditions are kept unchanged one encounters an abrupt shift from an initial homogeneous deformation pattern to one involving localization into a narrow

band inside which material strength and microfabric degrade. Subsequent damage confined within the band would then eventually collapse into a well-defined failure plane.

In trying to pursue an investigation into localization, it is important to introduce a definition in order to provide some background to the present thesis. Consider a body subjected to a homogeneous loading history, proportional loading for example. It is quite obvious that the response will be of the trivial mode concerned with diffuse deformation within the body. As a result, plastic deformations occur simultaneously all over the solid in a homogeneous fashion. However, it may be possible due to severity of loading conditions and prominence of inelastic deformations—shear dilatancy for geomaterials—that at a given stress level, a new mode sets in and supersedes the original trivial mode. This so-called localized mode involves the emergence of a typical pattern in the form of either a narrow band of intense straining or clusters of micro-cracks, depending upon material ductility.

The foregoing observations suggest that this very local material phenomenon emerges as an outcome of the constitutive behaviour, but not kinematically imposed boundary conditions. Although several other factors such as the effect of rate dependence, geometry, discontinuous boundary conditions and material imperfections could be possibly considered, it is frequent that localization arises mainly because the constitutive law becomes unstable or bifurcates. This bifurcation can be triggered by a local vertex or a global corner in the geometry of the loading surface. The ensuing instability is then usually exhibited by a falling stress-strain curve with a negative or softening plastic modulus.

Instability caused by softening—the transition from the rising part of the stress-strain curve to the falling branch—can be easily accommodated in any yield surface formulation from a plasticity point of view. However, the most important question to be asked is whether the experimentally observed falling stress-strain curve is really a material instability, or is it an artifact of the experimental set up as a result of the build up of non-homogeneity as the shear band forms. There is no definite and satisfactory answer to the question, but in many circumstances it appears that the real situation will lie somewhere in

between, i.e. softening may be attributed partly due to experimental set up, and partly due to material behaviour.

In order to gain some insight into the various driving mechanisms leading to instability, what happens in granular and cohesive materials can be selected as basis of study. The processes governing the deformation of a granular material can be grossly described by two major hardening mechanisms: deviatoric and isotropic. The combination of those two mechanisms, each one of which having interacting effects on the strength of the material, replicate the observed response.

The hardening mechanism coming from the shearing component may be used to explain localization. During the evolution of the deviatoric loading, the microstructure undergoes damage in the form of dilation and grain crushing, both easily quantified by measuring the void ratio. It is by nature that this process is very prone to lead to concentration of deformation in the sense that accumulation of damage takes place in a restricted part of the medium as opposed to a general diffusion over the domain.

In a triaxial sample of dense material, it is conceivable that zones of accumulation of damage or dilation will form. At this point, this causes the overall bulk density to be lower than the original one and leads to a general loss in strength. The process which has been just described cannot take place in an arbitrary manner. The localized mode must satisfy boundary conditions and equilibrium both in the sense of kinematics and statics. As such, this implies that localization cannot be confined and must traverse the sample, i.e. shear banding occurs.

The process of localized deformation in clays may be quite different from what has been just described for granular materials. The driving mechanism behind localization may emanate from particle re-orientation and re-structuring in the micro-fabric. In rather homogeneous heavily overconsolidated clay samples loaded in triaxial compression or extension, softening response can be observed before any shear band forms to an

appreciable degree. This can be explained by means of energy release occurring as interparticle bonds break during dilation.

Modelling localized deformations in computational geomechanics has now become a major concern and challenge in the failure analysis of engineering structures for several reasons. While post peak behaviour may be an important aspect of problems with dominant kinematics, it also involves localized deformation with a dual significance: precursor to failure and a mechanism to large strain plastic response. Thus, accurate computations through proper formulations containing bifurcating theoretical representations are necessary in the evaluation of the ultimate capacity of structures containing shear bands.

It is usually possible to categorize field discontinuity surfaces under two main classes: pre-existing old slip surfaces and joints in the soil or rock mass, and non-predefined discontinuity surfaces as those occurring in shear bands. In the latter case, no information is given on initiation and development as loading of the structure progresses with time. Numerical treatment of discontinuities of the first kind—those geologically predefined—is fairly straightforward. Slippage at the discontinuity interface can be explicitly accounted for in the analysis by means of numerical artifacts such as the joint element, see Goodman et al. [1968]. While it is fairly easy to model discontinuities when their locations are known in advance, it is in contrast certainly important to recognize difficulties inherent in tracing shear band development in a general case. Understanding concerning both details of proper formulation of field equations and numerical implementation are yet to emerge. Some of the major concerns involve issues on formulation of governing field equations with inherent discontinuities including kinematics, discretization and linearization.

1.1.2. Conventional methods of analysis

Design tools conventionally used by the geotechnical engineer often reduce to limit equilibrium analysis whereby a mode of failure is postulated in which one or more rupture

surfaces form. While the use of a local stress-strain relationship is precluded, overall equilibrium is merely satisfied with a yield condition along the prescribed discontinuity surface. By examining a number of different mechanisms, the most critical one is chosen for which the loading is taken to be the limit equilibrium collapse load. In this respect, the limit equilibrium method is like an upper bound calculation in that it considers a mechanism of collapse. The exact collapse load in reality will be less than the one computed and may be unconservative considering other possible sources of errors. If one tries to model progressive failure using the method, a major shortcoming arises when considering limit failure of the material since the yield condition has to be prescribed simultaneously at all locations along the slip surface. Another limitation pertains to stresses and deformations in the following respects: firstly, equilibrium of internal stresses in the mass cannot be fully guaranteed since equilibrium is sought by means of resultant forces, and secondly, deformation of the sliding mass cannot be modelled. In brief, perhaps one may say that since trial mechanisms need to be prescribed, the analysis heavily involves engineering judgement, and excludes any sound understanding of the underlying principles in the quest for a practical solution.

An attempt at an improved analysis is the use of the finite element method which is more versatile in obtaining a solution for the deformation analysis of a field boundary value problem with appropriate constitutive laws other than elasticity or perfect plasticity. An outlook on the constitutive modelling literature indicates that the trend is towards the mathematical description of non-standard effects such as anisotropy, principal stress rotations during cyclic loading and non-coaxiality of stress and strain increment tensors through phenomenological considerations. More attention, instead, has to be paid to the nature of the formulation which basically assumes overall homogeneous deformations. Consequently, the conventional technique can be proven to be a gross approximation, and hence quite inadequate in considering very local deformations. In fact, it is noted that

conventional finite elements tend to diffuse the shear band in the mesh and no discontinuity is captured since it has been smoothed out.

A possible remedy of the problem is to consider geometrical non-linearity through finite plasticity in which the deformation gradient contains higher order non-linear terms which predominate during the formation of a shear band. However, an appeal to finite plasticity reveals that the complexity of the formalism may be exceedingly laborious and unnecessary so as to detract from practicality. Another alternative aspect of the solution is to implicitly incorporate the presence of discontinuities, thus non-homogeneous deformations, in the formulations and introduce new algorithms in the computations in order to enhance the finite element analysis. This appears to be very attractive and may produce satisfactory solutions while maintaining the framework of classical finite element analysis.

1.1.3. Bifurcation theory

The theory of bifurcation borrowed from the classical fields of mechanics and applied mathematics has long been used in metal plasticity, and recently applied and extended to soils, in order to explain localized deformation. In this theory, localized deformation is associated with a material instability which translates into the emergence of a possible alternate mode of non-homogeneous deformation construed as the spontaneous loss of uniqueness of governing incremental equilibrium equations.

The analysis of localized deformation by means of bifurcation theory has many practical implications. It may give rise to more insight in the interpretation of element tests for the derivation of constitutive laws by accounting for effects of loss of homogeneity. Another implication is its use as a criterion to detect shear banding in a finite element analysis in which localization conditions can be checked point-wise (locally) through the tangential constitutive tensor during the deformation history. While the utilization of linear bifurcation theory can satisfactorily predict shear band direction and corresponding load

level, no mechanism is provided for estimating the shear band width and post bifurcation behaviour. Recent works by Muhlhaus and Vardoulakis [1987] stipulate the use of Cosserat based constitutive models in which an internal characteristic length is explicitly accounted for in the formulation by considering a polar medium with possibility of local microstructure rotation. The initiation point—geometrical point where the shear band starts—in some cases can be pre-determined since they coincide with sites of either material weaknesses or obvious discontinuity in boundary conditions. However, in most cases the initiation point cannot be determined *a priori* and can only be unravelled by a micromechanical study of the material structure and local non-homogeneities.

1.2. Objectives and scopes

The objectives of this thesis can be summarized as follows:

1. to study localized deformations in geomaterials;
2. to review the existing theoretical and numerical literature. Theoretical developments would include plasticity, limit theorems, bifurcation in general and limit equilibrium methods. Numerical issues such as strain softening anisotropy, smeared band concepts and special FEM formulations will be investigated;
3. to develop a realistic and rational numerical model that captures localized deformation;
4. to identify relevant material constants associated with the model;
5. to implement the proposed model in numerical procedures such as the Finite Element method and demonstrate its capabilities with reference to well known benchmark problems.

1.3. Organization of thesis

The main thrust of this thesis is directed towards the establishment of a formalism for the description of physical processes that govern localized deformation in geomaterials. A rational numerical framework is thus developed.

In order to emphasize ideas and put them into perspective, it is convenient to start with a literature review of past and current available models and point out their respective drawbacks in handling localized deformation.

The phenomenon of progressive failure, a central feature in the deformation of geomaterials, is presented in Chapter 2 of this thesis. A brief historical sketch of classical theories of failure as well as underlying basic premises are presented. Frictional characteristics and inelastic volume changes are concomitant to geomaterials. The mechanism which triggers initiation of shear bands and their subsequent inclinations are then elucidated.

In Chapter 3 the problem of localization is cast in the framework of bifurcation theory. This chapter starts off with very simple examples to illustrate the fundamentals of bifurcation as a prelude to a subsequent mathematical description. The major emphasis of this chapter is on the mathematical derivations of bifurcation equations to describe localization. A criterion is thus obtained for the detection of localization and it is found to be very much dependent upon the constitutive law. As a matter of fact, the sensitivity of locating a bifurcation point is demonstrated when the criterion is subjected to subtle features such as non-associativity of plastic strains.

Until now, the adequacy of numerical models to capture localization is somewhat limited since most of them are based on a smeared approach whereby the localized deformation is averaged over the continuum. Chapter 4 summarizes the numerical techniques currently available and discusses the relative merits of each individual approach.

The mathematical framework for capturing shear bands is thus described. The approach adopted is the writing of a modified Principle of Virtual Work for deformations and fluid flow equations for a discontinuous medium. The development of appropriate discontinuous shape or interpolation functions in the discretization of the FEM equations basically completes the presentation of the model.

In Chapter 5, the issues on the proper description of the deformation response of a thin localized layer are addressed. Depending on the scale of investigation, the response is seemingly either of phenomenological or micromechanical nature. Various approaches are discussed briefly, and a simple phenomenological Coulomb type of law is proposed to simulate the behaviour of the shear band.

Chapter 6 discusses the implementation of the proposed formulation with particular reference to the numerical strategies adopted. Chapter 7 of this thesis is devoted to the testing of specially designed shear band elements with embedded discontinuous shape functions, and their ability to reproduce localized deformations is demonstrated. The element behaviour is examined in conditions of plane strain in an eigenvalue analysis and complemented by a patch test to check for both stability and consistency conditions. The analysis then moves on to a general boundary value problem—in particular the classical punch problem—to illustrate the performance of the model. Comparisons of predictions of the model with the conventional continuum based model are presented.

Findings of the model with regard to its deficiencies and strengths are given in Chapter 8. Conclusions and recommendations for future research are then outlined.

Chapter 2

Progressive Failure

2.1. Introduction

There has been considerable literature related to the topic of progressive failure in geotechnical engineering with particular emphasis on overconsolidated or shale-like clays, the occurrence of which has frequently caused serious economic losses as well as defying consistent prediction of time to and conditions for failure. Although 'progressive' is commonly thought of in the spatial sense, which is indeed also involved here, the phenomenon derives much of its pathology from the temporal aspect, Peck [1967], that failure of a soil mass takes place gradually with on-going time. A well known disturbing feature of progressive failure is that the applied or driving forces needed to cause failure of a soil medium is often much less than those apparently needed to mobilize the maximum shear strength of the soil everywhere along any assumed failure surface. Any discontinuity surface in the form of a rupture surface or a shear band introduces a non-uniform spatial strain and hence stress distribution with some degree of local concentration that degrades the strength from a critical peak value to a residual one as the material weakens with further straining. This "strain softening" behaviour is recognized to trigger a progressive mechanism failure. What happens in a direct shear box test clearly supports this view .

Skempton [1964] introduced the concept of residual strength by explaining the vital features of the stress-displacement curve obtained for weathered London clay, an uncemented overconsolidated material, in a direct shear box test, see Fig. 2.1. The material is found to undergo considerable inelastic deformation before peak strength at or near which deformation becomes localized into a narrow band. Subsequent to localization, deformation is characterized by the amount of relative sliding (g) between the surfaces of this band. Beyond peak, the material undergoes strength degradation leading to a residual strength τ_r which can be adequately reproduced from results of ring-shear tests, Bishop et al. [1971]. The foregoing concept provides a physical basis for the observations made by Chazy and Habib [1961] regarding a bearing capacity problem for a foundation, see Fig. 2.2. It is convenient to consider discontinuity surfaces along which relative sliding take place.

There seems to be basically two necessary conditions for generation of progressive failure: soil brittleness and non-uniform straining. The way failure will propagate with further loading depends on the post-peak behaviour of the soil. If there is no post peak strength reduction, failure will propagate slowly as mobilized stresses in adjoining regions reach the available ultimate strength and yielding propagates in a diffuse manner. However, if the soil exhibits brittleness there will be a loss in strength with further straining. General failure will occur when the strength reduction in the post peak regions exceeds the increment in mobilized strength in the pre-peak regions. This will lead to a sudden instability, and large post-peak movements as a mechanism is formed.

2.2 Finite element modelling of progressive failure

The general procedure to model progressive failure mechanism in a stress analysis is to characterize the constitutive behaviour of the soil as strain softening. The procedures developed fall into three categories: elastic stress redistribution, brittle plastic models and elasto-plastic strain softening models.

The first attempt to numerically model progressive failure in soils was probably done by Lo and Lee[1973] who successfully modified conventional finite element analysis to predict stress levels in slopes cut in sensitive clays. Once failure had occurred, the elastic modulus was made to become negative and stresses were redistributed iteratively to the surrounding zones in an attempt to mimic the strain softening behaviour. A criticism of the model is that the arbitrary assignment of a negative elastic modulus once failure occurs does not necessarily portray the actual mechanism, i.e. plastic flow of the material.

The simplest possible model is the elastic brittle model whereby the peak strength is allowed to abruptly drop to a residual value. From a numerical aspect, the sudden drop in strength may cause a spurious release of energy which leads to instability. Also, the way the stresses are redistributed is still obscure, although perfect plasticity is used at residual strength.

Models with a negative hardening modulus as proposed by Nayak, Zienkiewicz[1972], Hoeg[1972], Prevost and Hoeg[1975a], and Chan[1985] are classical but can lead to serious theoretical and numerical questions as to objectivity and uniqueness. In fact, the tangent stiffness matrix may become negative definite for a strain softening material and validity of solutions, if any, may be questionable. General numerical instability reflected in difficulty of convergence becomes more prominent in strain softening. A theoretical treatment of strain softening has been performed by Prevost and Hoeg[1975b] who attempt to prove uniqueness of solution under special circumstances. The problem of non-uniqueness in the sense that there may be two or more possible equilibrium states in the solid revolves around the bifurcation theory, the object of Chapter 3.

The foregoing brief review of methods of analysis in geotechnical engineering shows the lack of consistency in concept and raises some fundamental issues as to basic physics and mechanisms. It is seen that a progressive failure mechanism does not in general lead to a diffuse type of plastic deformation but rather leads to localized deformation

into rupture surfaces or shear bands. This invariably suggests an analysis in which these features are taken into account, see for example Pietruszczak and Mroz[1981].

2.3. Rupture surfaces and methods of design

The failure of soils along well defined rupture surfaces is a concept that has been firmly recognized for several decades now and much of soil mechanics theory is based on it. During a fairly long history in soil mechanics, traditional methods of design have always hinged around the Mohr-Coulomb failure criterion which predicts the plane on which failure occurs. Moreover, geotechnical engineers have always relied on two basic strength parameters, i.e. cohesion c and friction angle φ as physical properties for design.

The forthcoming sections briefly sketch the role of rupture surfaces in different types of analyses and the evolution of the theory with time. This will set the background for building a rational framework and a formalism for localization.

2.3.1. Historical background

Coulomb [1773] in his celebrated analysis of the limiting equilibrium of soil wedges behind a retaining wall, regarded his formula as an assumption expressing limiting shear stresses on a hypothetical failure plane. This problem, one of the earliest in kind, is a good example in which underlying concepts and physical processes involve localization of deformation in the form of a rupture surface.

Statical equilibrium of the sliding wedge is satisfied by equating the force which should be exerted on the wall so as to counteract forces due to gravity and mobilization of both friction and cohesion. By trying several wedge configurations, the minimum force is searched. A similar approach is followed for the case of passive pressure wherein the wall is pushed into the soil.

A critical look at the analysis reveals limitations in the method. Firstly, the wedge is considered rigid in the analysis, even though deformations may be very small. While the

calculations are carried out on resultant forces, local equilibrium of internal stresses is not ensured. In this respect, the limit force or load found is larger than the actual one, and thus can be considered as an upper-bound solution based on the global principle of limit equilibrium. More importantly in a different context, nowhere in the analysis is ever considered the spreading of plastic flow as localization initiates and propagates along rupture surfaces.

Rankine in 1857 goes on to analyze a purely frictional material for planes of maximum stress obliquity and established limiting zones of active and passive pressures. Sokolovski [1965] determined the stress distribution in zones of limiting equilibrium under specified two-dimensional boundary geometry and loadings. The solution includes a map of lines indicating the planes, as prescribed by Mohr-Coulomb stress conditions, on which slip may occur. Those lines, referred as stress characteristics may be regarded as planes of incipient failure.

The direction of failure and the velocity (or displacement) field have not been considered so far. In order to get the required velocities and strain rates, the missing link is established by making an assumption on the relative directions of stress and strain rates at incipient yield. One then stipulates the existence of a plastic potential from which the plastic strain rates can be derived. This surface being different from the yield (loading) surface in the stress space leads to the theory of non-associated plasticity. However, it is well known that the coincidence of the yield surface with the plastic potential bears fundamental consequences on postulates set by Drucker on convexity of the yield surface and normality of the plastic flow rule on the one hand, and Hill's principle of maximum work on the other hand.

Drucker's normality rule is well established for mainly pressure insensitive materials, i.e. metals, in the sense that it ensures mechanical stability. However for granular media such as geomaterials, the normality rule predicts too much dilation as compared with what is experimentally observed. The main reason for this discrepancy is

that normality leads to little dissipation, if not none at all (case of a purely frictional material) since most of the work is spent into producing dilation. As a result, the satisfaction of the normality rule would be awkward for a dissipative medium such as sand. In general, the strain rate vector must be corrected by making it normal to some other surface named as plastic potential surface derived from the amount of dissipation released by the material. It seems that Drucker's postulate is not reasonable and too restrictive when applied to soils. For instance, Mandel [1966] demonstrated that Drucker's postulate is a sufficient but not a necessary condition for a material to be stable. On the other hand, Lade et al. [1987] showed in the light of experiments that stability can still be achieved for stress controlled paths near ultimate state or failure. They basically found that the second order work remains positive although the plastic strain rate vector is non-associative.

The plastic potential for a granular material can be considered by introducing the dilatancy angle ψ which replaces the friction angle in the Mohr-Coulomb criterion. Bengt Hansen [1958] gives the following expression in plane strain conditions:

$$\sin \psi = -(\dot{\varepsilon}_1 + \dot{\varepsilon}_2) / (\dot{\varepsilon}_1 - \dot{\varepsilon}_2), \tag{2.1}$$

in which $\dot{\varepsilon}_1$ and $\dot{\varepsilon}_2$ are the in plane strain rates in directions 1 and 2 respectively. Using both the yield and plastic potential surfaces represented by Mohr-Coulomb and dilatancy equations respectively together with coaxiality of stress and infinitesimal strain increments, one ends up with a hyperbolic set of differential equations which satisfy equilibrium. The characteristics belonging to the set of partial differential equations are velocity characteristics showing directions of the velocity (displacement) field. In a rigid plastic situation with plastic strain rates derived from a plastic potential, one obtains two sets of characteristics namely stress and velocity which do not coincide. They would coincide in the case of associated plasticity whereby stress characteristics can be found such that, when

treated as velocity characteristics, they satisfy the boundary displacement conditions and a unique solution is obtained.

2.3.2. Orientation of rupture/shear bands

The determination of the shear band or rupture surface orientation is very important in the analysis of the statics and kinematics of a soil mass at failure. It will be interesting to discuss the possibilities to link the direction of the shear band to either a stress or velocity characteristic.

Stress characteristics are related to planes of maximum obliquity upon which the ratio of shear stress to the normal stress is maximum and where the ultimate strength has been reached. At failure, the planes are inclined at angles $\pm(\pi/4 - \varphi/2)$ to the direction of major principal stress σ_1. The angle of internal friction φ is defined as:

$$\varphi = \sin^{-1}\left(\frac{\sigma_1 - \sigma_3}{\sigma_1 + \sigma_3}\right)_{max}, \tag{2.2}$$

in which σ_3 is the minor principal stress. It is rather a conventional concept to make this so called Coulomb rupture plane coincide with the shear band. However, since the mechanism behind a shear band is usually of kinematical nature, it may be somewhat erroneous to consider tangents to stress characteristics as planes on which rupture takes place.

In certain circumstances, it may be more appropriate to treat the shear band as a velocity characteristic which bears a kinematic discontinuity in displacement gradient. It seems quite natural and logical to associate the shear band with velocity characteristics since both are related to a jump in displacement gradient. Thus the directions of no incremental strain (direction of zero extension) are inclined at $\pm(\pi/4 - \psi/2)$ to the direction of major principal strain increment $\dot{\varepsilon}_1$, see Fig. 2.3. The angle of dilation ψ at failure has been defined previously for plane strain conditions, see Eq. 2.1.

The association of the shear band orientation with lines of zero extension was suggested by Roscoe [1970] from experimental measures on a model retaining wall. Since rupture surfaces should logically follow velocity characteristics, then the question of coaxiality of stress and strain increment tensors is raised, if only one unique surface were to be considered. It seems that there may be deviation of $\pm(\varphi - \psi)/2$ between stress and strain rate tensors as illustrated in Fig. 2.4. The lines of zero extension (velocity characteristics) will exactly coincide with maximum stress obliquity lines (stress characteristics) only in the idealized case where the principal stress and strain increment directions are coaxial, i.e. $\varphi = \psi$. However, in practice the friction angle φ is much larger than the dilation angle at failure, see Tatsuoka et al. [1990] who reports a difference of the order of 28^{o} to 34^{o} for Toyoura sand, Fig. 2.5.

Many considerations enter into the determination of shear band orientations. Anisotropy may be an influencial factor since a sand mass deposited vertically exhibits significant anisotropy. It is therefore natural to consider that the shear band direction with respect to the direction of maximum stress obliquity plane and the zero extension direction be influenced by the inherent anisotropic fabric. This point is often ignored in the study of shear bands. Also, it is experimentally observed that the deviation from coaxiality of principal stress and strain increment tensors slowly decreases as one approaches failure. Therefore assuming coaxiality near failure is not a bad assumption. The direction of the shear band may also be controlled by boundary conditions, i.e. uniform stresses or displacement, or the size of the specimen. From those pertinent factors, the actual situation may not be simple. Thus at present, shear bands appearing in either the direction of maximum stress obliquity or of zero extension direction, or in the intermediate directions (as will be seen for the case of bifurcation theory in Chapter 3), is still an intensely controversial subject.

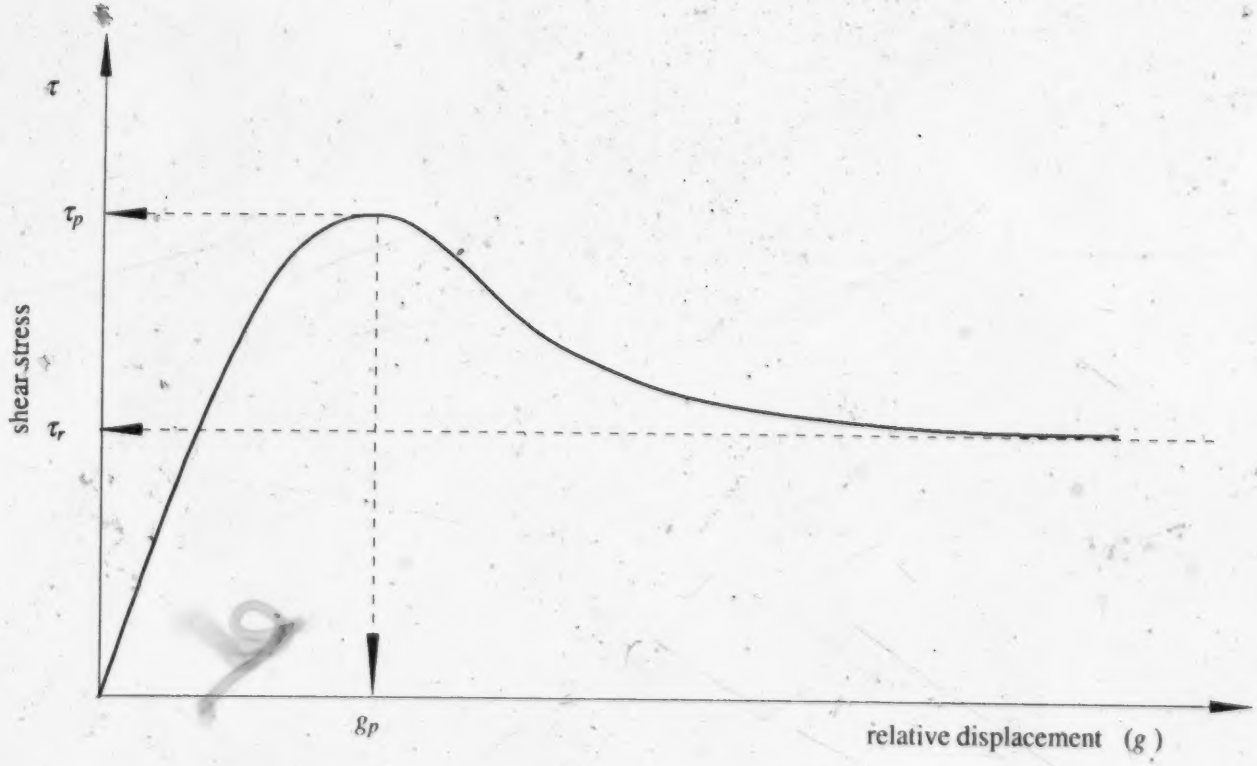

Figure 2.1 Stress-relative displacement curve for a direct shear box test

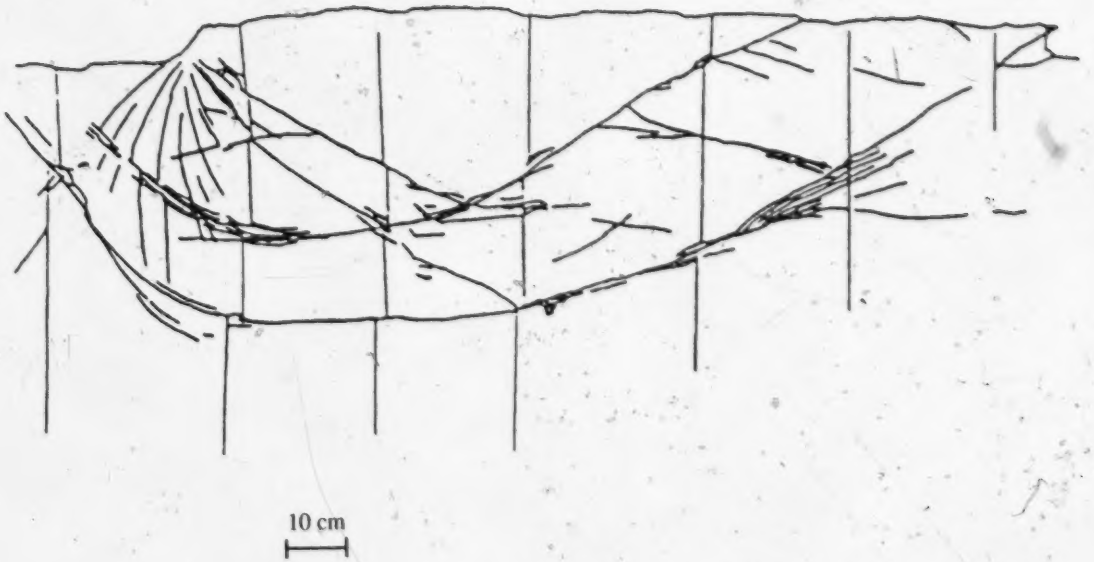

Figure 2.2 Slip surfaces beneath a foundation: modified after Chazy and Habib [1961].

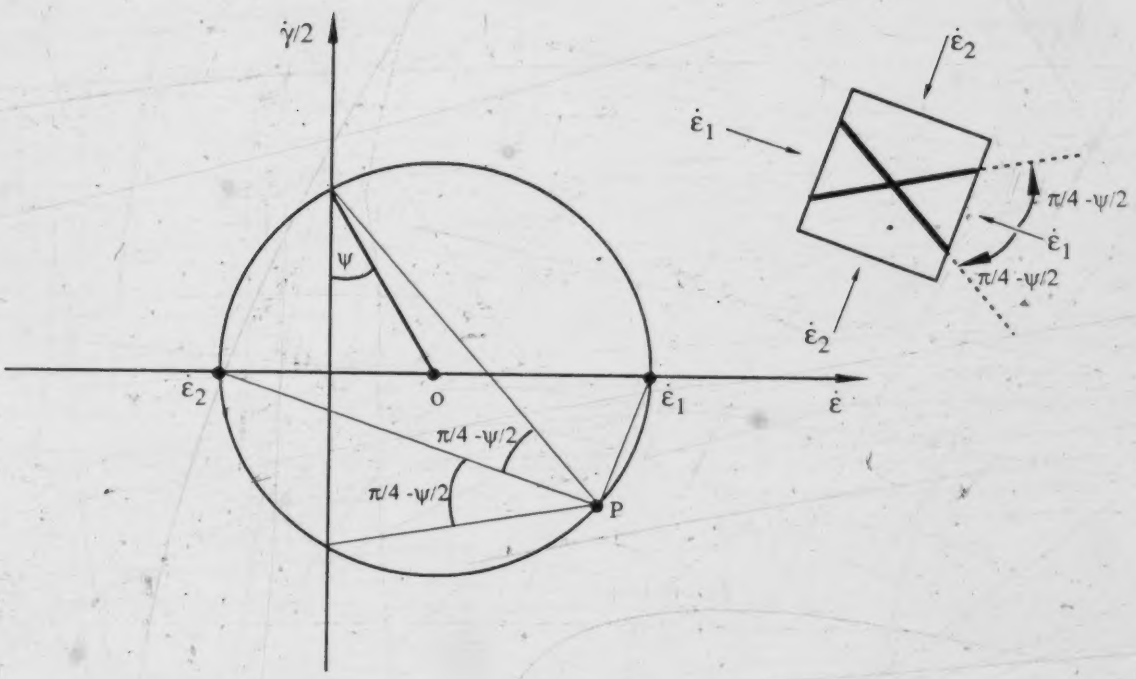

Figure 2.3 Lines of zero extension (velocity characteristics) in plane strain conditions

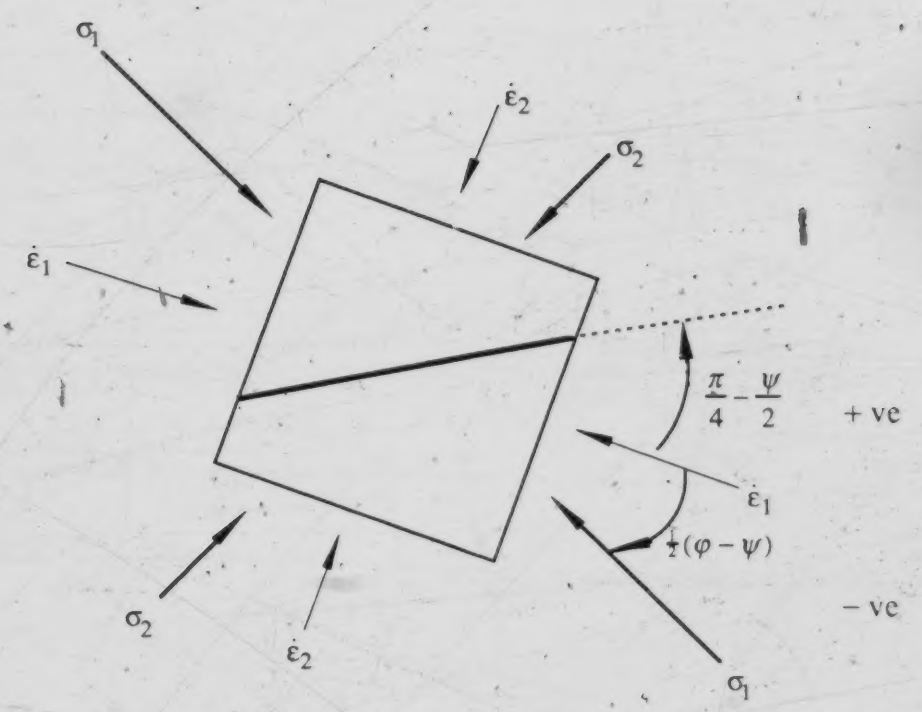

Figure 2.4 Non-coaxiality of principal stress and strain increment directions

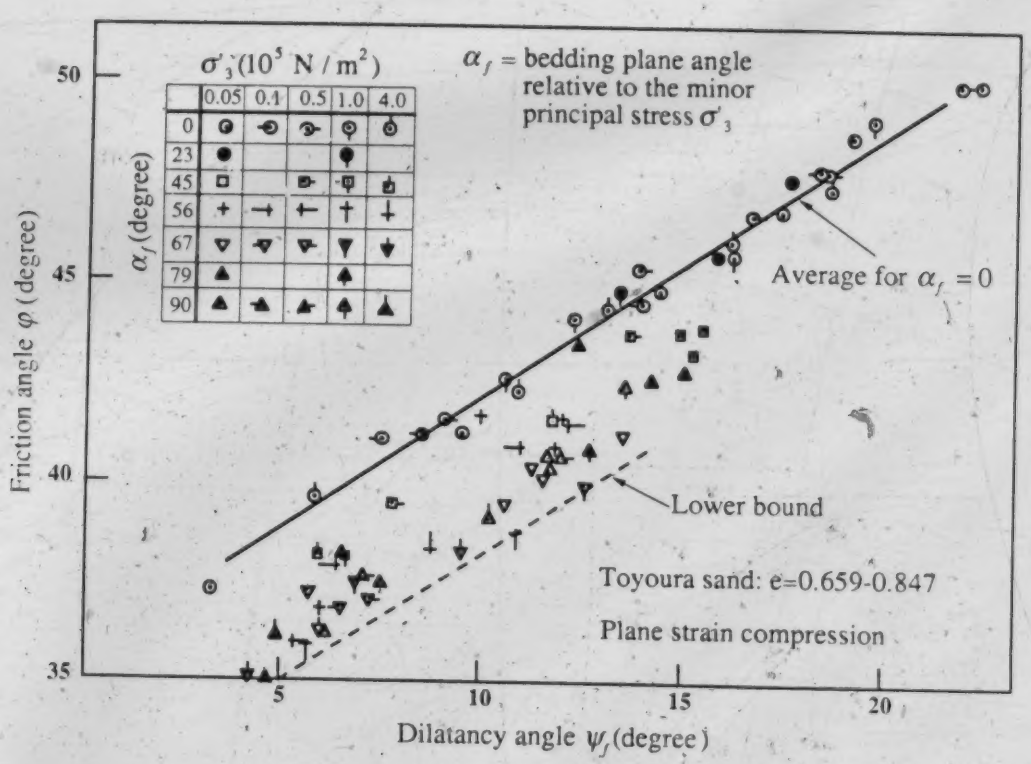

Figure 2.5 Variation of dilatancy angle with friction angle for Toyoura sand: modified after Tatsuoka et al. [1990]

Chapter 3

Localization as a Problem of Bifurcation

3.1. General

The phenomenon of bifurcation derives much of its terminology from the emergence of multiple solutions for a physical problem as a result of branching at a singular point on the solution path. Under a change in character of the governing equations it is then found that the evolution of the governing physical process undergoes a transition from a fundamental solution path into an alternate one. In order to set the character of the problem of bifurcation, an analogy will be made with two simple examples in the context of physical processes.

The first example is concerned with the boiling point of a liquid. The process which takes place when the liquid is heated can be mathematically described once the basic physics are established. As such, during heating the constituent molecules are excited to such an extent that their kinetic energies are dramatically increased. It is common to observe a critical temperature, dependent on pressure, at which boiling starts. This marks the beginning of a phase change at which the liquid turns into vapour. As heat is continually supplied to the system, most of it is consumed in producing the phase change as opposed to increasing the temperature. This mechanism which involves a deviation from the

fundamental path (no change of phase with a temperature increase) into an alternate one (change of phase with constant temperature) is very analogous to a bifurcation process. Moreover, it is known that the temperature at which the phase change occurs is very sensitive to the degree of purity of the liquid. For instance, water in the impure state may not freeze below zero degree Celsius under normal pressure and may therefore exist in liquid form rather in the solid state. The duality of states which water can fulfill under different conditions of purity is analogous to the phenomenon of bifurcation of a physical system due to the introduction of imperfections.

The second example is concerned with the elastic buckling of a column subjected to axial loading. While the fundamental path is a homogeneous axial elastic compression, a critical load (Euler's load) is reached at which the column snaps laterally with a combination of axial and flexural movements. In this situation the bifurcation process is of geometrical nature and is triggered only if the column is perfect.

It is interesting to note that in the first example, as the bifurcation point is passed (liquid turns into vapour), the constitutive relation describing the gas phase is different from that of the liquid phase. However, the contrasting difference in the case of buckling of the column is that the same constitutive equations govern the behaviour of the system in both pre and post buckling regimes.

The localization of plastic deformation has been the object of intense study for the past decades. It can be viewed from diverse perspectives, for example localization starts as a result of structural imperfections such as material weaknesses, stress concentrations and discontinuous boundary conditions. Also it may be considered as a bifurcation problem whereby the constitutive behaviour of the material becomes unstable under certain conditions and localization manifests itself as a shear band.

In trying to pursue an investigation into localization, it will be appropriate in this study to invoke the theory of bifurcation as in Thomas [1961] and Hill [1962a]. Localized deformation is construed as an outcome of material instability, and also as a spontaneous

loss of uniqueness of governing incremental equilibrium equations which results in the emergence of a possible alternate mode of non-homogeneous deformation. Local neighbourhoods of the material depart from near uniform straining in favour of highly localized patterns.

The conditions under which localized deformation modes arise are currently well understood, see for example Rice [1976]. However, preferential attention has been given to the study of shear banding in mainly metals, and the possibility of applying localization techniques in a numerical perspective for soils has remained relatively unexplored. Hence, bifurcation relations are elaborated and applied to the calculation of shear band initiation and inclination for simple constitutive laws with von Mises and Mohr-Coulomb conditions for both cohesive and frictional materials respectively. In order not to detract from practicality, it is thought quite logical to follow such an approach rather than to proceed to complexities such as yield vertex surfaces, Rudnicki and Rice [1975] and non coaxiality of stress and strain increments, Vardoulakis et al. [1978] and recently Yatomi et al. [1989], which also trigger instability. The influence of non-associativity is explored with respect to dilation expressed by the well established Rowe's stress dilatancy equation. Shear band inception is encountered whenever the hardening modulus achieves a critical value, which also leads to the definition of a bifurcation surface in stress space. It is found that for certain states depending on the negativeness of the softening modulus, four solutions for shear band inclination can be obtained.

As the foregoing concepts are to be incorporated into a finite element procedure for the analysis of localized deformation, stability criteria for general stress states are expanded and expressed in convenient closed form so that they can be checked easily during the location of a bifurcation point. The continuation of the solution along the localized path is then undertaken by introducing a shear band element with appropriate deformational capabilities, details of which will be expounded in Chapter 4.

3.2 Localization of inelastic deformation

In this section some aspects of the general theory of localization of inelastic deformation are reviewed. For sake of simplicity infinitesimal deformations will be considered throughout and rotational effects neglected. Standard tensor notation will be used. Subscripts preceded by commas denote partial derivative with respect to spatial coordinates.

3.2.1 Kinematics of a shear band

Consider a body sustaining initial homogeneous fields of Cauchy stresses σ_{ij} and infinitesimal strains ε_{ij} in a chosen frame of reference axes (x_1, x_2, x_3). A shear band will develop whenever a bifurcation occurs in such a manner that the field of displacement gradient $u_{i,j}$ becomes non-uniform and discontinuous across a band of orientation **n**, see Figure 3.1.

If **a** is an arbitrary vector in space which is zero everywhere outside the shear band, kinematic conditions describing the jump in displacement gradient while displacements being still continuous across the band are restricted by Maxwell's theorem, see Truesdell and Toupin [1960], i.e.

$$[\![u_{i,j}]\!] = a_i\, n_j \tag{3.1}$$

in which $[\![.]\!]$ signifies the jump operator. Since $\varepsilon_{ij} = \frac{1}{2}(u_{i,j}+u_{j,i})$, it follows that

$$[\![\varepsilon_{ij}]\!] = \frac{1}{2}(a_i\, n_j + a_j\, n_i). \tag{3.2}$$

The above physically refers to a jump in displacement gradient or strain of amplitude **a** across a band of normal **n**. A pure shear mode corresponds to **a** orthogonal to **n**. In effect, experimental measures of the displacement field during localization in an incompressible soil material confirm that the locus of iso-values of the dominant displacements is more or

less parallel to the shear band and hence can be considered as lines of zero extension. On the other hand, a pure splitting mode corresponds to **a** parallel to **n**. In most situations, the emerging mode is a combination of the two limiting cases.

3.2.2 Statical condition

Across the shear band, continuity of traction forces $\dot{t}_i$ must be enforced so as to maintain equilibrium. This translates into the following statical condition:

$$\dot{t}_i = [\![n_j \, \dot{\sigma}_{ij}]\!] = n_j [\![\dot{\sigma}_{ij}]\!] = 0. \tag{3.3}$$

3.2.3 Constitutive relationship

Since prior to bifurcation, the body is subjected to a homogeneous state, it is quite reasonable to link stresses to strains by means of a rate independent relationship of the form

$$\dot{\sigma}_{ij} = L_{ijkl} \, \dot{\varepsilon}_{kl}, \tag{3.4}$$

where L_{ijkl} is the tangential constitutive tensor. If the same material behaviour applies both inside and outside the shear band, which corresponds in fact to a continuous bifurcation, the jump operator applied to Eq. (3.4) yields

$$[[\dot{\sigma}_{ij}]] = L_{ijkl} [[\dot{\varepsilon}_{kl}]]. \tag{3.5}$$

Replacing the above into Eq. (3.3) and bringing in the kinematic condition described by Eq. (3.2), finally imply that

$$(n_i L_{ijkl} n_l) \dot{a}_k = 0. \tag{3.6}$$

A trivial solution of **a** (i.e. $a_k = 0$) corresponds to a continuous displacement gradient as inferred in Eq. (3.1). However in order to arrive at non-trivial solutions of a_k, the discriminant of the homogeneous system of equation (3.6) with the three unknowns a_1, a_2, a_3 must vanish, namely the determinant

$$\det(n_i L_{ijkl} n_l) = 0. \tag{3.7}$$

The existence of real solutions of the above equation is the basic requisite for continuous bifurcation to take place, with directions **n** indicating normals to which a shear plane may develop. Further deformation may then result in an infinite number of shear planes forming a finite shear band inside which fairly large deformation takes place. However, while this linear bifurcation theory can satisfactorily predict shear band direction and corresponding load level characterized by the tangential constitutive tensor, no information is given for the shear band thickness.

3.3 Continuous bifurcation

In order to explore the solutions of Eq. (3.7), for a continuous bifurcation phenomenon, consider the following particular form of constitutive rate relation

$$\dot{\boldsymbol{\sigma}} = \mathbf{E}:(\dot{\boldsymbol{\varepsilon}} - 1/H(\mathbf{Q}:\dot{\boldsymbol{\sigma}})\ \mathbf{P}) \tag{3.8}$$

in which **P** and **Q** are metric tensors representing plastic strain directions and normals to the yield surface respectively. The symbol : denotes an inner product in the sense that $\mathbf{A}:\mathbf{B} = (\mathbf{A})_{ij}(\mathbf{B})_{ij}$. H is the plastic hardening modulus whereas **E** is the tensor of elastic moduli for incremental deformation assumed in the form:

$$E_{ijkl} = \Lambda\delta_{ij}\delta_{kl} + G(\delta_{ik}\delta_{jl} + \delta_{il}\delta_{jk}), \tag{3.9}$$

Λ and G are the Lamé constants for isotropic response and δ_{ij} is the Kronecker delta. Equation (3.8) arises as a consequence of Melan's definition [1938] of rate of plastic strains

$$\dot{\boldsymbol{\varepsilon}}^{p} = \frac{1}{H}(\mathbf{Q}:\dot{\boldsymbol{\sigma}})\mathbf{P}. \tag{3.10}$$

The explicit form of the constitutive rate relation given in Eq. (3.8) which would fit into the bifurcation criterion is classically given as

$$L_{ijkl} = E_{ijkl} - \frac{E_{ijmn}P_{mn}Q_{st}E_{stkl}}{H + Q_{op}E_{opqr}P_{qr}}. \tag{3.11}$$

When the above constitutive tensor is replaced into the bifurcation criterion in Eq. (3.7) and after some tensor manipulations, the following generic expression is obtained:

$$\frac{H}{2G} = 2\,\mathbf{n}.\mathbf{P}.\mathbf{Q}.\mathbf{n} - (\mathbf{n}.\mathbf{P}.\mathbf{n})(\mathbf{n}.\mathbf{Q}.\mathbf{n}) - \mathbf{P}:\mathbf{Q}$$

$$- \frac{\Lambda}{\Lambda + 2G}(\mathbf{n}.\mathbf{P}.\mathbf{n} - \text{trace}\,\mathbf{P})(\mathbf{n}.\mathbf{Q}.\mathbf{n} - \text{trace}\,\mathbf{Q}). \tag{3.12}$$

The above expression gives the hardening modulus at which instability in the form of a shear band may occur. However, no information is given on inception of the first band when the plastic hardening modulus achieves a critical value.

3.3.1 Bifurcation directions

In order to simplify the analysis of the bifurcation criterion without loss of generality, it is desirable to consider the particular case of a planar shear band whose normal lies in the x_1-x_2 plane, i.e.,

$$\mathbf{n} = (\alpha,\beta,0) = (-\sin\theta,\cos\theta,0), \tag{3.13}$$

where θ is the angle the shear band makes with the x_1 axis. Also, let the set of reference axes coincide with the directions of principal stresses and strains such that the second order tensors **P** and **Q** reduce to

$$\mathbf{P}=\begin{bmatrix} P_1 & 0 & 0 \\ 0 & P_2 & 0 \\ 0 & 0 & P_3 \end{bmatrix};\quad \mathbf{Q}=\begin{bmatrix} Q_1 & 0 & 0 \\ 0 & Q_2 & 0 \\ 0 & 0 & Q_3 \end{bmatrix} \tag{3.14}$$

The explicit form of the bifurcation criterion, obtained by replacing Eqs. (3.13) and (3.14) into (3.12), is given by

$$\begin{aligned}\frac{H}{2G} &= 2(P_1Q_1\sin^2\theta + P_2Q_2\sin^2\theta) - (P_1\sin^2\theta + P_2\cos^2\theta) \\ &\quad (Q_1\sin^2\theta + Q_2\cos^2\theta) - (P_1Q_1 + P_2Q_2 + P_3Q_3) \\ &\quad -\frac{\Lambda}{\Lambda+2G}\left\{(P_1\sin^2\theta + P_2\cos^2\theta) - (P_1+P_2+P_3)\right\} \\ &\quad \left\{(Q_1\sin^2\theta + Q_2\cos^2\theta) - (Q_1+Q_2+Q_3)\right\}.\end{aligned} \tag{3.15}$$

On the basis of the above expression, the incipient shear band inclination depends on the current state of stress characterized by **P** and **Q** as well as the plastic hardening modulus H. In order to solve for shear band inclinations, Eq. (3.15) may be conveniently recast into a quadratic equation in $\cos 2\theta$ or ($\sin^2\theta$), so that

$$b_0\cos^2 2\theta + b_1\cos 2\theta + b_2 = 0, \tag{3.16}$$

where

$$b_0 = -(1+k)(P_1 - P_2)(Q_1 - Q_2),$$

$$b_1 = 2\{[(Q_1 + Q_3)(P_2 - P_1) + (P_2 + P_3)(Q_2 - Q_1)]k + P_2Q_2 - P_1Q_1\},$$

$$b_2 = -4P_3Q_3 + (P_1 + P_2)(Q_1 + Q_2)(1+k) - 2k[(P_1 + P_2)Q_3 + (Q_1 + Q_2)P_3] - \frac{2H}{G},$$

$$k = \frac{\Lambda}{\Lambda + 2G} = \frac{\nu}{1-\nu}\ ;\ \nu = \text{Poisson's ratio.} \tag{3.17}$$

Equation (3.16) generally admits four solutions, and since only real values of θ are of interest, the character of the solution depends on whether $\cos 2\theta$ or $\sin^2\theta$ is real. Thus, the main possibilities of solution are outlined as

1. *Elliptic case:* no real solution of $\cos 2\theta$ exists, i.e. $\sin^2\theta \le 0$ or $\sin^2\theta \ge 1$ or $\sin^2\theta$ is complex;
2. *Parabolic case:* two real solutions of θ exist $(\pm\theta_1, \pm\theta_2)$;
3. *Hyperbolic case:* four real solutions of θ exist .

Prior to bifurcation, no instability is possible since equation (3.16) does not yield any real solution; this is the elliptic case. However assuming a continuous transition of the solution regime from elliptic to hyperbolic through parabolic, the first shear band will develop at the critical instant when the discriminant of Eq. (3.16) vanishes, i.e. when

$$\cos 2\theta_{crit} = \frac{P_2Q_2 - P_1Q_1 + k\{(Q_1 + Q_3)(P_2 - P_1) + (P_2 + P_3)(Q_2 - Q_1)\}}{(1+k)(P_1 - P_2)(Q_1 - Q_2)},$$

$$P_1 \neq P_2\ ;\ Q_1 \neq Q_2. \tag{3.18}$$

Substituting for the value of k into Eq. (3.18) and after some algebra, the critical shear band orientation simply becomes

$$\cos 2\theta_{crit} = \frac{P_1 + \nu P_3}{(P_2 - P_1)} + \frac{Q_2 + \nu Q_3}{(Q_2 - Q_1)}. \tag{3.19}$$

The corresponding plastic modulus ratio follows as

$$\frac{H_{crit}}{2G} = \frac{\left\{(Q_1 P_2 - Q_2 P_1) + \nu\left[Q_3(P_2 - P_1) + P_3(Q_2 - Q_1)\right]\right\}^2}{4(1-\nu)(P_1 - P_2)(Q_1 - Q_2)} - \frac{P_3 Q_3}{(1-\nu)}. \tag{3.20}$$

While the condition of shear banding is completely determined by **P**, **Q** and **n** , the critical hardening modulus is on the other hand a computed quantity. This critical modulus ratio can be either positive or negative depending on the magnitude of **P** and **Q**. In other words, this means that bifurcation into a shear band can occur on the hardening branch of the stress-strain curve for a non-associated flow rule. This has been experimentally observed by Vardoulakis [1980] and Vermeer [1982]. On the other hand for an associated flow rule, **P** = **Q**, Eqs. (3.19) and (3.20) simply reduce to

$$\cos 2\theta_{crit} = \frac{Q_1 + Q_2 + 2\nu Q_3}{Q_2 - Q_1}, \tag{3.21}$$

$$\frac{H_{crit}}{2G} = -\frac{(3\Lambda + 2G)}{2(\Lambda + G)} Q_3^2 = -(1+\nu) Q_3^2. \tag{3.22}$$

Contrary to a non-associated flow rule, normality of plastic flow implies that bifurcation can only occur for $H \leq 0$, i.e. strain softening or perfect plasticity.

3.4 Material model

In order to gain physical insight into the significance of equations (3.19) and (3.20), simple material models such as the incompressible von Mises elasto-plastic model with associated flow rule and isotropic softening as well as the Mohr-Coulomb material are investigated.

3.4.1 Prandtl-Reuss material

The yield condition is given by the function F as follows

$$F = \tfrac{1}{2} s_{ij} s_{ij} - \kappa^2 = 0, \tag{3.23}$$

in which s_{ij} is the deviatoric stress such that

$$s_{ij} = \sigma_{ij} - \tfrac{1}{3} \sigma_{kk} \delta_{ij}. \tag{3.24}$$

The yield stress which corresponds to the radius of the von Mises surface centred about the hydrostatic axis is represented by κ. During plastic flow κ is usually made to vary with the amount of plastic strains mobilized, or is made to remain fixed in the case of perfect plasticity.

During plane strain compression in the x_1 direction oriented vertically, with no lateral confining pressure in the x_2 direction, the loading conditions are

$$\varepsilon_{33} = \varepsilon_{12} = \varepsilon_{23} = \varepsilon_{31} = 0 \quad \text{and} \quad \sigma_2 = 0. \tag{3.25}$$

If all stress components are assumed to be zero at the beginning of loading, only σ_1 and σ_3 will change. Thus the gradient to the yield surface F becomes

$$\mathbf{P} = \mathbf{Q} = \frac{1}{\sqrt{2}} \{ 1 \ , \ -1 \ , \ 0 \}. \tag{3.26}$$

When replaced into Eq. (3.15), the condition for shear bands is as follows

$$\frac{H_{crit}}{2G} + \frac{1}{2(1-\nu)}\cos^2 2\theta = 0. \tag{3.27}$$

As expected for perfect plasticity (H=0) the above relation gives 2 shear planes oriented at ±45°. For various values of H, the solutions may unfold different orientations as illustrated in Figure 3.2. It is seen that different modes emerge depending upon the negativeness of the modulus ratio. For instance, four conjugate shear band orientations can be obtained for $H/2G = -0.5$, while splitting occurs at $H/2G = -1.0$. These specific modes are quite difficult to obtain in geomaterials because the state $H/2G = 0$ is momentarily reached before the post-peak range where damage is caused to the structure. At that point, due to high instability the occurrence of the above mentioned modes are suppressed. The situation is more favourable in the case of a metallic medium which may carry the peak load without fracture over a larger range of deformation.

3.4.2 Mohr-Coulomb material

In plane strain conditions, the Mohr-Coulomb yield surface is described by

$$F = \tfrac{1}{2}(\sigma_1 - \sigma_2) - \tfrac{1}{2}(\sigma_1 + \sigma_2)\sin\varphi, \tag{3.28}$$

in which σ_1 and σ_2 are principal stresses and the third stress σ_3 is ignored; φ is the mobilized internal friction angle. For an associated flow rule, the plastic strain directions are related to the gradient to F which read:

$$\frac{\partial F}{\partial \sigma_1} = \frac{1-\sin\varphi}{2}, \frac{\partial F}{\partial \sigma_2} = -\frac{1+\sin\varphi}{2}. \tag{3.29}$$

Shear band inclinations may be obtained by replacing the above into Eq. (3.21) which leads after some simplifications to

$$\cos 2\theta_{crit} = \sin\varphi, \ \therefore \theta_{crit} = \frac{\pi}{4} \pm \frac{\varphi}{2}. \tag{3.30}$$

3.4.3 Non-associated flow rule

A plastic potential can be conveniently chosen to define plastic strains. It is assumed much in the same spirit to take the equivalent form as the yield function such that the friction angle φ is replaced by the dilation angle ψ, i.e.,

$$G = \tfrac{1}{2}(\sigma_1 - \sigma_2) - \tfrac{1}{2}(\sigma_1 + \sigma_2)\sin\psi, \tag{3.31}$$

The gradient to the plastic potential is simply obtained by replacing φ by ψ in Eq.(3.29). Thus,

$$\frac{\partial G}{\partial \sigma_1} = \frac{1-\sin\psi}{2}, \frac{\partial G}{\partial \sigma_2} = -\frac{1+\sin\psi}{2}. \tag{3.32}$$

The critical inclination at bifurcation is obtained by substituting Eqs.(3.29) and (3.32) into Eq. (3.19):

$$\cos 2\theta_{crit} = -\sin\frac{(\varphi+\psi)}{2}\cos\frac{(\varphi-\psi)}{2}. \tag{3.33}$$

If the dilatancy angle is very close to the angle of friction, then $\cos(\varphi - \psi)/2 \equiv 1$. Also in practice, the difference between the two angles is usually less than 30^o so that $\cos(\varphi - \psi)/2$ varies between 0.9659 and 1. Therefore

$$\theta_{crit} = \frac{\pi}{4} \pm \frac{(\varphi+\psi)}{4}. \tag{3.34}$$

The corresponding expression for the critical plastic hardening modulus emerges as

$$H_{crit} = \frac{G}{8(1-\nu)}(\sin\varphi - \sin\psi)^2 \tag{3.35}$$

which is in agreement with Mandel's expression [1966].

3.5 Simple friction hardening model

The expression for the critical plastic hardening modulus was derived in previous sections. It is intended to explore its physical significance by extending the simple perfectly plastic basic model into a friction hardening model with a non-associated plastic flow rule and dilation described by Rowe's stress dilatancy equation [1962].

3.5.1 Hardening law

The process of hardening is regarded as the gradual mobilization of friction angle as plastic slips/distortions progress during deformation. Experimental evidence often shows that the behaviour can be described by means of a hyperbolic function of the form

$$\sin\varphi_m = \mu = \mu_p \frac{\gamma^p}{A + \gamma^p}, \tag{3.36}$$

in which $\mu_p = \sin\varphi_p$, where φ_p is the peak friction angle. γ^p is a scalar quantity representing the plastic strain history while A is a material constant. A conventional expression for the plastic hardening modulus is obtained by writing the consistency equation ($dF = 0$), i.e.,

$$H = -\frac{\partial F}{\partial \mu}\frac{\partial \mu}{\partial \gamma^p}. \tag{3.37}$$

$$H = (\sigma_1 + \sigma_2)\frac{(\mu_p - \mu)^2}{A\mu_p} \tag{3.38}$$

3.5.2 Bifurcation surface

Stress states at the onset of bifurcation can be obtained by equating Eq. (3.38) with (3.35) and having stresses as sole variables. To this end, mobilized friction has to be related to the amount of dilation at any stress level. Rowe's stress dilatancy equation couples the rate of plastic volumetric strain ($\dot{\varepsilon}_v^p / \dot{\varepsilon}_1^p$) to effective stress ratio (σ_1 / σ_3), i.e.,

$$\frac{\sigma_1}{\sigma_3} = K(1 - \frac{\dot{\varepsilon}_v^p}{\dot{\varepsilon}_1^p}) \quad \text{for triaxial and plane strain compression,} \tag{3.39a.}$$

$$\frac{\sigma_1}{\sigma_3} = K / (1 - \frac{\dot{\varepsilon}_v^p}{\dot{\varepsilon}_1^p}) \quad \text{for triaxial extension.} \tag{3.39b.}$$

K is a material constant related to energy considerations and is equal to $\tan^2(\frac{\pi}{4} + \frac{\varphi_{cv}}{2})$, φ_{cv} being the friction angle at constant volume. The stress ratio can be expressed in terms of mobilized friction angle by means of Eq. (3.28). By the use of the usual definition of dilation angle in plane strain conditions as defined by Hansen [1958], a more convenient form of Rowe's equation emerges as

$$\sin\psi = \frac{\sin\varphi_m - \sin\varphi_{cv}}{1 - \sin\varphi_m \sin\varphi_{cv}} = \frac{\mu - \mu_c}{1 - \mu\mu_c} \tag{3.40}$$

The above expression links dilation to the mobilization of friction angle which is a path dependent parameter by virtue of Eq. (3.36). Consequently, the plastic potential function also becomes path dependent and this may lead to an inconsistency in the plasticity formalism.

Equation (3.40) can be recast in convenient form in view of expanding Eq. (3.35) such that

$$\sin\varphi_m - \sin\psi = \frac{\mu(1-\mu^2)}{1-\mu\mu_c}. \tag{3.41}$$

Considering the fact that $\mu = (\sigma_1 - \sigma_2)/(\sigma_1 + \sigma_2)$, the critical plastic hardening modulus becomes

$$H_{crit} = \frac{E\mu_c^2}{(1-\nu^2)(\sigma_1+\sigma_2)^2}\frac{\sigma_1^2\sigma_2^2}{\left[(\sigma_1+\sigma_2)-(\sigma_1-\sigma_2)\mu_c\right]^2}. \tag{3.42}$$

For localization to become possible, the current plastic hardening modulus must at most be equal to the above critical value; this leads after some simplifications to

$$\left[(\sigma_1+\sigma_2)\mu_p - (\sigma_1-\sigma_2)\right]^2 - \frac{EA\mu_c^2\mu_p}{(1-\nu^2)(\sigma_1+\sigma_2)^2}\frac{\sigma_1^2\sigma_2^2}{\left[(\sigma_1+\sigma_2)-(\sigma_1-\sigma_2)\mu_c\right]^2} \le 0. \tag{3.43}$$

Calling $s = (\sigma_1 + \sigma_2)/2$ and $t = (\sigma_1 - \sigma_2)/2$, Eq. (3.44) can be conveniently recast into

$$\left[(s\mu_p - t)(s - t\mu_c)\right]^2 - \frac{EA\mu_p\mu_c^2}{32(1-\nu^2)s}(s^2 - t^2) \le 0. \tag{3.44}$$

The above expression describes the locus of stress points which satisfy bifurcation in the stress space, The resulting surface can be viewed as a bifurcation surface enclosing a permissible domain within which the material is stable, see Pietruszczak and Stolle [1987]. Figure 3.3 illustrates the bifurcation surface for a typical sand. It is interesting to note that the bifurcation surface is reached well before the conventionally known failure surface, implying that localization can take place before peak. However, if an associated flow rule is

used, the critical plastic hardening modulus becomes zero and Eq. (3.44) obviously reverts to the classical failure surface. Figure 3.4 shows the corresponding stress strain curve with location of the bifurcation point using the model based on Rowe's stress dilatancy equation, while Figure 3.5 illustrates the intersection of the plastic hardening modulus curve with the bifurcation surface in the space (φ,ψ,H) in a typical finite element analysis.

3.5.3 Shear band conditions under different stress configurations

It is conceivable that criteria set by Eqs. (3.19) and (3.20) for the onset of shear banding depend very much on tensors **P** and **Q**, i.e. prevalent stress states. For this reason it is proposed to explore the physical significance of those criteria by investigating three of the most common stress conditions encountered in geotechnical engineering: triaxial compression, triaxial extension and plane strain compression.

Table 3.1 summarizes the values of the tensors **P** and **Q** under those different stress conditions. Note that the directions of normals to the yield surface are simply obtained by substituting K=1 in the equations, i.e. $\varphi_{cv} \neq 0$. In such situation both plastic potential and yield surfaces are made to coincide as a result of $\psi = \varphi$ in the expression (3.40).

The hardening process is described by Eq. (3.20). A well known fact encountered in the deformation process is that the rate of hardening initially starts off with a high value which eventually drops to zero (perfect plasticity) and becomes negative (softening) as further straining is imposed. As such, bifurcation in the form of localization takes place whenever the hardening modulus first reaches a critical value.

Figure 3.6 illustrates the variation of the critical hardening modulus with stress ratio. It can be seen that for plane strain conditions, the critical hardening modulus is always positive and eventually decreases asymptotically to zero. This means that localization is very prone to occur in the ascending branch of the stress-strain curve. On the other hand, in both triaxial compression and extension, the critical hardening modulus is

always negative. Thus it implies that the only possibility for shear bands to appear is in the softening branch of the stress-strain curve. This very interesting piece of information reveals that in general shear bands appear more easily in plane strain conditions as opposed to triaxial compression, and that triaxial extension might be the middle situation. Also, experimental evidence shows that localization into a shear band tends to occur at a low stress range for granular materials in plane strain conditions. In triaxial stress conditions, on the contrary, the loss of homogeneity is predominantly diffuse (barelling) rather than of the shear band type, see Vardoulakis [1979] and Arthur and Dunstan [1982]. Mathematically speaking due to the nature of axi-symmetrical stress conditions, if the shear band were to appear, it would have to form in a conical surface, and this configuration is kinematically difficult to occur. However, in practice, one does observe planar shear bands in the triaxial cell because of imperfections such as weak points and stress concentrations at boundaries.

A possible physical explanation for this interesting phenomenon is the direct connection between dilation due to severe distortion and shear band formation in a granular material. In conventional triaxial stress conditions, the material has the freedom to dilate in all directions once the shear band forms, i.e. loosening takes place in a direction perpendicular to the band (direction of zero extension), and also in a direction contained in the shear plane. If we turn to the plane strain case, the kinematic condition is such that the material is constrained to deform in a plane perpendicular to the shear band. Considering that the same amount of global dilation takes place in the two situations, we can conclude that the extent of dilation perpendicular to the shear band in plane strain will be greater than in the equivalent triaxial case. As a consequence plane strain conditions are more prone to localization than are triaxial stress conditions. Finally, it should be remembered that the opposite situation occurs when dealing with mobilization of friction since a lower shear strength is traditionally obtained in triaxial stress than in plane strain conditions. It seems that inception of localization and mobilization of strength are governed by two different

mechanisms. In essence, it can be said that material instability occurs prematurely in plane strain in contrast to triaxial stress conditions.

Figure 3.7 gives the plot of the corresponding critical shear band inclinations with stress ratio. Also are plotted the Mohr-Coulomb as well as the Roscoe solutions which correspond to stress and velocity characteristics repectively. The nature of these two solutions and how they relate to the shear band inclination were discussed in Chapter 2. It seems that the bifurcation analysis lies in between the two solution ranges which refer to traditional and practical solutions such as Mohr-Coulomb and Roscoe.

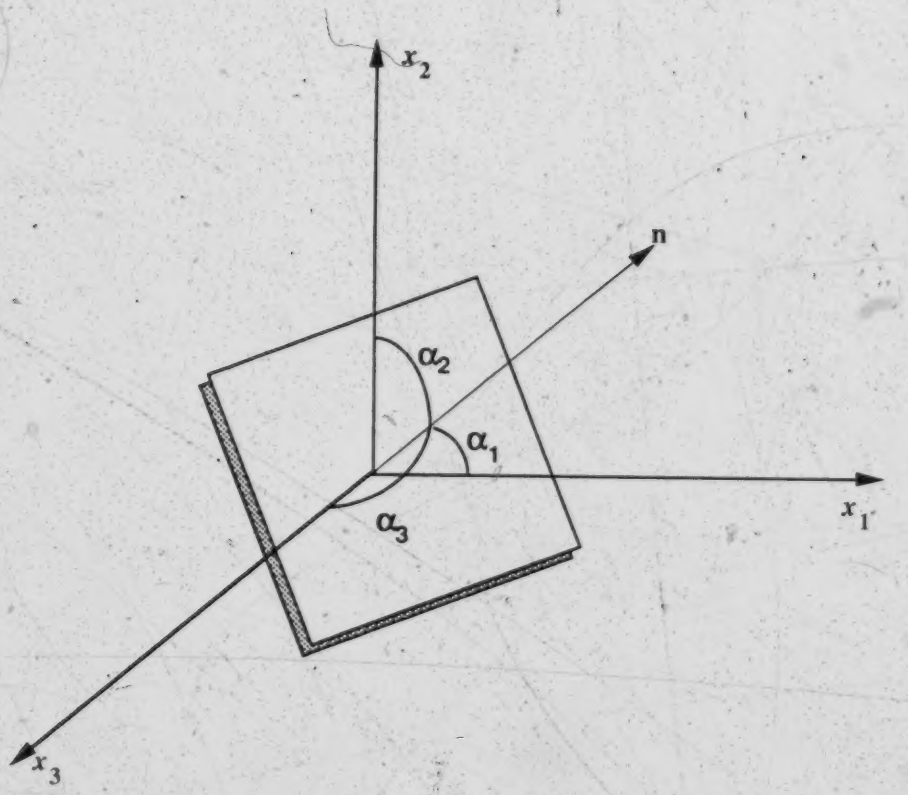

Figure 3.1 Shear band in 3-D space

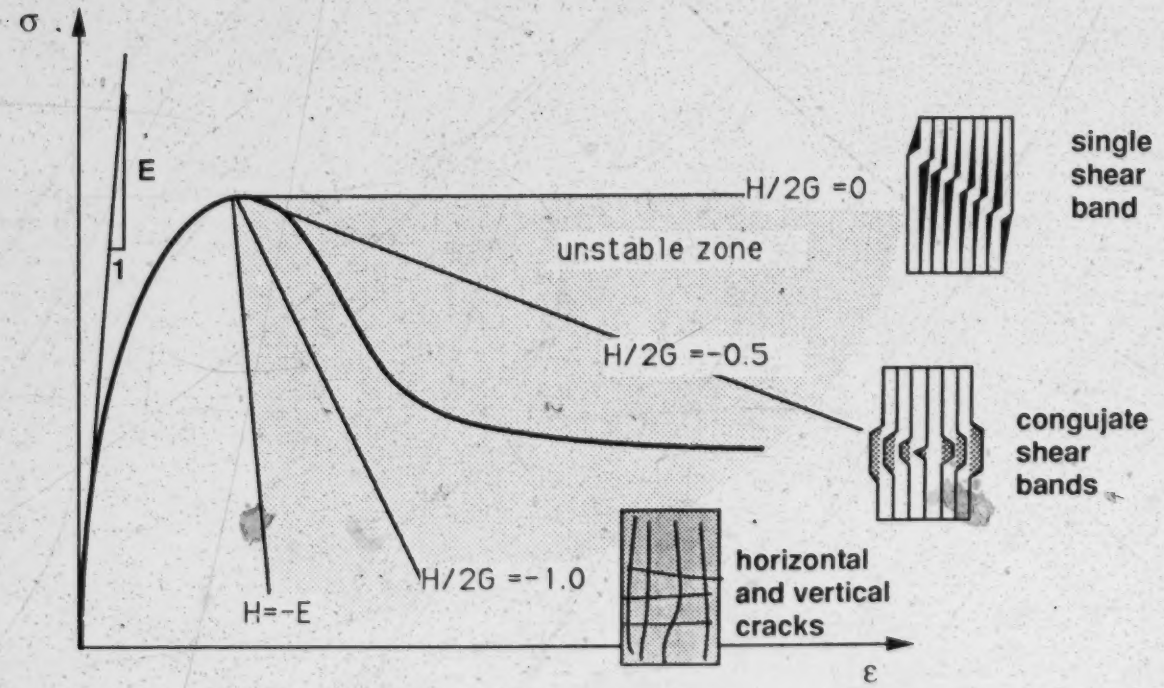

Figure 3.2 Bifurcation modes in plane strain conditions for a von Mises material

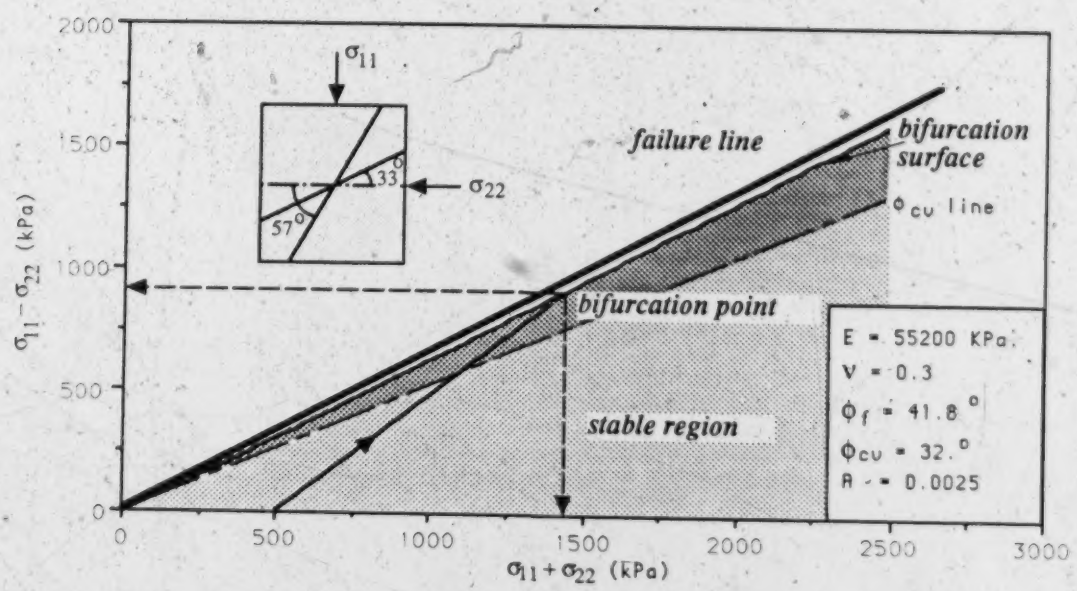

Figure 3.3 Bifurcation surface in stress space

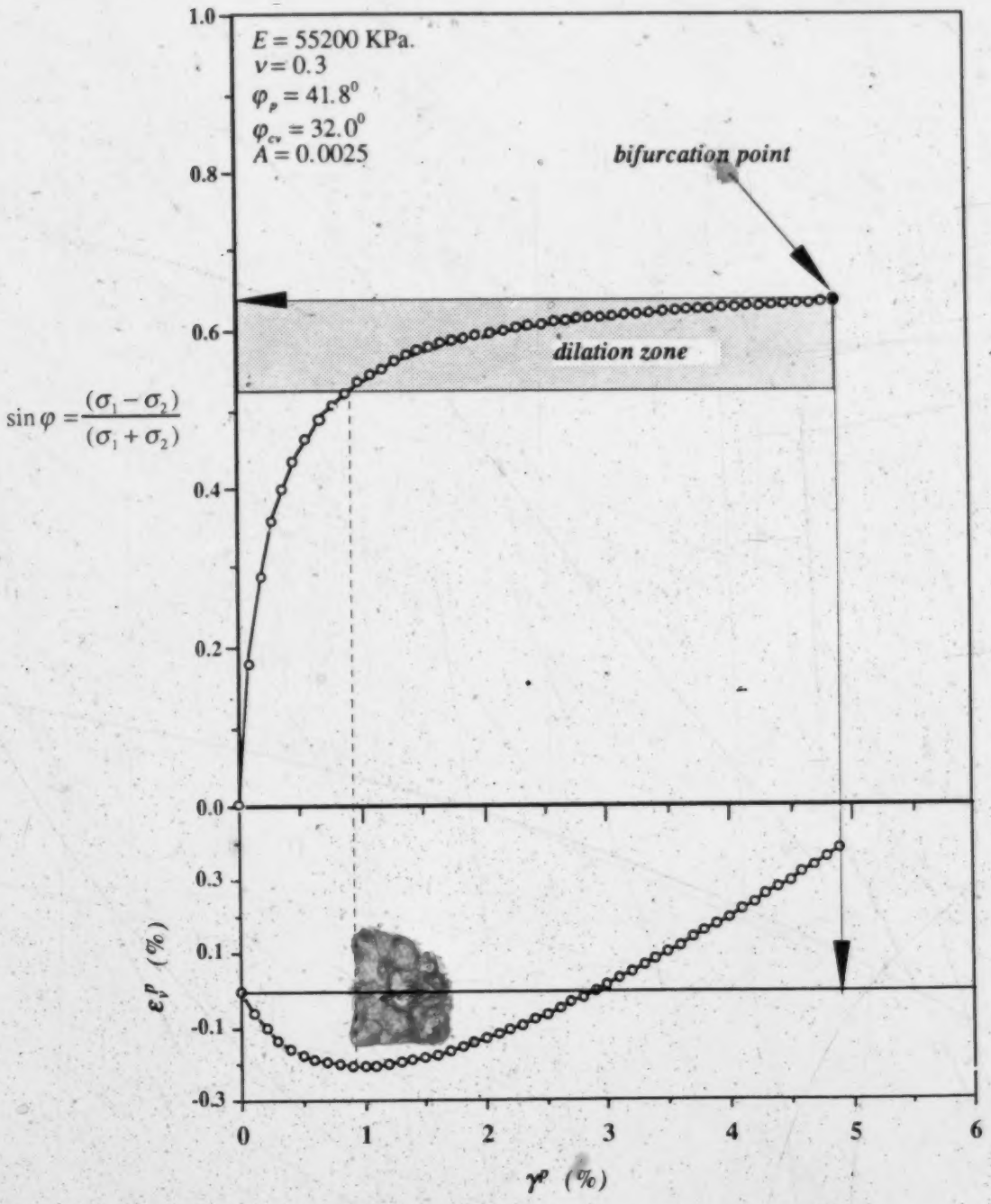

Figure 3.4 Stress-strain curve using Rowe's stress dilatancy equation

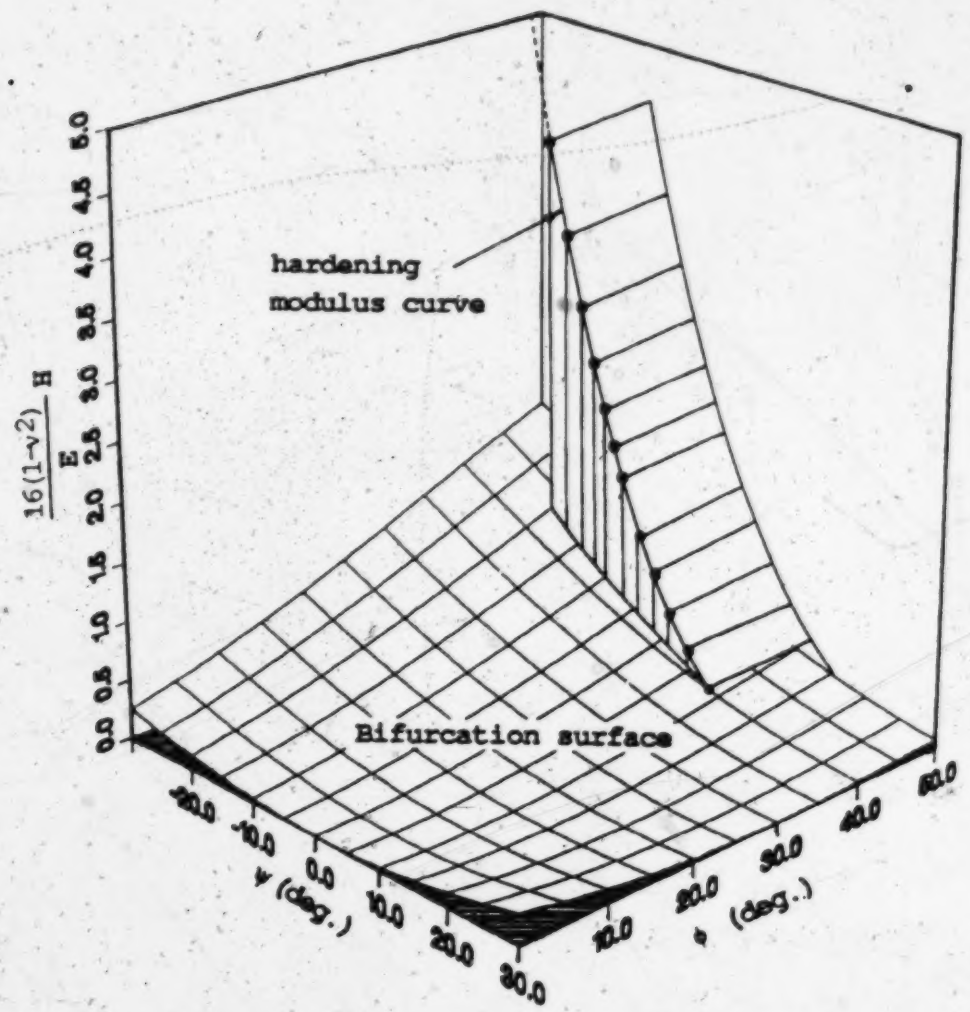

Figure 3.5 Intersection of hardening modulus curve with bifurcation surface

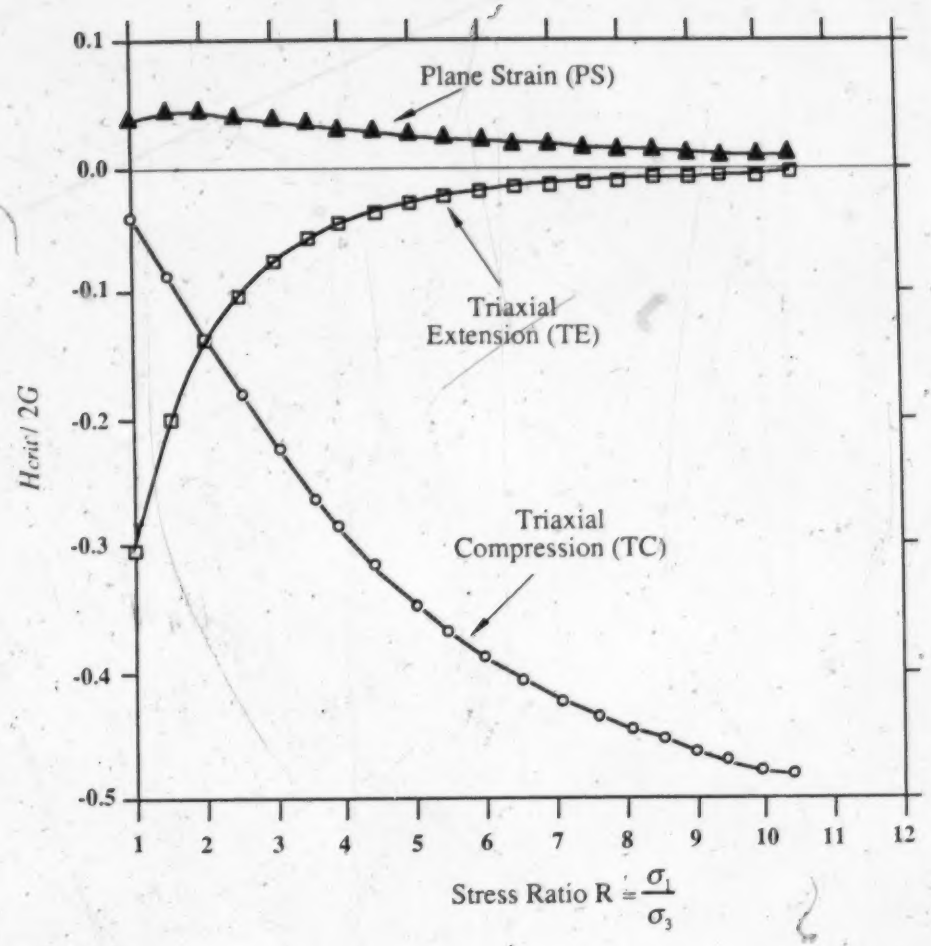

Figure 3.6 Variation of critical hardening modulus with stress ratio

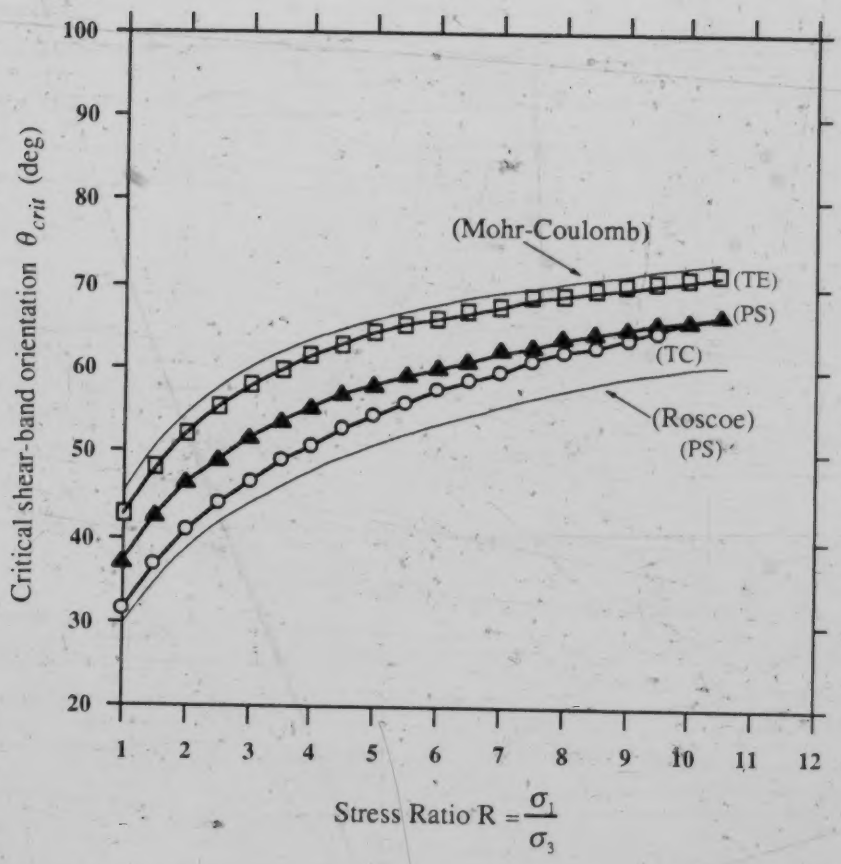

$$\theta_{crit}^{M.Coulomb} = \tan^{-1}\sqrt{\frac{\sigma_1}{\sigma_3}} \; ; \; \theta_{crit}^{Roscoe} = \tan^{-1}\sqrt{\frac{\dot{\varepsilon}_2}{\dot{\varepsilon}_1}}$$

Figure 3.7 Variation of critical shear band orientation with stress ratio

Table 3.1 Direction of plastic strains under different stress conditions

Stress Conditions	$P_1 = \frac{\partial G}{\partial \sigma_1}$	$P_2 = \frac{\partial G}{\partial \sigma_2}$	$P_3 = \frac{\partial G}{\partial \sigma_3}$
Plane Strain $\dot{\varepsilon}_1 < 0, \dot{\varepsilon}_3 = 0$	$\frac{-K}{\sqrt{K^2 + R^2}}$	$\frac{R}{\sqrt{K^2 + R^2}}$	0
Triaxial Compression $\dot{\varepsilon}_1 < 0, \dot{\varepsilon}_2 = \dot{\varepsilon}_3$	$\frac{-2K}{\sqrt{4K^2 + 2R^2}}$	$\frac{R}{\sqrt{4K^2 + 2R^2}}$	$\frac{R}{\sqrt{4K^2 + 2R^2}}$
Triaxial Extension $\dot{\varepsilon}_1 > 0, \dot{\varepsilon}_2 = \dot{\varepsilon}_3$	$\frac{2R}{\sqrt{4R^2 + 2K^2}}$	$\frac{-K}{\sqrt{4R^2 + 2K^2}}$	$\frac{-K}{\sqrt{4R^2 + 2K^2}}$

Note:

$$K = \tan^2\left(\frac{\pi}{4} + \frac{\varphi_{cv}}{2}\right); \quad R = \frac{\sigma_1}{\sigma_3}.$$

Values of **Q** (normals to the yield surface F) are obtained by making $K=1$, i.e $\varphi_{cv}=0$.

Chapter 4

Numerical modelling of localization

4.1. Introduction

One of the major challenges in computational mechanics nowadays is the pursuit of a complete numerical analysis for the failure of a structure. There has been much endeavour in trying to trace the deformation process as it changes from an initially near diffuse pattern whereby all field variables are continuous, into one of discontinuous character in the peak and post-peak regimes. Despite inherent complexities in the analysis and a formidable task of mathematical description, such computations may be at times justified for situations where one needs to evaluate the ultimate capacity as well as ensuing kinematics at the onset of failure.

In order to contemplate a rational framework within which reasonably accurate computations can be accomplished, the basic underlying physics governing localization are reviewed. The proper characterization of localization behaviour is presently of considerable conjecture and not fully understood. Some fundamental questions as how to relate the processes with foundations of continuum theory have been raised. This Chapter attempts to clarify those points and a numerical model is proposed.

4.2. Softening damage

The phenomenon of localization embodies a basic mechanism which involves accumulation of inelastic deformation in the form of damage. For instance, in geomaterials failure occurs by progressive damage manifested in various forms, among others, micro-cracking, discrete cracks, void formation and rupture/shear bands. The resulting phenomenological response is characterized by strain softening or softening damage with a gradual decline of stress at an increasing strain as the maximum stress is reached. This can be viewed as a progressive loss of stiffness with increasing load which eventually leads to failure of the material.

The description of strain softening from a fundamental viewpoint poses severe mathematical difficulties the implications of which are not yet fully understood. It may be tacitly regarded as the loss of positive definiteness of the matrix of the tangential modulus which in turn results into a spontaneous loss of ellipticity of incremental equilibrium equations. This loss of ellipticity which precludes any wave propagation—the acoustic tensor has imaginary eigenvalues—was probably first found by Hadamard [1903] who argued it is an inadmissible property for a continuum model. The same argument was later expanded by Hill [1958, 1962b] who set criteria for loss of ellipticity for elasto-plastic solids in a purely local fashion—i.e. they may be applied anywhere within the structure regardless of the boundary conditions and material properties. Rudnicki [1975, 1977] applied the concept to analyze localization into a planar shear band in an infinite half space for J_2 flow type and pressure sensitive type of materials. Those studies were undertaken using Hill's linear bifurcation theory.

Due to the loss of ellipticity of the governing equations for rate independent materials, the basic soundness of numerical solutions may be questionable, see Sandler and Wright [1984]. The initial boundary value problem becomes ill-posed since a small difference in load results in large changes in response. In fact Sandler examined the

problem of a one dimensional rod with velocity prescribed at one end, in which the material strain softens. By increasing the load slightly, a significantly different response was obtained.

The physical bases of strain softening in rocks, soil and concrete were investigated by Read and Hegemier [1984]. They raised the controversy on the existence of strain softening as a true material property and essentially claimed that strain softening does not exist—it is a purely geometrical artifact. Another yet more disturbing feature of strain softening is that inelastic deformation must localize into zones of vanishing volume according to a classical local continuum. Since the model entails a local measure such as an energy density function, the structure fails with zero dissipation—which is physically inadmissible and by far unrealistic.

4.2.1 Localization instabilities

The localization of inelastic deformation is seemingly the manifestation of an instability phenomenon.

In the context of plasticity, it can be regarded as a material instability triggered by a non-associated flow rule, or a yield vertex where the plastic strain rate vector is theoretically indeterminate. The localization criterion derived in Chapter 3 is very sensitive when subjected to the above mentioned subtle features. Thus, the degree of success for determining failure by means of localization techniques critically depends on having at hand a realistic description of the constitutive equation.

Other forms of localization instabilities emerge as distributed damage which can be caused by strain softening due to external agencies such as heat for example. Also liquefaction in dense sands can cause chaotic instability, while non-linear geometrical effects caused by large strains can lead to damage.

4.3 Consequences of using ordinary finite elements

Two major pathological difficulties are often encountered during the finite element computation of localization. Firstly the actual experimental width of localized bands are far smaller than the characteristic dimensions of the structure and hence the practical mesh size. Secondly, in continuum formulations, as the governing equations change in type, it is found that the width of the localized band is not unique since the theory does not provide for an internal characteristic length.

As a result of using ordinary finite elements solutions with strain softening, one often experiences a severe mesh dependence since capturing localization strongly depends on the size h of the mesh. This, together with the inability of the mesh to adequately reproduce localization of strain characterized by strain softening, leads to somewhat meaningless results from an engineering stand-point. Furthermore, the inherent concept of specific energy as measured per unit volume poses some difficulties as the size d_b of the localized zone vanishes to zero. As a matter of fact, with increasing mesh refinement, the energy dissipation in the strain softening zone approaches zero. This observation is physically unacceptable since energy is still dissipated along the surface contour of the localized area, although volume approaches zero. A solution to this disturbing shortcoming can be obtained by calculating energy by unit surface as opposed to volume. Another limitation is that finite element solutions exhibit a directional dependence since localization tends to follow certain preferred directions dictated by the mesh such as along edges and element diagonals where sharp strain gradients can be suitably resolved; see Leroy et al. [1988].

4.4 Possible remedies

One of the common methods used to avoid spurious mesh sensitivity in localization to a vanishing volume is to consider that the process is not instantaneous but develops with time. Then, there is no loss of ellipticity because the relevant stiffnesses for a viscoplastic

solid are the elastic stiffnesses and (det **n.L.n**) is always positive as long as the stress levels remain small. Needleman [1987] demonstrates that the introduction of rate sensitivity and viscosity effects in effect introduces a length scale in the boundary value problem, even though the constitutive description does not involve any material parameter with the dimensions of length. However, it can be argued that the methodology is purely an artifact since it just postpones the onset of instability. Simo [1988] subsequently coined the process as a viscoplastic regularization of the dissipation function in a mathematical sense.

In order to remedy some of the undesirable features of strain softening solutions such as mesh size and directional dependencies, a very profound and effective approach is concerned with the introduction of non-local concepts. Non-local theories were first introduced by Kroner [1967] and further developed by Eringen [1972] for elasticity problems. This concept states that the stress-strain relationship is not considered to be local but links the stress at a point to the state of deformation within a finite volume about that point in a distributional sense. In essence, the local continuum variables defined per unit of volume are replaced by a non-local condition within a designated finite volume, in order to make physical quantities such as plastic dissipation become objective. Consequently the non-local theory lends itself perfectly to difficulties met in modelling local jumps in a strain field, and microscopic details in a heterogeneous media.

Non-local hardening models, as proposed by Bazant & Pijaudier-Cabot [1987, 1988] and Bazant & Feng-Bao [1988], are applications of the concept alluded to above. These models can be readily implemented into a finite element program without major modification. As such one just has to get into the subroutine where stress, strain and state variables are calculated and convert appropriate measures into the average distributional sense. However, the method still requires a very fine mesh and the choice of averaging techniques over the finite volume around a generic point is quite arbitrary.

Another technique used to avoid the vanishing localized zones is the concept of gradient limiters as applied for problems of large deformation, see Schreyer [1986] and

Triantafyllidis [1986]. The approach consists of accounting for localized deformation by adding a second order gradient dependent term to the expression of the strain energy density. The modified strain energy functions thus lead to equilibrium equations which always remain elliptic. This method can apparently give shear band directions and thickness in the post localization regime, and provides a unifying concept between pre and post localization regimes of deformation. However, these models limit themselves to fairly simple one dimensional stress and boundary conditions—extension to three dimensional stress conditions is not that obvious. Muhlhaus and Vardoulakis [1987] seems to have much success in dealing with a polar (Cosserat) medium with couple stresses which arise as a result of local rotation of the microstructure as the structure is deformed. The Cosserat approach retains second order terms in the description of the state of deformation, whereas the non-local continuum involves higher terms in its formulation. In the extreme case of fully localized mode, one resorts to fracture mechanics.

In the context of plasticity models, a very simple representative methodology consists of introducing the effects of microstructures through a homogenized (smeared) model which exhibits softening. The method involves the smearing of plastic localization over the entire solid in question. In essence, the localized solid is regarded as a continuous medium while the shear band is treated in an abstract manner by means of a strain softening constitutive law. The resulting plasticity model makes the hardening modulus mesh size dependent in a crude manner, as opposed to using the theory of distributions in non-local techniques. Procedures germane to this type of method have been used in models proposed by Pietruszczak & Mroz [1981] and Bicanic et al. [1985].

4.5 Proposed model

In the brief review, some of the most important issues on localization have been addressed and they seemingly are much well understood and appreciated in solid mechanics due to

existence of a fairly rational formalism. However, from a geomechanical stand-point, the manifestation of localization and its study are relatively new issues and have not yet aroused as much interest as in solid mechanics. As such, for instance, both correct mathematical and numerical descriptions of kinematics of a soil structure undergoing localized deformation are yet to emerge. By virtue of the nature of classical formulations which basically assume overall homogeneous deformations, conventional techniques used in geomechanics can be proven quite inadequate in expressing very local deformations.

Much of the current works include numerical models for which the finite element method is coaxed into predicting localization by using the smeared (homogenized) concept. This technique has proven to be quite effective and simple to implement into any finite element code, see for instance Tanaka and Kawamoto [1989]. However, little attention has been paid to the kinematical aspect which basically involves the discretization of a discontinuous field. It is well known that basic finite element techniques are hinged around continuum concepts by which all field variables are supposed to vary in a continuous manner. Models such as those proposed by Ortiz et. al. [1987] and Belytschko et. al. [1988] are attempts to enhance the deformational capabilities of ordinary finite elements by assuming a strain field which will replicate the deformation mode ensuing localization. However, though the deformational capability of the structure is enhanced, the basic formulation still hinges around a pseudo-smeared approach since controlling equations and interpolation functions are evaluated on an average sense, disregarding the discrete nature of the localized zone.

An interesting study, of the continuum type, was done by Burridge[1987] to model localized deformations in soil slopes. The original static problem is recast into a pseudo-dynamic one, and the resulting equations are solved by means of the finite difference technique. It is well-known that convergence towards reaching a stable finite element solution for the case of a structure following a softening material law can be ameliorated by the introduction of fictitious damping terms with the steady state solution being the

searched one. The finite difference scheme is attractive in the resolution of such problem in the sense that, according the solution scheme, one does not need to form the whole stiffness matrix—it suffices to solve each equation at a time in a decoupled fashion. Although this approach may work for some specific cases, its success heavily depends on the right amount of damping to be used, and the corresponding correct time step. Other restrictions concern the limitation to have regular grids and simple boundary conditions.

By way of contrast, the present study focuses on discrete discontinuities whose physical behaviour is formulated in a better manner. In precise terms, the essence of the model is as follows: failure occurs by the propagation of a shear band, here treated as a discontinuity surface, upon which relative sliding of the adjacent surfaces may lead to an on-going reduction of the material effective strength. The tip of the band, where the surface gives way to still intact material, advances in space with time and loading history. Initially it might appear logical to use an adaptive mesh to simulate the phenomenon by FEM, i.e., the location is made to coincide with the edges of the elements. However, the generation of meshes to fit the element topology with a moving band would impose a considerable penalty on the solution technique, if not make it intractable.

The approach adopted circumvents the problem by writing a modified principle of virtual work expression for a material body containing an internal discontinuity surface as known in classical continuum mechanics, Malvern [1969] and used for soil-pile interaction Boulon [1986]. A special element whose associated interpolation functions explicitly cater to discontinuities has been developed, obviating the need to update the mesh topology. The direction of the shear band will be predicted by a Mohr-Coulomb type criterion, but can be as well be governed by a bifurcation based equation, see for instance Vardoulakis [1980].

4.5.1 Problem formulation

Consider a singular line traversing a two dimensional domain as a continuous material line across which displacements are discontinuous. The lack of continuity in the displacement

field is a logical consequence of the loss of continuity between particles at damaged points and must be considered in some way whenever formulating the problem. It is understood that the local damage observed is still considered at the macroscopic level and it is not the intent of this thesis to go into details of micromechanics. In dealing with those discontinuities, the principle of virtual work will be amended as outlined in the subsequent sections. It is noted that all ensuing developments are based on the small strain theory because the study deals with initiation of localization. However, the formulations are by no means restrictive since they can be extended to large deformations.

4.5.2 Virtual work for displacement discontinuities

In the light of the derivation of incremental equilibrium equations for a material body traversed by a surface of displacement discontinuity, the classical principle of virtual work (PVW) is amended and conveniently recast into:

$$\int_{\Omega} \sigma_{ij} \delta\varepsilon_{ij} \, d\Omega = \int_{\Omega} f_i \delta u_i \, d\Omega + \int_{\Gamma_\sigma} \bar{T}_i \delta u_i \, d\Gamma + \int_{\Gamma_{sb}} t_i^{\dagger} \delta g_i \, d\Gamma, \tag{4.1}$$

in which σ_{ij} are Cauchy stresses, $\delta\varepsilon_{ij}$ associated virtual strains, f_i body forces, $\bar{T}_i$ prescribed boundary tractions along surface Γ_σ, $t_i^{\dagger}$ surface tractions at the internal discontinuity surface Γ_{sb} and δg_i associated virtual displacement jumps or slips. Note that $t_i^{\dagger}$ is an internal traction force which will be subsequently determined through a contact constitutive relationship. Equation (4.1) can be literally rephrased as: the work done by set of forces f_i and $\bar{T}_i$ exactly equals to the energy involved in deformation of the continuum and slip resistance along the discontinuity surface. It further describes the equation of equilibrium of a body traversed by a discontinuity surface and forms the basis of the governing equations in the proposed numerical model. As such, it permits localized plastic

deformation to occur along the discontinuity surface, as well as bulk plastic deformation of the ambient soil mass.

The last term introduced in Eq. (4.1) refers to virtual frictional work along Γ_{sb}, and it can be shown through the divergence theorem that it is the limiting form of the virtual work expression for a thin interface layer whose two parallel boundaries tend to coincide with each other. It is also interesting to note that this formulation avoids the undesirable feature of vanishing dissipation as the localized zone tends to zero because the work term is a surface integral which subsists even though volume reduces to zero.

4.5.3 Incremental virtual work equations

In order to capture the evolution (kinematics) of the physical behaviour of the shear band over time $[0,t]$, the foregoing equations of equilibrium are formulated in rate form. The evolution of the motion is considered as a sequence of equilibrium states assumed infinitesimally small so as to preclude effects of inertia, large deformations and rotational effects.

Using the modified PVW expression, equilibrium of the body in configuration $C^{(1)}$ requires that, see Figure 4.1 :

$$\int_{\Omega^t} \overset{\circ}{\sigma}_{ij}\,\delta(\Delta\varepsilon_{ij})\,\mathrm{d}\Omega = \int_{\Omega^t} f_i\,\delta(\Delta u_i)\,\mathrm{d}\Omega + \int_{\Gamma_\sigma} \bar{T}_i\,\delta(\Delta u_i)\,\mathrm{d}\Gamma + \int_{\Gamma_{sb}} t_i^1\,\delta(\Delta g_i)\,\mathrm{d}\Gamma. \tag{4.2}$$

At time t_2, equilibrium of configuration $C^{(2)}$ implies that

$$\int_{\Omega^t} (\sigma_{ij}+\Delta\sigma_{ij})\,\delta(\Delta\varepsilon_{ij})\,\mathrm{d}\Omega = \int_{\Omega^t} (f_i+\Delta f_i)\,\delta(\Delta u_i)\,\mathrm{d}\Omega + \int_{\Gamma_\sigma} (\bar{T}_i+\Delta\bar{T}_i)\,\delta(\Delta u_i)\,\mathrm{d}\Gamma + \int_{\Gamma_{sb}} (t_i^1+\Delta t_i^1)\,\delta(\Delta g_i)\,\mathrm{d}\Gamma. \tag{4.3}$$

Consider incremental deformations small so that piecewise linear material behaviour may be assumed, i.e.,

$$\Delta\sigma_{ij} = L_{ijkl}\Delta\varepsilon_{kl}, \quad \Delta t_i^1 = -\eta_{ij}\Delta g_j, \tag{4.4}$$

in which L_{ijkl} is a fourth order material constitutive tensor and η_{ij} a second order tensor describing a contact relationship linking normal and tangential tractions to conjugate displacement discontinuities along the shear band Γ_{sb}. For instance, as a simple case for the latter, the Coulomb friction law can be used. The rheology of the shear band will be examined in Chapter 5 and a framework for a generic contact law will be presented.

The incremental form of the modified PVW arises when Eqs. (4.4) are replaced into Eqs. (4.3) and (4.2) subtracted from the latter. The final expression recast in FE form reads:

$$\int_{\Omega^e} L_{ijkl}\Delta\varepsilon_{kl}\delta(\Delta\varepsilon_{ij})\,\mathrm{d}\Omega = \int_{\Omega^e} \Delta f_i\delta(\Delta u_i)\,\mathrm{d}\Omega + \int_{\Gamma_\sigma} \Delta\bar{T}_i\delta(\Delta u_i)\,\mathrm{d}\Gamma - \int_{\Gamma_{sb}} \eta_{ij}\Delta g_j\delta(\Delta g_i)\,\mathrm{d}\Gamma, \tag{4.5}$$

which involves global displacements u_i and slip displacements g_i.

4.5.4 Fluid flow through discontinuous medium

The deformation behaviour of a fluid saturated porous medium can be ideally considered as comprised of basically two main constituents: the solid grains and the pore fluids occupying the interconnected pore space. The interaction of the different constituents may

be suitably described by Terzaghi's concept [1923], i.e. the total stresses σ_{ij} acting on a plane through an average volume is decomposed into partial stresses such that:

$$\sigma'_{ij} = \sigma_{ij} + \alpha\delta_{ij}\,\pi, \tag{4.6}$$

in which the primed tensor refers to an effective value which controls the solid grain behaviour, δ_{ij} the Kronecker delta and π the pore fluid pressure. α is a coefficient interpreted by Biot [1941] as the ratio of fluid volume squeezed out to the volume change of porous medium if the latter is compressed while allowing the fluid to escape. It approaches unity for a fully saturated medium in which the fluid is considered totally incompressible. α will be considered equal to unity throughout subsequent derivations.

Consider the material body in Figure 4.1 subjected to a fluid flow regime as shown in Figure 4.2. Considering gravity induced forces $\boldsymbol{\gamma}$, the average pore fluid velocity v_i can be obtained through Darcy's law which states that flow is proportional to the fluid pore pressure gradient through the conductivity tensor k_{ij}, i.e.

$$v_i = -k_{ij}(\pi_{,j} + \gamma_j). \tag{4.7}$$

Note that the negative sign implies that the flow goes in the direction of decreasing gradient. It is herein assumed that Darcy's law still holds because the analysis is concerned with the initiation of the discontinuous surface. The continuity condition or conservation of mass ensures for a completely saturated system that the rate of average volume change exactly balances the amount of water flowing out, i.e.,

$$v_{i,i} + \dot{u}_{i,i} = 0. \tag{4.8}$$

Appendix A gives a complete derivation of the above expression which embeds several assumptions with regard to relative compressibilities of fluid and solid phases. Replacing Eq. (4.7) into Eq. (4.8) thus yields

$$-[k_{ij}(\pi_{,j} + \gamma_j)]_{,i} - \dot{u}_{i,i} = 0, \tag{4.9}$$

which must be satisfied inside the region $\Omega_1 \cup \Omega_2$ together with the following boundary conditions:

$$\pi = \overline{\pi} \text{ on } \Gamma_\pi \; ; v_i n_i = \overline{q} \text{ on } \Gamma_q \text{; and } [v_i^{(1)} - v_i^{(2)}] n_i^{(1)} = -\dot{g}_i n_i^{(1)} + \overline{q}_{sb} \text{ on } \Gamma_{sb}. \tag{4.10}$$

The term $\overline{q}_{sb}$ represents leak-off, i.e the rate of mass transfer of fluid from the porous adjacent medium to the shear band Γ_{sb}. Notice that if there is no variation in shear movement, i.e. $\dot{g}_i = 0$, the leak-off term is non-zero, and there is still flow transfer from the shear band to the ambient domain. In the continuous case where there is no shear band, the leak-off term loses its sense and it is understood that $\overline{q}_{sb}$ is zero.

From the same perspective as Terzaghi's principle of effective stresses, the effective internal traction vector, $\mathbf{t}'^1$, controlling the mechanical behaviour of the shear band may be written as

$$t_i'^1 = t_i^1 + \pi n_i^1. \tag{4.11}$$

While it is desirable to recast the problem into a variational statement for a numerical analysis, an alternate method consists of expressing the above problem into a weak form by conveniently choosing a hydraulically admissible field π^*. Applying the method of weighted residuals leads to the following integral statement in view of a finite element analysis:

$$\int_{\Omega} k_{ij}\pi_{,j}\,\delta\Delta\pi^{*}_{,i}\,d\Omega+\int_{\Omega}\dot{u}_{i,i}\,\delta(\Delta\pi^{*})\,d\Omega-\int_{\Gamma_{sb}}\left\{\dot{g}_i\,n^{1}_{i}-\overline{q}_{sb}\right\}\delta(\Delta\pi^{*})\,d\Gamma$$
$$=-\int_{\Omega}k_{ij}\gamma_{j}\,\delta\Delta\pi^{*}_{,i}\,d\Omega-\int_{\Gamma_{q}}\overline{q}\,\delta(\Delta\pi^{*})\,d\Gamma \tag{4.12}$$

$\forall\ \delta(\Delta\pi^{*})$ hydraulically admissible; $\Delta\pi^{*}=\Delta\pi$ (Bubnov-Galerkin method).

This formulation is an extended version of the flow equation for a continuous body in the sense that it caters to flow across and along an internal discontinuity surface. Also it can be shown that Eq (4.12) is an integral statement (weak form) which is equivalent to solving Eq. (4.9) inside the domain $\Omega_1 \cup \Omega_2$ subjected to boundary conditions displayed in Eq. (4.10), see appendix A.

Since the mechanical behaviour of a system due to effects of a change in stress is due only to changes in effective stresses, the equilibrium equation in Eq. (4.5) is recast with the aid of Eqs. (4.6) and (4.11) into:

$$\int_{\Omega}(\Delta\varepsilon_{kl}L_{ijkl}-\Delta\pi\delta_{ij})\delta\Delta\varepsilon_{ij}\,d\Omega+\int_{\Gamma_{sb}}(\eta_{ij}\Delta g_{j}-\Delta\pi n^{1}_{i})\delta\Delta g_{i}\,d\Gamma$$
$$=\int_{\Omega}\Delta f_{i}\,\delta\Delta u_{i}\,d\Omega+\int_{\Gamma_{\sigma}}\Delta\overline{T}_{i}\,\delta\Delta u_{i}\,d\Gamma, \tag{4.13}$$

$\forall\ \delta\Delta g_i$ and $\delta\Delta u_i$ kinematically admissible.

The classical flow-deformation coupling, as in consolidation problems, Biot [1941], naturally arises from equations (4.12) and (4.13) which describe fluid flow and mechanical behaviour respectively.

4.6 Finite element discretization

For the formulation of the approximate problem, the domain is discretized as a union of M discrete elements joined together at N global nodes and intersected at NL localized nodes, where are defined respectively displacement and slip displacement degrees of freedom.

Figure 4.3 shows the discretized domain with the locus of the localized nodes which eventually describes the geometry of the shear band during its progression in the deformation history. The addition of fluid pore pressure degrees of freedom at all nodes thus completes the entire field variable description.

4.6.1 Displacement field interpolation

In order to approximate the problem, a finite element subspace is conveniently defined using piecewise polynomial basis functions. As such, the displacement field over an elemental volume Ω^e is approximated using a smooth basis for displacements $\mathbf{u}$, and a discontinuous one for slip displacements $\mathbf{g}$. Interpolation of $\mathbf{u}$ in terms of nodal values (barred variables) can be written as

$$u_i(\mathbf{x}) = \sum_{a=1}^{N} N_a^{(\alpha)}(\mathbf{x})\,\bar{u}_{ia} + \sum_{a=1}^{NL} N_a^{(\beta)}(\mathbf{x})\,\bar{g}_{ia}. \tag{4.14}$$

Note that the subscript i ranges from 1 to 2 for a two-dimensional space. In compact symbolic notation, the incremental form of Eq. (4.14) is given as:

$$\Delta\mathbf{u} = \mathbf{N}^{(\alpha)} \cdot \Delta\bar{\mathbf{u}} + \mathbf{N}^{(\beta)} \cdot \Delta\bar{\mathbf{g}}, \tag{4.15}$$

in which $\Delta\bar{\mathbf{u}}$ is the vector of incremental nodal displacements, $\Delta\bar{\mathbf{g}}$ vector of incremental slip displacements at localized *nodes*, and $\mathbf{N}^{(\alpha)}$, $\mathbf{N}^{(\beta)}$ associated matrices of interpolation polynomials. Super-indices α and β refer to continuous and discontinuous components respectively. The associated incremental strains can be formally computed from kinematic conditions as follows:

$$\Delta\boldsymbol{\varepsilon} = \mathbf{B}^{(\alpha)} \cdot \Delta\bar{\mathbf{u}} + \mathbf{B}^{(\beta)} \cdot \Delta\bar{\mathbf{g}}, \tag{4.16}$$

with $\mathbf{B}^{(\alpha)}$ and $\mathbf{B}^{(\beta)}$ as compatibility matrices. The derivation of interpolation functions $\mathbf{N}^{(\alpha)}$ and $\mathbf{N}^{(\beta)}$ is presented in the subsequent sections.

4.6.2 Pore fluid pressure field interpolation

The fluid pore pressure field is interpolated by a smooth linear polynomial basis in the following fashion:

$$\Delta\boldsymbol{\pi} = \mathbf{H} \cdot \Delta\overline{\boldsymbol{\pi}}, \tag{4.17}$$

in which $\Delta\overline{\boldsymbol{\pi}}$ is the vector of incremental nodal pressures, and $\mathbf{H}$ the associated matrices of interpolation polynomials. The incremental pore fluid pressure gradient naturally emerges as:

$$\Delta\boldsymbol{\pi}_{,i} = \text{grad}(\Delta\boldsymbol{\pi}) = \mathbf{B}^{H} \cdot \Delta\overline{\boldsymbol{\pi}}, \tag{4.18}$$

with $\mathbf{B}^{H}$ the hydraulic compatibility matrix.

4.7 Derivation of discontinuous interpolation functions

As presented in the previous section, the idea of expressing the displacement at a generic material point in terms of a continuous component and a disturbance term which accounts for the presence of a discontinuity surface leads to the derivation of suitable interpolation polynomials $\mathbf{N}^{(\alpha)}$ and $\mathbf{N}^{(\beta)}$. To this end a special type of element has been developed which allows for internal discontinuities in the displacement field. By the use of such special elements, herein coined as discontinuous elements, it is possible to use a fixed grid and have the discontinuity surface move through it without any mesh update.

4.7.1 1-D discontinuous piecewise linear interpolation function

Consider the function u defined on the 1-D domain $[0,L] = \{x \in \Re / 0 \le x \le L\}$ as shown in Figure 4.4a. Let $u(0)=u_1$ and $u(L)=u_2$, while u suffers a jump discontinuity at $x=a$. However u is still continuous over $x \in [0,a[$ and $x \in]a, L[$. If one envisions the union of several of these domains $[0, L[$ in the sense of the finite element method, it is seen that one will be still treating with a globally C^0 function. As one wants to maintain compatibility in slope at the discontinuity point, in other words, $(du/dx)_{a^-} = (du/dx)_{a^+}$, this physically implies that the strain distribution above and below the discontinuity surface is kept the same for simplicity, see Figure 4.4b for a 2-dimensional configuration. Consequently for $x \in [0,a[$, the displacement function $u(x)$ can be expressed solely in terms of u_1 and u_2 by merely extending the linear portion defined by u_1 and u_3. Thus,

$$u(x) = (1-\frac{x}{L})u_1 + \frac{x}{L}u_2 - \frac{x}{L}g. \tag{4.19}$$

Similarly for $x \in]a,0[$, the function u can be written as

$$u(x) = (1-\frac{x}{L})u_1 + \frac{x}{L}u_2 + (1-\frac{x}{L})g. \tag{4.20}$$

If the coordinate transformation $\xi = \frac{2x}{L} - 1$ is performed, the expressions of u in terms of local coordinates ξ become:

$$u^-(\xi) = \frac{(1-\xi)}{2}u_1 + \frac{(1+\xi)}{2}u_2 - \frac{(1+\xi)}{2}g, \tag{4.21}$$

and

$$u^+(\xi) = \frac{(1-\xi)}{2}u_1 + \frac{(1+\xi)}{2}u_2 + \frac{(1-\xi)}{2}g. \tag{4.22}$$

The super-index '+' refers to the plus side of the discontinuity line and '−' to the minus side. The interpolation functions $\mathbf{N}^{(\alpha)}$ and $\mathbf{N}^{(\beta)}$ can be now easily identified from Eqs. (4.21) and (4.22), at least in the one-dimensional case, i.e.

$$N_1^{(\alpha)^-}(\xi) = N_1^{(\alpha)^+}(\xi) = \frac{(1-\xi)}{2}, \quad N_2^{(\alpha)^-}(\xi) = N_2^{(\alpha)^+}(\xi) = \frac{(1+\xi)}{2}, \tag{4.23}$$

$$N_1^{(\beta)^-}(\xi) = -\frac{(1+\xi)}{2}, \quad N_1^{(\beta)^+}(\xi) = \frac{(1-\xi)}{2}. \tag{4.24}$$

Both the continuous and resulting discontinuous interpolation shape functions are illustrated in Figure 4.5.

It is interesting to notice that if g is set to zero in Eqs. (4.21) and (4.22), the interpolation scheme reverts to a continuous one. Also, the basis functions $\mathbf{N}^{(\beta)}$ vanish at $x = 0$ and $x = L$. Their values at any point inside the domain are uniquely determined by the values of the discontinuous interpolant once the position of the discontinuity front $x=a$ is located. A higher order interpolation function can be further derived using similar procedure or more elegantly by means of concepts of hierarchical shape functions.

4.7.2 4-node discontinuous quadrilateral element QD4

This section is addressed to the derivation of the field function with a simple discontinuity in a piecewise local finite element representation for the family of isoparametric elements. It is found that some geometric complexities are involved in determining the way the discontinuity line cuts the element sides. Figure 4.6 illustrates the two master configurations which account for all geometric possibilities of the discontinuity location in the element. The position of the discontinuity front is defined by localized nodes a and b found on element edges. Any other configuration is simply obtained by local cyclic permutation of node numbers.

The piecewise linear local approximation has been previously derived for the one-dimensional case and the concept will be extended to a two-dimensional situation. The derivation of interpolation functions $\mathbf{N}^{(\alpha)}$ and $\mathbf{N}^{(\beta)}$ have been performed in the following way. Functions suffering a discontinuity along element boundaries crossed by a discontinuity line are found and interpolated linearly for the interior through blending techniques, see Zienkiewicz and Morgan [1983]. The mapped function which interpolates the displacement field anywhere inside the element has the following form:

• for domain Ω_2^e, i.e on the plus side of Γ_{sb},

$$\begin{aligned} u^+(\xi,\eta) = \; & \frac{1}{4}(1-\xi)(1-\eta)\,u_1 + \frac{1}{4}(1+\xi)(1-\eta)\,u_2 \\ & + \frac{1}{4}(1+\xi)(1+\eta)\,u_3 + \frac{1}{4}(1-\xi)(1+\eta)\,u_4 \\ & - \frac{1}{4}(1-\xi)(1+\eta)\,g_1 - \frac{1}{4}(1+\xi)(1+\eta)\,g_2. \end{aligned} \tag{4.25}$$

or

$$u^+(\xi,\eta) = N_1^{(\alpha)}u_1 + N_2^{(\alpha)}u_2 + N_3^{(\alpha)}u_3 + N_4^{(\alpha)}u_4 + N_1^{(\beta)^+}g_1 + N_2^{(\beta)^+}g_2. \tag{4.26}$$

g_1 and g_2 are the magnitude of the displacement jumps at locations a' and b' respectively.

• for domain Ω_1^e, i.e on the minus side of Γ_{sb},

$$u^-(\xi,\eta) = N_1^{(\alpha)}u_1 + N_2^{(\alpha)}u_2 + N_3^{(\alpha)}u_3 + N_4^{(\alpha)}u_4 + N_1^{(\beta)^-}g_1 + N_2^{(\beta)^-}g_2. \tag{4.27}$$

where

$$N_1^{(\beta)^-} = \frac{1}{4}(1-\xi)(1-\eta),\; N_2^{(\beta)^-} = \frac{1}{4}(1+\xi)(1-\eta). \tag{4.28}$$

The shape functions $N_i^{(\alpha)}$ are the serendipity type functions. Figure 4.7 depicts the geometrical representation of the class of discontinuous piecewise locally linear functions $N_i^{(\beta)}$.

The derivation of suitable shape functions for option 2 is more delicate to treat than the previous case since one needs to break down the quadrilateral into two constants strain triangles, and construct the associated discontinuity functions. Figure 4.8 illustrates the resulting discontinuous interpolation function for a 3-node triangular element.

The final forms of the displacement function interpolation for the constant strain triangle are given as

$$u^{+}(\xi,\eta) = [N_1(1-\lambda_a) + N_4(1-\lambda_b)]u_1 + [N_1\lambda_a + N_2]u_2 + [N_3 + N_4\lambda_b]u_3 + (\lambda_a - 1)N_1 g_1 + (\lambda_b - 1)N_4 g_2. \tag{4.29}$$

in which

$$N_1^{(\alpha)^+} = N_1(1-\lambda_a) + N_4(1-\lambda_b), \tag{4.30 a}$$

$$N_2^{(\alpha)^+} = N_1\lambda_a + N_2, \tag{4.30 b}$$

$$N_3^{(\alpha)^+} = N_3 + N_4\lambda_b, \tag{4.30 c}$$

$$N_1^{(\beta)^+} = (\lambda_a - 1)N_1, \tag{4.30 d}$$

$$N_2^{(\beta)^+} = (\lambda_b - 1)N_4, \tag{4.30 e}$$

where

$$N_1 = \frac{1}{4}(1-\xi)(1-\eta), \tag{4.31 a}$$

$$N_2 = \frac{1}{4}(1+\xi)(1-\eta), \tag{4.31 b}$$

$$N_3 = \frac{1}{4}(1+\xi)(1+\eta), \tag{4.31 c}$$

$$N_4 = \frac{1}{4}(1-\xi)(1+\eta). \tag{4.31 d}$$

ξ, η are the local coordinates of the system in which quadri-rectangular domain Ω_1^e, Fig. 4.6, is mapped onto. Similarly, displacement in the domain Ω_2^e is given as

$$u^{-}(L_1,L_2,L_3) = [L_1 + L_2(1-\lambda_a) + L_3(1-\lambda_b)]u_1 + L_2\lambda_a u_2 + L_3\lambda_b u_3 + L_2\lambda_a g_1 + L_3\lambda_b g_2. \tag{4.32}$$

where L_1, L_2, L_3 are the area coordinates of the triangular domain Ω_2^e.

4.8 Governing finite element equations

Linearizing Eqs. (4.12) and (4.13) with the aid of Eqs. (4.15), (4.16), (4.17), and (4.18) leads, after some algebra, to the following set of homogeneous matricial equation:

$$\begin{bmatrix} \mathbf{K}_{\Omega\Omega} & \mathbf{K}_{\Omega S} & \mathbf{K}_{\Omega H} \\ \mathbf{K}_{S\Omega} & \mathbf{K}_{SS} & \mathbf{K}_{SH} \\ \mathbf{K}_{H\Omega} & \mathbf{K}_{HS} & \mathbf{K}_{HH} \end{bmatrix} \begin{Bmatrix} \Delta\overline{\mathbf{u}} \\ \Delta\overline{\mathbf{g}} \\ \Delta\overline{\boldsymbol{\pi}} \end{Bmatrix} = \begin{Bmatrix} \Delta\mathbf{f}_\Omega \\ \Delta\mathbf{f}_S \\ \Delta\mathbf{G}_H \end{Bmatrix}, \tag{4.33}$$

in which

$$\mathbf{K}_{\Omega\Omega} = \int_\Omega \mathbf{B}^{(\alpha)^T} : \mathbf{L} : \mathbf{B}^{(\alpha)}\, d\Omega \; ; \mathbf{K}_{\Omega S} = \int_\Omega \mathbf{B}^{(\alpha)^T} : \mathbf{L} : \mathbf{B}^{(\beta)}\, d\Omega \; ; \; \mathbf{K}_{\Omega H} = -\int_\Omega \mathbf{H}^T : (\hat{\mathbf{m}}^T \cdot \mathbf{B}^{(\alpha)}) d\Omega \; ;$$

$$\mathbf{K}_{S\Omega} = \int_\Omega \mathbf{B}^{(\beta)^T} : \mathbf{L} : \mathbf{B}^{(\alpha)}\, d\Omega \; ; \mathbf{K}_{SS} = \int_\Omega \mathbf{B}^{(\beta)^T} : \mathbf{L} : \mathbf{B}^{(\beta)}\, d\Omega + \int_{\Gamma_{sb}} \mathbf{N}^{(\beta)^T} \cdot \boldsymbol{\eta} \cdot \mathbf{N}^{(\beta)}\, d\Gamma \; ;$$

$$\mathbf{K}_{SH} = -\int_\Omega \mathbf{H}^T : (\hat{\mathbf{m}}^T \cdot \mathbf{B}^{(\beta)})\, d\Omega - \widetilde{\int_{\Gamma_{sb}}} \mathbf{H}^T : (\mathbf{n}^T \cdot \mathbf{N}^{(\beta)})\, d\Gamma \; ; \quad \hat{\mathbf{m}}^T = \langle 1, 1, 1, 0, 0, 0 \rangle,$$

$$\mathbf{K}_{H\Omega} = \int_\Omega (\mathbf{B}^{(\alpha)^T} \hat{\mathbf{m}}) : \mathbf{H}\, d\Omega \; ; \; \mathbf{K}_{HS} = -\int_\Omega (\mathbf{B}^{(\beta)^T} \hat{\mathbf{m}}) : \mathbf{H}\; d\Omega - \int_{\Gamma_{sb}} (\mathbf{N}^{(\beta)^T} \cdot \mathbf{n}) : \mathbf{H}\; d\Gamma;$$

$$\mathbf{K}_{HH} = \theta \Delta t \int_\Omega \mathbf{B}^{H^T} : \mathbf{k} : \mathbf{B}^H\, d\Omega \; ; \; \Delta\mathbf{G}_H = (\mathbf{G}_{n-1} + \theta\, \Delta\mathbf{G}_n)\Delta t - \frac{\overline{\boldsymbol{\pi}}_{n-1}}{\theta} \int_\Omega \mathbf{B}^{H^T} : \mathbf{k} : \mathbf{B}^H\; d\Omega \; ;$$

in which $0 \le \theta \le 1$ and

$$\mathbf{G}_n = -\int_\Omega \mathbf{B}^{H^T} : \mathbf{k} : \boldsymbol{\gamma}\, d\Omega - \int_{\Gamma_q} \mathbf{H}^T \cdot \overline{\mathbf{q}}\; d\Gamma - \int_{\Gamma_{sb}} \mathbf{H}^T \cdot \overline{\mathbf{q}}_{sb}\, d\Gamma;$$

and **k** is the conductivity tensor.

$$\Delta \mathbf{f}_{\Omega} = \int_{\Omega} \mathbf{N}^{(\alpha)^{\mathrm{T}}} \cdot \Delta \mathbf{f}\, d\Omega + \int_{\Gamma_{\sigma}} \mathbf{N}^{(\alpha)^{\mathrm{T}}} \cdot \Delta \overline{\mathbf{T}}\, d\Gamma\ ;$$

$$\Delta \mathbf{f}_{S} = \int_{\Omega} \mathbf{N}^{(\beta)^{\mathrm{T}}} \cdot \Delta \mathbf{f}\, d\Omega + \int_{\Gamma_{\sigma}} \mathbf{N}^{(\beta)^{\mathrm{T}}} \cdot \Delta \overline{\mathbf{T}}\, d\Gamma.$$

Since the treatment of the complete coupled problem is outside the scope of the present paper, and plays no important role in the mathematical development of the localization problem, the elaboration of the fluid phase is omitted and attention is confined to the drained case. Therefore submatrices $K_{\Omega\Omega}, K_{\Omega S}, K_{S\Omega}$ and K_{SS} are the only partitions retained in the global matrix.

4.9 Convergence of enhanced strain field scheme

The use of a discontinuous strain field which replicates the deformational patterns following localization should not reduce the order of convergence of the finite element scheme. For purposes of illustration and ease of demonstration, the case of linear elasticity will be closely examined as a model problem. In this respect there always exist potential functions from which stresses and internal tractions are derived. Extension to the non-linear case such as elasto-plasticity can be accommodated by simply splitting the terms into linear and non-linear parts representing stored and irrecoverable energies respectively.

As can be deduced from Eq. (4.5) in the ease of elastic bodies undergoing small deformations, the displacement field **u** and slip displacements **g** along an internal boundary minimizes the strain energy potential

$$\Phi(\mathbf{u},\mathbf{g}) = \int_{\Omega} W(\boldsymbol{\varepsilon})\, d\Omega + \int_{\Gamma_{sb}} w(\mathbf{g})\, d\Gamma - \int_{\Omega} \mathbf{f}\cdot\mathbf{u}\, d\Omega - \int_{\Gamma_{\sigma}} \overline{\mathbf{T}}\cdot\mathbf{u}\, d\Gamma, \tag{4.34}$$

under suitable boundary conditions and restrictions on the domain of analysis. The function W is the strain energy density of the material and w the surface strain energy of the internal discontinuity, which in the linear case take the following forms

$$W(\boldsymbol{\varepsilon}) = \frac{1}{2} D_{ijkl}\, \varepsilon_{ij}\, \varepsilon_{kl}, \tag{4.35}$$

$$w(\mathbf{g}) = \frac{1}{2} \eta_{ij}\, g_i\, g_j, \tag{4.36}$$

for some material elastic moduli $\mathbf{D}$ and discontinuity surface elastic contact tensor $\boldsymbol{\eta}$. Considering the spatial discretization of Ω into a finite element mesh, i.e. $\{\Omega^e, e=1,N\} \cup \{\Gamma^e_{sb}, e=1,NL\}$ as introduced in Section 4.6.1 and Eq. (4.14), the discretized potential takes the following form:

$$\begin{aligned}\Phi(\mathbf{u}_h,\mathbf{g}_h) = &\sum_{e=1}^{N} \int_{\Omega^e} W\Big(\boldsymbol{\varepsilon}\Big(\sum_{a=1}^{N} N_a^{(\alpha)} \overline{\mathbf{u}}_a + \sum_{a=1}^{N} N_a^{(\beta)} \overline{\mathbf{g}}_a\Big)\Big)\, d\Omega^e \\ &+ \sum_{e=1}^{NL} \int_{\Gamma_{sb}} w\Big(\sum_{a=1}^{NL} N_a^{(\beta)} \overline{\mathbf{g}}_a\Big)\, d\Gamma^e - \sum_{e=1}^{N} \int_{\Omega^e} \mathbf{f}\cdot\Big(\sum_{a=1}^{N} N_a^{(\alpha)} \overline{\mathbf{u}}_a + \sum_{a=1}^{NL} N_a^{(\beta)} \overline{\mathbf{g}}_a\Big)\, d\Omega^e \\ &- \sum_{e=1}^{N} \int_{\Gamma_{\sigma}} \overline{\mathbf{T}}\cdot\Big(\sum_{a=1}^{N} N_a^{(\alpha)} \overline{\mathbf{u}}_a + \sum_{a=1}^{NL} N_a^{(\beta)} \overline{\mathbf{g}}_a\Big)\, d\Gamma^e,\end{aligned} \tag{4.37}$$

in which $\mathbf{u}_h$ and $\mathbf{g}_h$ are approaching functions of $\mathbf{u}$ and $\mathbf{g}$ respectively. Minimization of this potential yields the sought nodal displacements and localized nodal slip displacements. The strains can be obtained from the associated displacements through the discretized strain operators (compatibility matrices $\mathbf{B}^{(\alpha)}$ and $\mathbf{B}^{(\beta)}$) over each side of the discontinuity front as

$$\boldsymbol{\varepsilon} = \mathbf{B}^{(\alpha)} \cdot \mathbf{u} + \mathbf{B}^{(\beta)} \cdot \mathbf{g} \tag{4.38}$$

It is noted that the structure of the above equation is very similar to that encountered for a non-conforming element. The term $\mathbf{B}^{(\beta)}.\mathbf{g}$ plays the role of non-conforming modes which are added to the basic ones represented by $\mathbf{B}^{(\alpha)}.\mathbf{u}$. However, in order not to reduce the order of the element convergence with respect to the primal variable $\mathbf{u}$, the assumed operator $\mathbf{B}^{(\beta)}$ must comply with the following two well-known conditions, see Zienkiewicz and Taylor[1989]:

(i) **Stability:** The stiffness matrix has to be non-singular for all possible assemblies of element, and thus ensures that the discrete solution is unique. Also by the same token, one avoids spurious mechanisms—occurrence of zero eigenvalues, or zero diagonals in the Crout factorization of the stiffness matrix—which may pollute the solution for all sizes of the element. For instance, if the displacement field is rigid or in accord with a constant strain condition, the assumed strain operator must vanish identically;

(ii) **Consistency**: As the size of the element tends to zero, the variational principle should yield the exact solution of the problem. In other words, the assumed strain operator must coincide with the compatible strain operator in the variational statement for all displacement fields in P_k, complete polynomials of order k.

- **Proof of stability**

Consider the discretized form of the stationary potential energy as previously given in Eq. (4.41) with fluid components suppressed, i.e.

$$\begin{bmatrix} \mathbf{K}_{\Omega\Omega} & \mathbf{K}_{\Omega S} \\ \mathbf{K}_{S\Omega} & \mathbf{K}_{SS} \end{bmatrix} \begin{Bmatrix} \mathbf{u} \\ \mathbf{g} \end{Bmatrix} = \begin{Bmatrix} \mathbf{f}_{\Omega} \\ \mathbf{0} \end{Bmatrix}. \tag{4.39}$$

For the shear band element to pass the patch test, it is required that the slip degrees of freedom **g** be zero whenever the global displacement **u** corresponds to rigid body motions or constant strain conditions. If $\mathbf{u}_0$ is defined as the set of nodal displacements corresponding to one of the above conditions, then $\mathbf{g}_0$ can be computed from the second set of equations obtained in Eq. (4.33). Accordingly,

$$\mathbf{g}_0 = -\mathbf{K}_{ss}^{-1}\mathbf{K}_{s\Omega}\mathbf{u}_0. \tag{4.40}$$

Since the contact constitutive relationship is derived from a strain energy potential, the matrix $\mathbf{K}_{ss}^{-1}$ is necessarily positive definite. As a result, to obtain zero slip displacements $\mathbf{g}_0$, the term $\mathbf{K}_{s\Omega}\cdot\mathbf{u}_0$ has to vanish, i.e.

$$\int_{\Omega}\mathbf{B}^{(\beta)^T}:\mathbf{D}:\mathbf{B}^{(\alpha)}\cdot\mathbf{u}_0\ d\Omega = 0. \tag{4.41}$$

The above certainly holds true for a rigid body motion because the term $\mathbf{D}:\mathbf{B}^{(\alpha)}.\mathbf{u}_0$, basically a stress $\boldsymbol{\sigma}_0$, is necessarily zero. In other words, this ensures that no zero energy modes will be obtained when the mesh is restrained from any rigid body motion. For a constant strain condition, the stress $\boldsymbol{\sigma}_0$ is constant, and in order to satisfy Eq. (4.41), the assumed strain operator could vanish trivially, i.e.

$$\int_{\Omega}\mathbf{B}^{(\beta)^T}d\Omega \equiv 0. \tag{4.42}$$

- **Proof of consistency**

If the approximate solution is to approach the exact solution as h tends to zero, the truncation error of all terms in the variational principle must be of order h^n with $n \geq 1$. In other words, the approximation of the displacement field **u** must have a basis that is at least

complete to the order k if the highest derivative of $\mathbf{u}$ is of order k. The approximation of $\mathbf{u}^e$ over a shear band element must at least contain a complete linear basis, i.e $k=1$ as can be seen from the strain energy potential given in Eq. (4.34).

The use of an interpolation scheme in accord with a bilinear variation of displacements over the element, and the prescription of a linear variation of slip displacements along the shear band ensures the consistency condition. Moreover, the consistency requirement will be readily verified in Chapter 7 by means of the patch test.

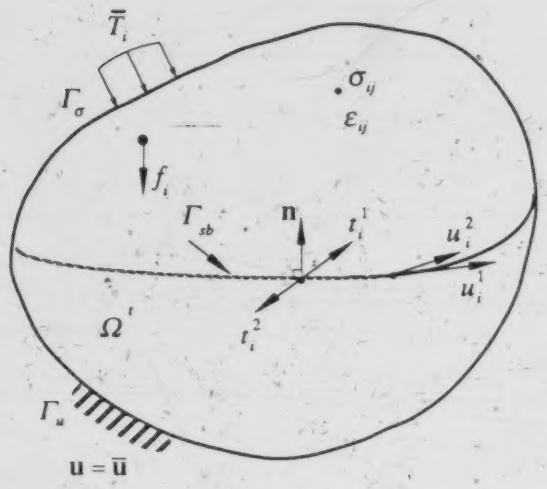

$$\Gamma = \Gamma_\sigma \cup \Gamma_u$$
$$\Gamma_\sigma \cap \Gamma_u = \varnothing$$

$$\delta g_i = \delta u_i^1 - \delta u_i^2$$

time t_1
configuration $C^{(1)}$

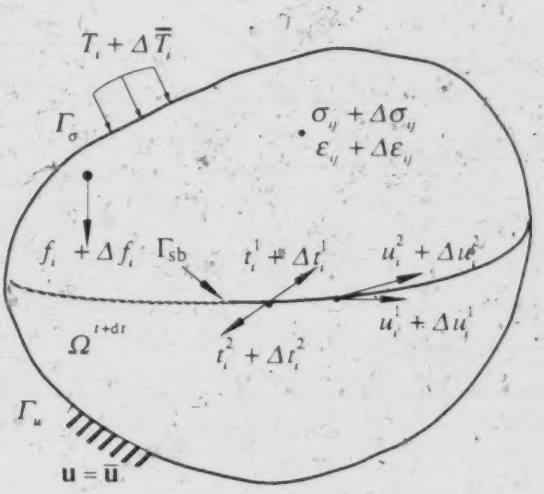

time $t_1 + dt_1$
configuration $C^{(2)}$

Figure 4.1. Description of motion

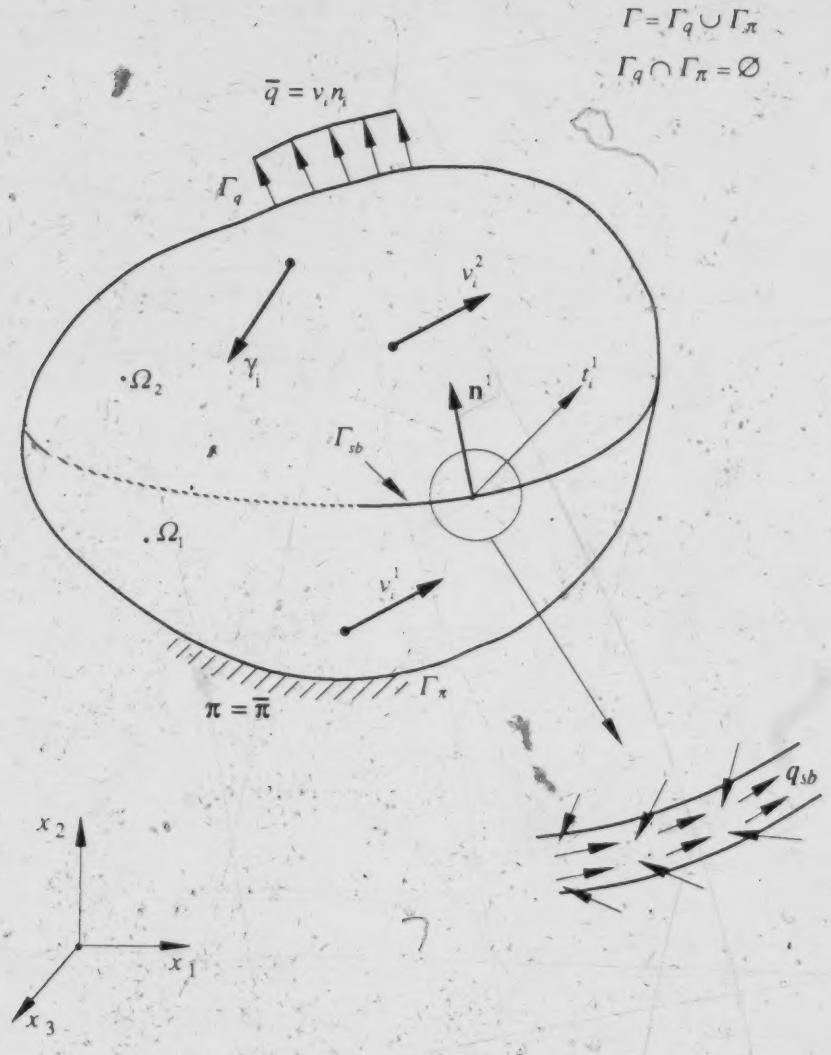

Figure 4.2. Fluid flow through discontinuous medium

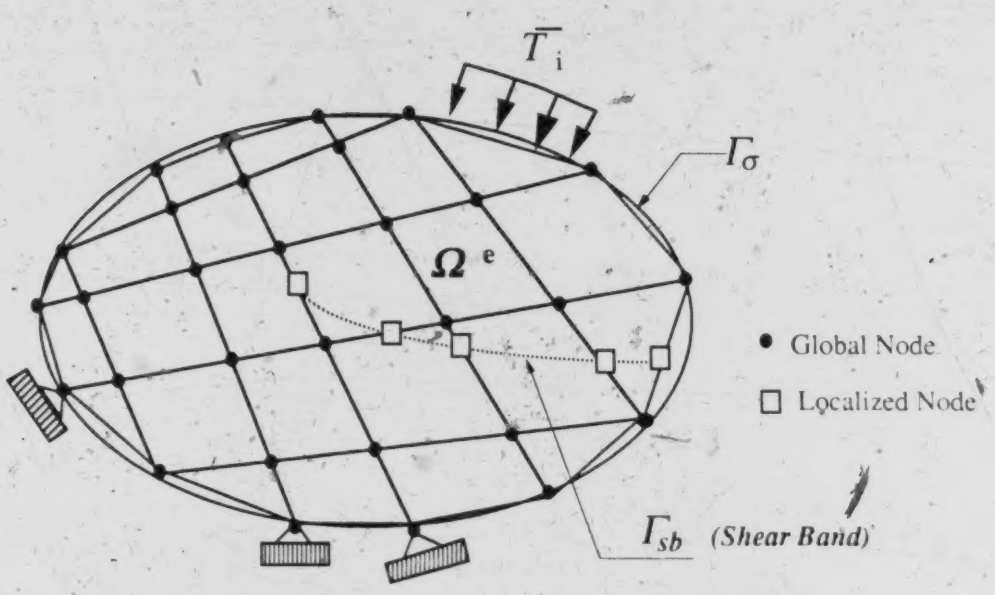

Figure 4.3 Finite element discretization of domain

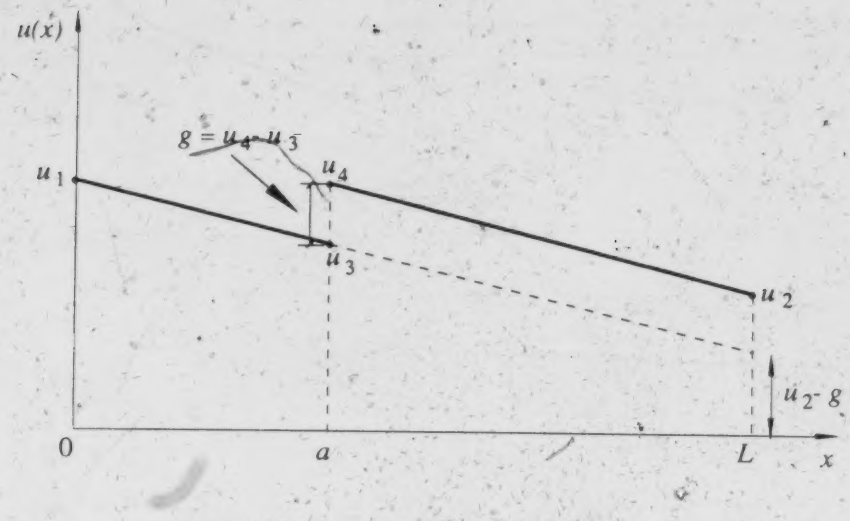

Figure 4.4a. 1-D discontinuous interpolation function

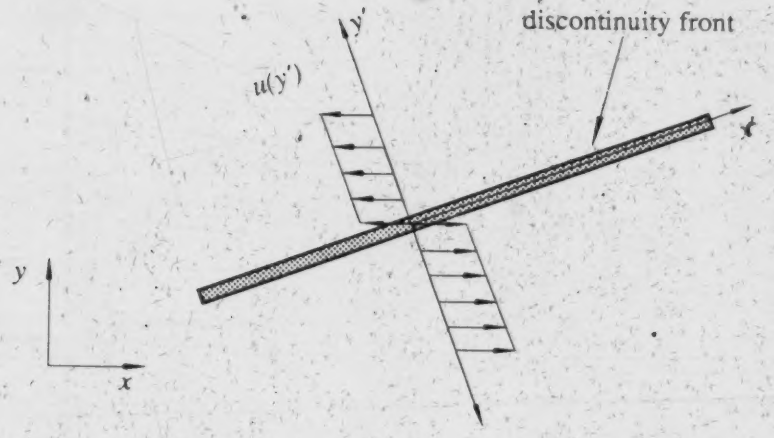

Figure 4.4b. Distribution of displacement across a shear band

Continuous interpolation function $N^{(\alpha)}$

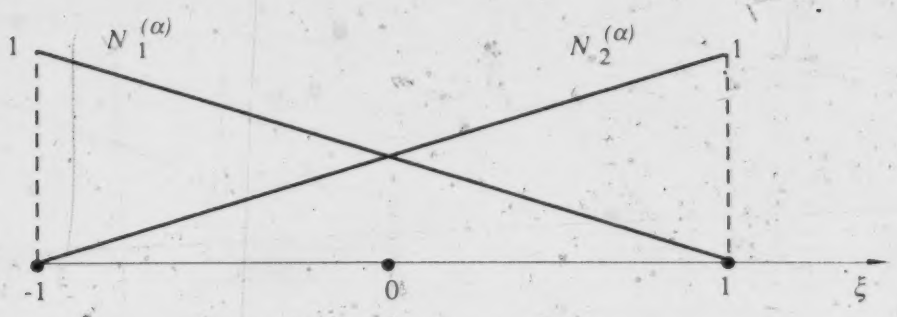

Discontinuous interpolation function $N^{(\beta)}$

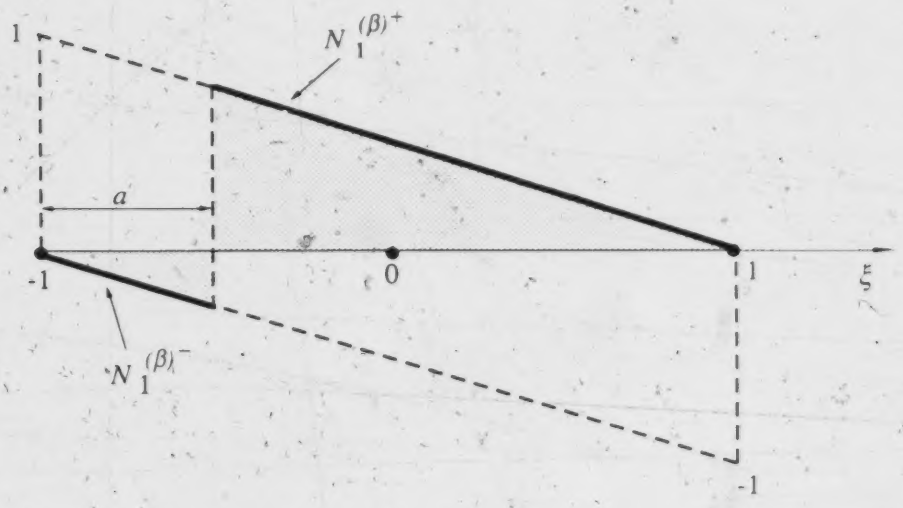

Figure 4.5 Geometrical description of 1-D discontinuous interpolation shape functions

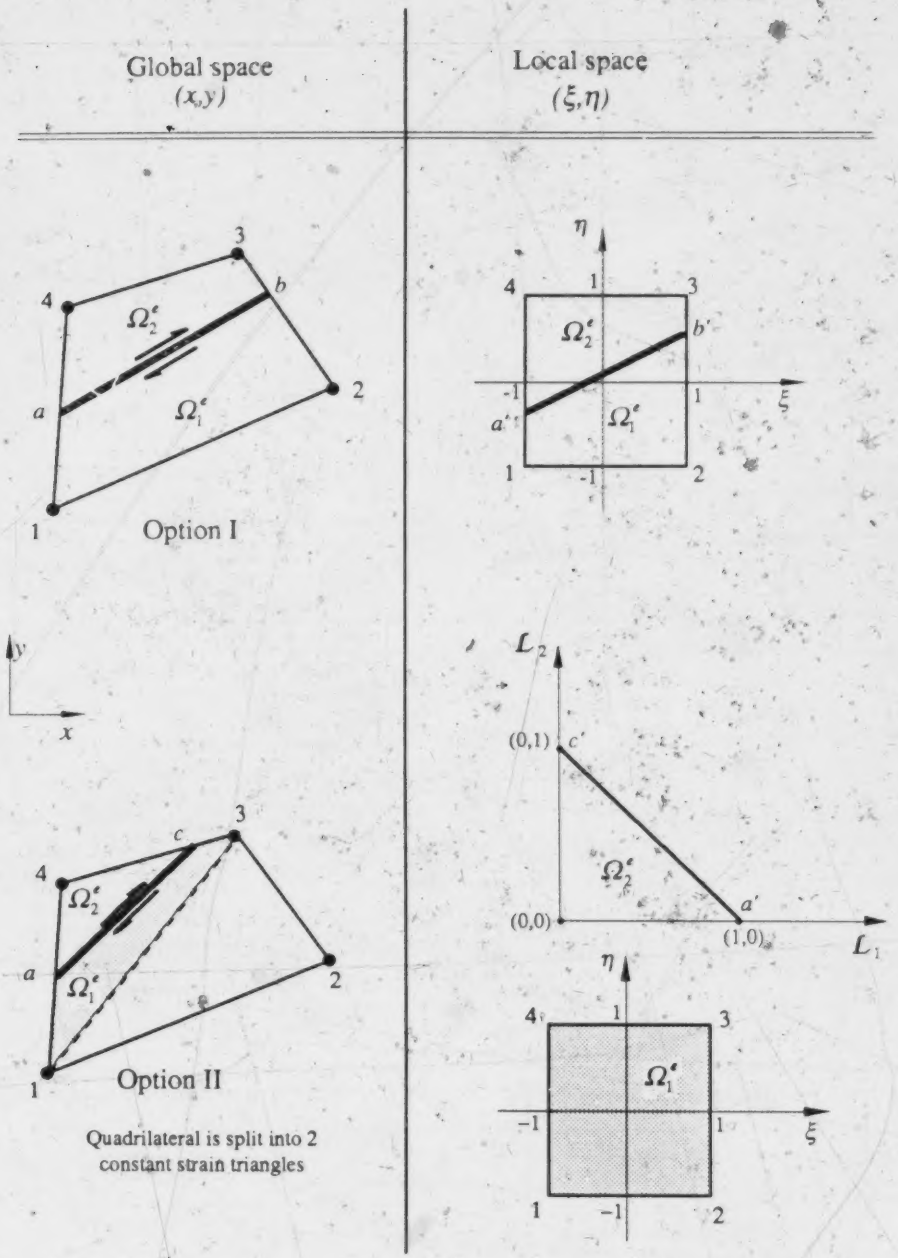

Figure 4.6 Master element configurations for QD4 elements

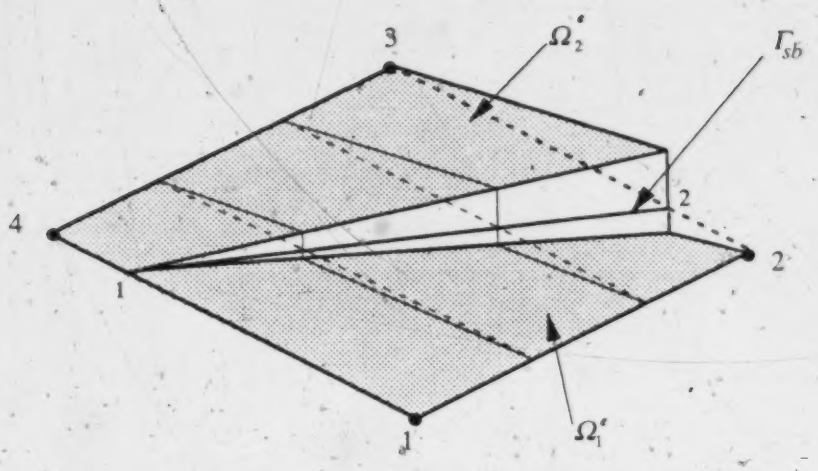

$$\text{for } (\xi,\eta) \in \Gamma_{sb}^{+} \quad N_2^{(\beta)^+} = \frac{1}{4}(1-\eta)(1+\xi)$$

$$\text{for } (\xi,\eta) \in \Gamma_{sb}^{-} \quad N_2^{(\beta)^-} = -\frac{1}{4}(1+\eta)(1+\xi)$$

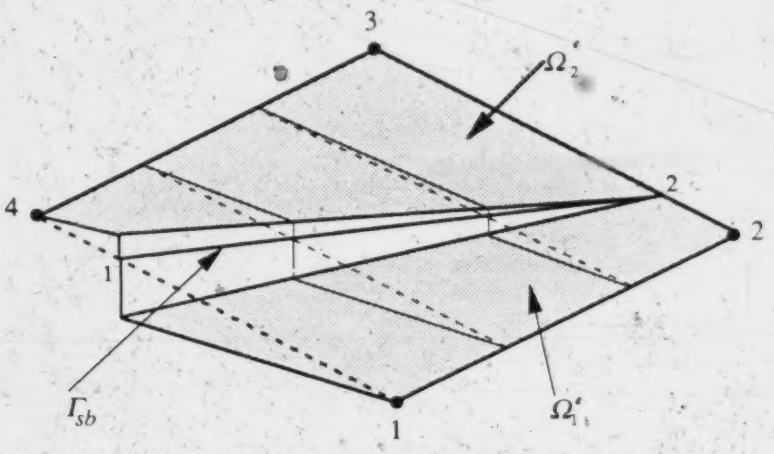

$$\text{for } (\xi,\eta) \in \Gamma_{sb}^{+} \quad N_1^{(\beta)^+} = \frac{1}{4}(1-\eta)(1-\xi)$$

$$\text{for } (\xi,\eta) \in \Gamma_{sb}^{-} \quad N_1^{(\beta)^-} = -\frac{1}{4}(1+\eta)(1-\xi)$$

Figure 4.7 Discontinuous shape functions for a 4-node quadrilateral element

λ_a and λ_b define the intersection locations of the band with element edges

Domain I Ω_1^e

$N_1^{(\beta)} = (\lambda_a - 1)N_1$

$N_2^{(\beta)} = (\lambda_b - 1)N_2$

L_i area coordinates

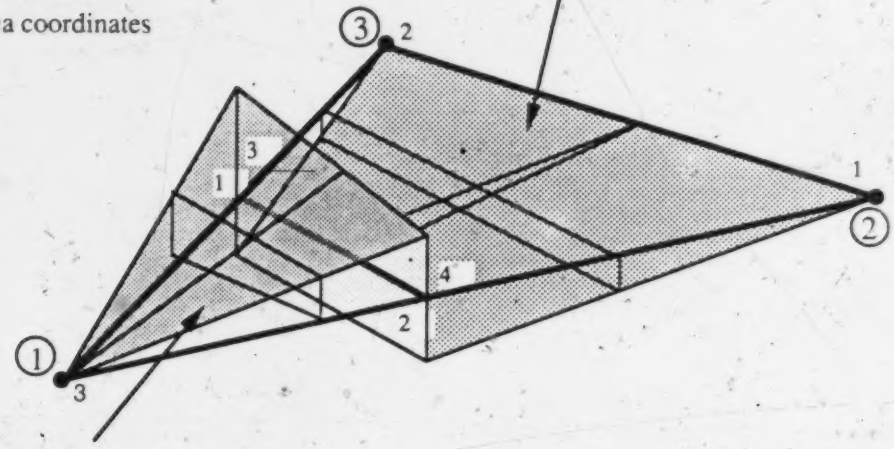

Domain II Ω_2^e

$N_1^{(\beta)} = L_2\lambda_a$

$N_2^{(\beta)} = L_3\lambda_b$

$$N_1 = \frac{1}{4}(1-\xi)(1-\eta)$$

$$N_4 = \frac{1}{4}(1-\xi)(1+\eta)$$

Figure 4.8 Discontinuous Interpolation Function for a 3-node Triangular Element

Chapter 5

Constitutive Relationships

5.1. Preliminary Considerations

It is of main concern to determine the laws that govern the local deformation response of the shear band. Fully developed plastic shear flow is considered and it can be regarded from the continuum stand-point as a plane simple shear flow if the scale of investigation is large compared with the characteristic length of the granular structure. Geometrically speaking, this kind of plastic shear flow can be visualized as the sliding of a set of infinitesimally close planes taking place inside a band of material. According to the scale of investigation, this simple shearing may not be continuous, and suffer discontinuity jumps across a shear plane. If the band is considered as a shear plane, the discontinuity will be rather described by a displacement jump. On the other hand for a relatively thick band, the same discontinuity may be regarded as a weak type, i.e. a jump in the gradient of displacement across the thickness of the band, see Figure 5.1.

From a macroscopic stand-point, the fully developed shear flow translates into paths along which grains over-ride each other over infinite distances; these paths undulate in a random manner about macroscopic shear planes. When considering a macroscopic shear plane element $s\,s$ in Figure 5.1, it is possible at any instant to associate it with a wavy surface element $s'\,s'$. In other words, the discontinuous shearing on a characteristic

sliding plane will be the limit which a continuous shear flow approaches when the width of the shear zone is made to vanish.

It is appropriate at this point to regard the shear flow phenomenon as a contact friction interaction problem. The oldest and most popular idealization for friction is due to Coulomb. Although originally postulated for contact between dissimilar rigid bodies, it may have an analogous interpretation for contact between deformable similar bodies. It can be stated that the relative motion between two adjacent points in contact will occur whenever the tangential stress attains a value equal in magnitude to the normal compressive stress multiplied by some constant called the friction coefficient which characterizes the interface. Furthermore, it requires the relative tangential motion to be zero prior to frictional slip. However in the case of geomaterials, considerable experimental evidence shows that reversible tangential displacements take place prior to any permanent frictional sliding. This appears specially in rock joints problems, see Rosso [1976].

5.2. Rupture interface rheology

The shear band is visualized as a zone of the soil body within which large structural changes, in the form of either grain crushing or re-orientation, take place during localized shearing. Furthermore, the surfaces demarcating the localized zone are considered planar and parallel to each other separated by a distance which is a function of the grain size of the material. As such the thickness of the band will generally be very small, and typically of the order of 10 to 20 times the mean diameter of the soil grains for granular materials.

5.2.1 Experimental observations

In order to investigate the constitutive behaviour of the shear band, an experiment has to be devised in which the band is allowed to form freely without any kinematic restraint so that one ensures measuring only the mechanical properties of the band just as if it were isolated. A very simple arrangement is the direct shear box apparatus, but there has been much

controversy upon its validity, and interpretation of test results. It is well known that the state of stress is far from being uniform inside the box due to stress concentrations at the edges. As a result, the shear strength is not uniformly mobilized inside the specimen so that the measured stresses can only be considered on an average sense. Figure 5.2 illustrates the initiation of rupture surfaces at the two opposite ends of the box due to progressive failure, and amazingly enough, they are not found to be horizontal in the direction of the physical plane of shearing. Kink bands are initially formed and have been observed by Morgenstern and Tchalenko [1967] who investigated the microscopic characteristics of shear banding in a Kaolin specimen subjected to direct shear. As the loading process progresses towards higher shearing, those microscopic features coalesce and make way to a shear band in the horizontal direction as a result of principal stress rotation, large deformation and improvement of kinematic constraints. In this situation the mobilized shear strength is fairly uniform along the shear band since at each material point, it may be considered that the residual strength has been reached. The relative sliding between the top box and the bottom one, then approximately represents the global behaviour of the shear band alone with surrounding material in a rigid passive stress state.

The transition from the two states described is made through a rapid drop of the shear strength from a peak value to a residual one, see Figure 5.3. The rate of drop in strength, or softening rate which one measures depends on many factors. Firstly, due to the non-uniform mobilization of shear stresses along the band, the stress-relative displacement curve will not be unique for any material point. Secondly, the rate of softening will be function of the grain size, thickness of the band and the size of the box as well.

In order to obtain a reasonable representation of the behaviour of the shear band in an experimental device, the end effects errors introduced must be eliminated. It would be convenient to have an infinitely long shear box: a close approximation of it being the ring shear apparatus, see Yoshimi and Kishida [1981]. In this device, the problems caused by

non-uniformity of stress distribution are reduced, but freedom of formation of the shear band is somewhat restricted. However, the stress-relative displacement behaviour in the post-peak range will be obtained within a higher degree of accuracy than can be reached by the direct shear box.

Both the direct shear box and the ring shear tests can be regarded as a surface element test, the dual form of a volume element test. At this scale of investigation, both stress and strain can be viewed as homogeneous along the idealized displacement discontinuity surface. Due to kinematic constraints, the macroscopic shear band does not change configuration and stays horizontal, i.e. the direction of imposed shearing. Several experiments, for example x-ray photographs taken in a large shear box confirm this observation, see Scarpelli and Wood [1982]. However, one has to be careful in dealing with the extent of non-homogeneity in the vicinity of the shear band. Although the stress and strain fields can be considered homogeneous along the shear band interface, they may not be so inside it.

5.3 Formulation of stress-relative displacement relationship

The deformational properties of the shear band are in general different from those of a material undergoing general 3-D deformation. This implies that although a constitutive model may be valid for general continuum behaviour, its validity may need analysis and investigation when specialized into shear band behaviour. For instance characterization of large structural changes and dilation inside a shear band may be different from those occurring in a body undergoing general deformation.

Figure 5.4 illustrates the generic shear band problem specialized into a two dimensional configuration. The simple situation involving a shear band parallel to the x-z plane with normal and shear stresses acting on the surface is considered. Also the stress and strain fields are assumed homogeneous in the x-y plane and no deformation is allowed

in the z direction. A relationship linking the loading vector, herein boundary stresses $\{\sigma_n, \tau\}$ defined on an average sense, to the response vector which contains the boundary relative normal and tangential slip displacements $\{g_n, g_t\}$ is sought. Mathematically, a functional depending on stresses, relative slip displacements and associated state variables such as density and void ratio must be formulated. A pragmatic approach is herein adopted whereby the functional ideally lumps all variables which may contribute to complex phenomena such as grain crushing, large displacements and distortions and rotations. Thus, ideally

$$\mathcal{F}(\sigma_n, \tau, g_n, g_t, \rho_0, n, \ldots) = 0. \tag{5.1}$$

The symbol '.....' refers to other variables that need to be accounted for, see Malvern[1969], based on the *Principle of Equipresence*, which requires that all variables that could possibly influence the response of the shear band be incorporated in $\mathcal{F}$. In precise terms, $\mathcal{F}$ represents a contact constitutive relationship. Due to the non-linear nature of the problem, an incremental formulation which relates tangential response to tangential load is preferably chosen. Also for simplicity of the formulation, a non-viscous behaviour is considered such that $\mathcal{F}$ is made a homogeneous function of order 1.

There are basically several approaches to determine $\mathcal{F}$, either by fitting experimental data using sophisticated mathematical techniques, or advocating the classical plasticity formalism. The coming sections will basically review and hence assess the two different approaches in view of applying them to the shear band problem.

5.3.1 Phenomenological approaches

In the phenomenological approach adopted by Ichikawa[1985] for modelling continuum constitutive behaviour, the loading vector is expressed by means of a response functional covering the spectrum of all possible field variables and loading paths. The concept can be

similarly applied to the shear band by postulating the stresses at the limiting boundaries to be solely function of slip displacements. As such, the response of the stress normal to the shear plane is made function of normal slip displacements, and to a lesser degree tangential slip displacements. On the other hand, tangential slip displacements will be the predominant factor governing the shear stress response. This can be mathematically written as:

$$\sigma_n = \Phi(g_n^p, g_t^p) \text{ and } \tau = \Psi(g_t^p, g_n^p), \tag{5.2}$$

in which Ψ and Φ are the response functions to be experimentally determined from fitting and spectrum techniques. Note that superscript 'p' in Eq. (5.2) stands for plastic or irrecoverable component of slip displacement. The incremental form of Eq. (5.2) obtained by simple differentiation thus leads to the stress-slip displacement relationship. However, the difficulty of the formulation lies in the proper determination of Ψ and Φ through experiments. This requires considerable data and mathematical fitting techniques such as spectrum analysis of functions in order to arrive at the final form of the functionals.

Alternatively, the processes characterizing the shear band can be conveniently cast into the framework of damage theory. Damage theory has been recently used in engineering mechanics and is a fairly well established, see Chaboche[1981]. In the same context, the shear force along the boundaries of a shear band of finite thickness can be made to originate from two contributing sources, namely one due to purely frictional effects and the other one due to the extent of damage, i.e grain crushing, particle reorientation and micro-cracking inside the band. This leads to partitioning the contact surface area into frictional and damage components. The frictional component is described by a classical Coulomb law while damage is given by a convenient evolution law. The determination of driving parameters requires very sophisticated experimental techniques. It is usually difficult to experimentally follow the evolution of damage, and hence the mathematical relationship. Consequently, a

damage based formulation will not be contemplated in the present analysis, and as a matter of fact, is not justified.

5.4 Plasticity formalism

In the present study the behaviour of the band can be completely described by means of the plasticity formalism. Both a yield surface and plastic potential are postulated. Softening effects and microfabric changes in the band can be macroscopically modelled by the expedient of making state variables such as mobilized band friction and cohesion degrade with accumulated plastic deformations.

Suppose the behaviour of the surface discontinuity formed by the band be governed by a conventional Coulomb contact law of the form

$$|\tau| = c_d(\gamma^p) - \sigma_n \tan \varphi_d(\gamma^p), \tag{5.3}$$

in which:

φ_d = characteristic friction angle of discontinuity,
c_d = characteristic cohesive strength of discontinuity, and
γ^p = plastic distortion taking place at the discontinuity.

5.4.1 Contact yield and plastic potential functions

The Coulomb yield function can thus be conveniently written in the following alternate form:

$$F_d = \tau^2 - \left[c_d(\gamma^p) - \sigma_n \tan \varphi_d(\gamma^p)\right]^2 = 0 \tag{5.4}$$

The flow rule of plasticity requires the incremental plastic strain vectors $\dot{\varepsilon}^p$ to be orthogonal to a plastic potential function. The plastic potential function can be formulated much in the

same fashion as in Eq. (5.4) by simply replacing the friction angle φ_d by a dilatancy angle ψ_d, and c_d by $\bar{c}_d$. Thus,

$$G_d = \tau^2 - \left[\bar{c}_d(\gamma^p) - \sigma_n \tan\psi_d(\gamma^p)\right]^2. \tag{5.5}$$

The incremental plastic strains are readily obtained from the flow rule

$$d\boldsymbol{\varepsilon}^p = d\lambda \frac{\partial G_d}{\partial \boldsymbol{\sigma}}, \tag{5.6}$$

with $d\boldsymbol{\varepsilon}^p = \left\{d\varepsilon_n^p, d\varepsilon_w^p\right\}$ and $\boldsymbol{\sigma} = \left\{\sigma_n, \tau\right\}$ in the band local system (n,t). It is noted that when the thickness of the shear band becomes small compared to the dimensions of the specimen, finite deformations within the shear band may develop and hence materially large deformation measures may be needed in Eq. (5.6).

It can be readily shown that defining the above flow rule leads to imposing a kinematic constraint to the normal slip displacement g_n^p and tangential slip displacement g_t^p, i.e.

$$\frac{dg_n^p}{dg_t^p} = s \tan\psi_d, \tag{5.7}$$

in which $s = -1$ if $\tau < 0$ and $s = 1$ if $\tau > 0$.

5.4.2 Evolution rule

The evolution of deformation inside the band—or at least in its neighbourhood—can be traced by making both friction angle φ_d and cohesion c_d become function of plastic distortion γ^p.

In plane strain conditions, the plastic distortion rate can be conveniently expressed by

$$\dot{\gamma}^p = \sqrt{2\dot{\mathbf{e}}:\dot{\mathbf{e}}}, \tag{5.8}$$

where the deviatoric strain rate $\dot{\mathbf{e}}$ is classically given as

$$\dot{\mathbf{e}} = \dot{\boldsymbol{\varepsilon}} - \frac{1}{2}\mathrm{trace}(\dot{\boldsymbol{\varepsilon}})\mathbf{1}, \tag{5.9}$$

where in the special case of the simple 2-D band,

$$\mathrm{trace}(\dot{\boldsymbol{\varepsilon}}) = \dot{\varepsilon}_{nn} + \dot{\varepsilon}_{tt} \text{ and } \mathbf{1}_{ij}\mathbf{1}_{ij} = 2 \text{ since } i,j = 1,2 \text{ } (\mathbf{1} \text{ is the Kronecker delta}). \tag{5.10}$$

By virtue of the above, and considering that the t axis is a direction of zero extension ($\dot{\varepsilon}_{tt} = 0$; pure shear), the plastic distortion simplifies into

$$\dot{\gamma}^p = \sqrt{(\dot{\varepsilon}_{nn})^2 + 2(\dot{\varepsilon}_{nt})^2}. \tag{5.11}$$

By making use of the shear band thickness d_b, the above in terms of slip displacement rates becomes

$$\dot{\gamma}^p = \frac{1}{d_b}\left[(\dot{g}_n^p)^2 + (\dot{g}_t^p)^2\right]^{1/2} = \frac{1}{d_b}\left\|\dot{\mathbf{g}}^p\right\|. \tag{5.12}$$

It is seen that the plastic distortion rate degenerates into the norm of the slip displacement vector for a point along the shearing plane.

5.4.3 Elasto-plastic contact constitutive tensor

In general, it can be considered that the deformation of the discontinuity (shear band) is only partially recoverable. As such,

$$\mathrm{d}\mathbf{g} = \mathrm{d}\mathbf{g}^{e} + \mathrm{d}\mathbf{g}^{p}. \tag{5.13}$$

The following elasticity relations hold:

$$\mathrm{d}\boldsymbol{\sigma} = \boldsymbol{\eta}^{e} : \mathrm{d}\mathbf{g}^{e}, \tag{5.14}$$

where

$$\eta^{e} = \begin{bmatrix} K_d & 0 \\ 0 & G_d \end{bmatrix} \tag{5.15}$$

The parameters K_d and G_d are respectively elastic normal and shear moduli for the discontinuity.

The plastic slip displacements can be explicitly given by use of the alternate form of Eq. (5.5) and Eq. (5.6), i.e.

$$\mathrm{d}g_n^p = d_b \, \mathrm{d}\lambda \tan\psi_d, \mathrm{d}g_t^p = d_b \, \mathrm{d}\lambda. \tag{5.16}$$

The consistency equation, i.e $\mathrm{d}F_d = 0$, ensures that the stress stays on the yield surface, in other words,

$$\frac{\partial F_d}{\partial \boldsymbol{\sigma}} : \mathrm{d}\boldsymbol{\sigma} + \frac{\partial F_d}{\partial \gamma^p} : \mathrm{d}\gamma^p = 0. \tag{5.17}$$

Replacing $\mathrm{d}\gamma^p$ in the above with the aid of Eqs. (5.11) and (5.16) leads to the expression of the plastic multiplier $\mathrm{d}\lambda$, i.e.

$$\mathrm{d}\lambda = \frac{1}{H_d} \frac{\partial F_d}{\partial \boldsymbol{\sigma}} : \mathrm{d}\boldsymbol{\sigma}, \tag{5.18}$$

in which the hardening modulus H_d is

$$H_d = -\frac{1}{\cos\psi_d} h_d; \quad h_d = \frac{\partial F_d}{\partial \gamma^p}. \tag{5.19}$$

It can be readily shown, that the enforcement of the above consistency leads to the classical rate-independent contact constitutive relation

$$\dot{\boldsymbol{\sigma}} \equiv \dot{\mathbf{t}} = \boldsymbol{\eta}^{ep} : \dot{\mathbf{g}}, \tag{5.20}$$

where $\boldsymbol{\eta}^{ep}$ is a second order tensor with the following expression

$$\boldsymbol{\eta}^{ep} = \frac{1}{d_b}\left[\boldsymbol{\eta}^{e} - \frac{\left(\boldsymbol{\eta}^{e} : \dfrac{\partial F_d}{\partial \boldsymbol{\sigma}}\right) \otimes \left(\dfrac{\partial G_d}{\partial \boldsymbol{\sigma}} : \boldsymbol{\eta}^{e}\right)}{H_d + \dfrac{\partial F_d}{\partial \boldsymbol{\sigma}} : \boldsymbol{\eta}^{e} : \dfrac{\partial G_d}{\partial \boldsymbol{\sigma}}}\right]. \tag{5.21}$$

$\otimes$ denotes the tensor product in the sense that $(\mathbf{a} \otimes \mathbf{b})_{ijkl} = (\mathbf{a})_{ij}(\mathbf{b})_{kl}$.

The final explicit form of the above equation, in the special case of the 2-D planar shear band is

$$\boldsymbol{\eta}^{ep} = \frac{1}{d_b}\left\{\begin{bmatrix} G_d & 0 \\ 0 & K_d \end{bmatrix} - \frac{1}{G_d + K_d \tan\varphi_d \tan\psi_d - h_d \sec^2\psi_d}\begin{bmatrix} G_d^2 & sG_dK_d \tan\psi_d \\ sG_dK_d \tan\psi_d & K_d^2 \tan\psi_d \tan\varphi_d \end{bmatrix}\right\} \tag{5.22}$$

In order to get some insight into the above expression, if h_d tends to infinity, the elastic constitutive tensor is recovered. For a purely cohesive shear band, it suffices to replace both friction and dilatancy angles by zero in the very general expression in Eq.(5.22).

The evaluation of the constitutive tensor $\boldsymbol{\eta}^{ep}$ depends explicitly on the shear band thickness d_b. In order to avoid the sensitivity to this dimension, which in fact cannot be

uniquely determined, the problem can be reformulated in terms of strain rates, i.e. the shear band is associated with a velocity discontinuity.

s'-s' microscopic shear plane

s - s macroscopic shear plane

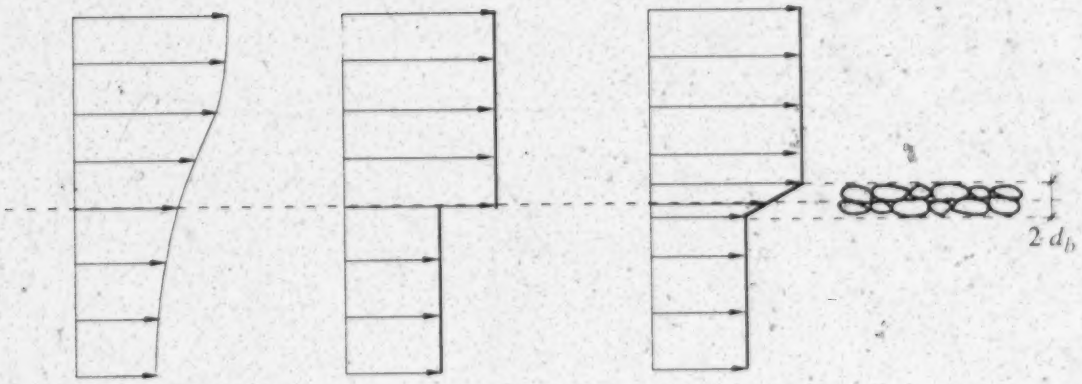

(a) continuous shearing

(b) "jump" discontinuity type of shearing

(c) "weak" discontinuity type of shearing

Figure 5.1 Macroscopic schematization of shear flow inside a shear band

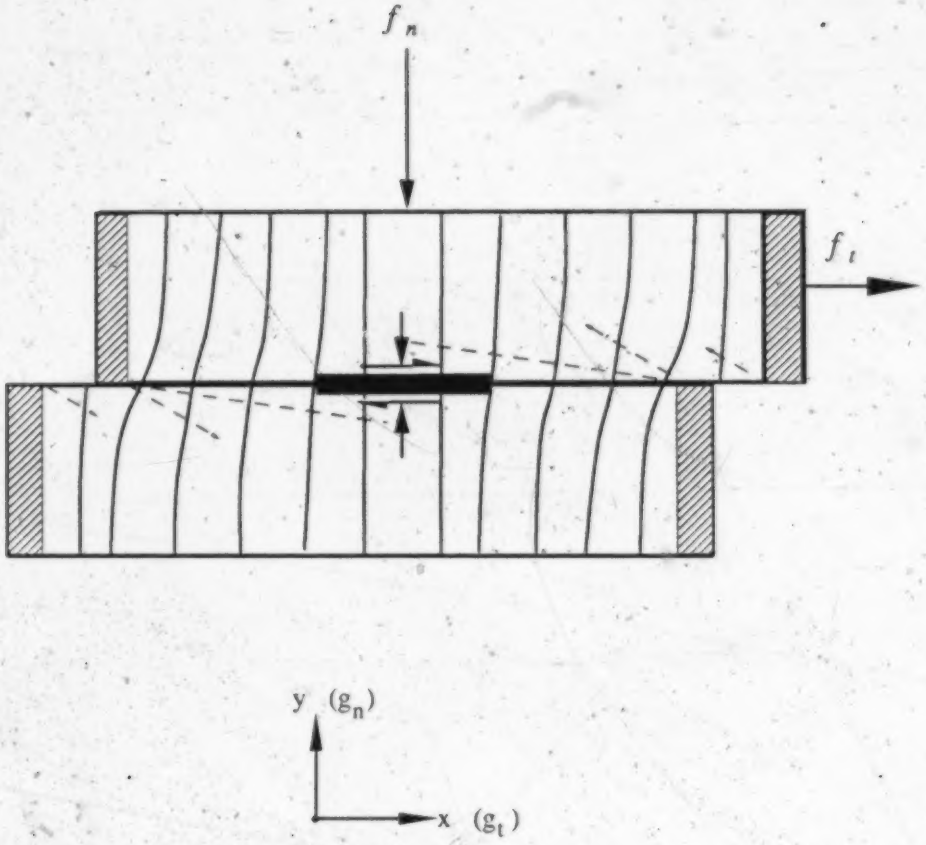

Figure 5.2 Non-uniform stress distribution inside a shear box: progressive failure

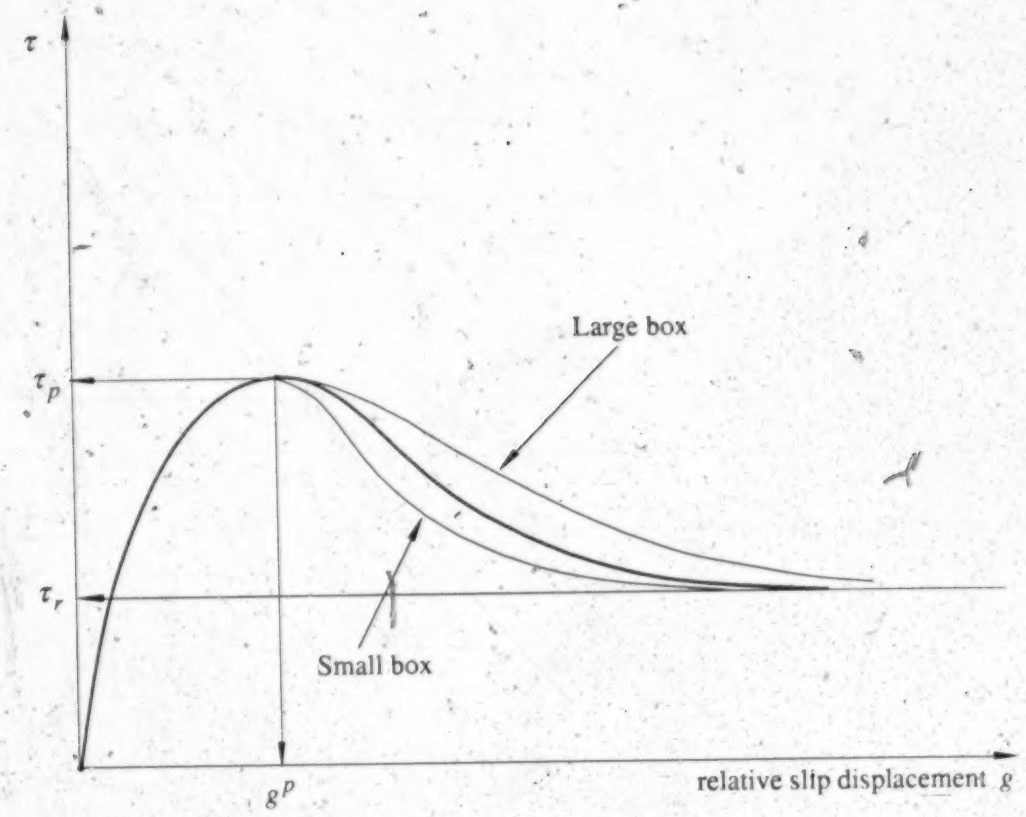

Figure 5.3 Stress-relative displacement relationship in a direct shear box

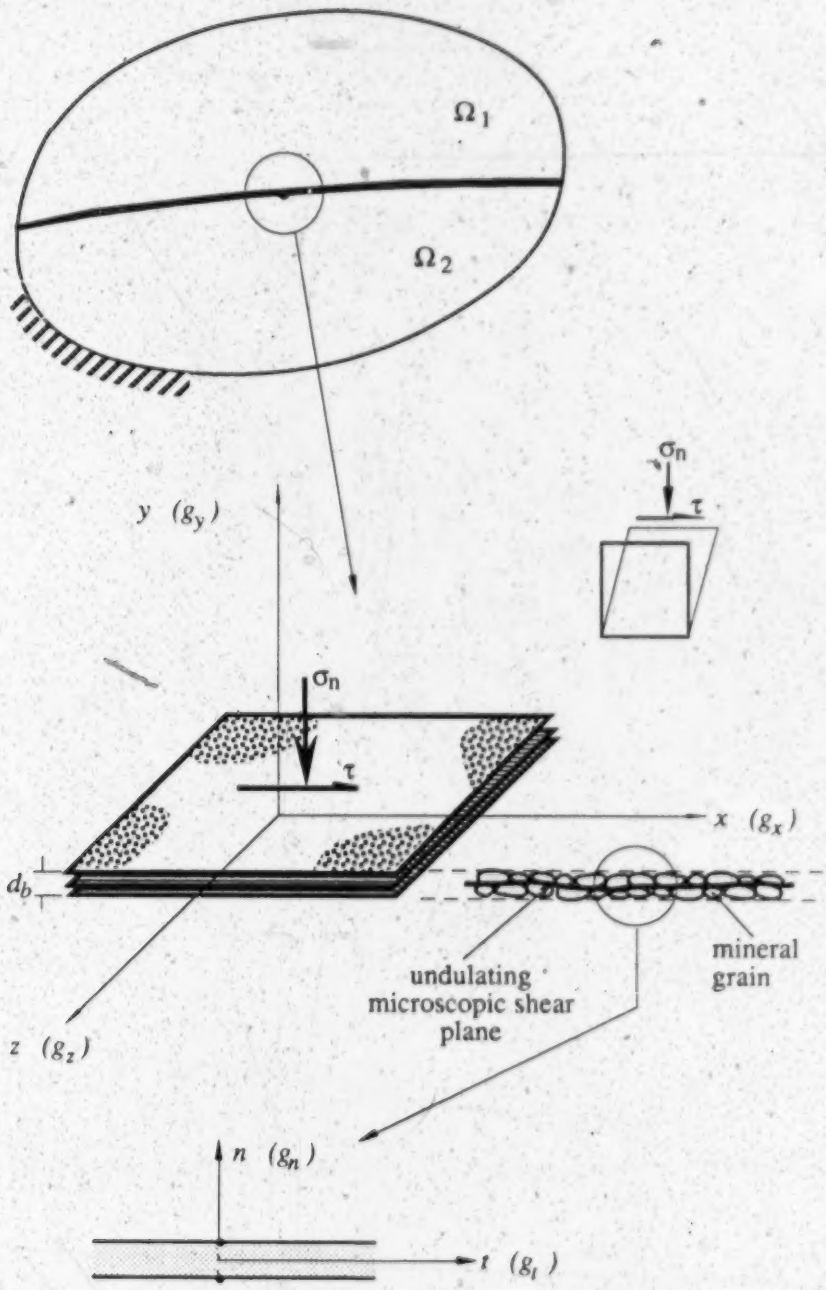

Figure 5.4 Generic representation of shear band in 2-D configuration

Chapter 6

Numerical Strategies

6.1. Introduction

The previous chapters laid the foundation for the establishment of a formalism for shear band inception, ensuing kinematics and basic laws governing its behaviour. In precise terms, it has been shown in Chapter 3, that bifurcation theory is appropriate for predicting localization. Chapter 4 goes on and demonstrates that important features, such as the discontinuous behaviour which arises during localization, can be incorporated into the theory by modifying the Principle of virtual work into an equivalent one for a body traversed by a discontinuity surface representing a shear band.

The pursuit of a finite element oriented framework has led to the design of special finite elements with embedded discontinuities in their interpolation functions to adequately model the real kinematics. Also, in Chapter 5, various contact laws have been reviewed and subsequently adapted to describe the shear band constitutive behaviour.

In this chapter, the implementation of foregoing formulations into a finite element program is discussed together with strategies adopted for the solution of numerical difficulties which inevitably arise in such a complex model.

6.2. Issues on model implementation

The discrete nature of the approach adopted for the modelling of shear bands inevitably introduces problems associated with the proper determination of the geometrical location and inclination of a shear band within a typical element. In a smeared scheme, the band topology is not indeed a real issue—the sole concern is in fact to diffuse the deformations generated inside the band over the entire representative domain, i.e. the element, in order to reproduce an idealized pseudo-uniform mode.

In contrast, the methodology herein followed examines the shear banded element at a discrete level—in more precise terms the kinematics are the primary features which govern the behaviour of the structure. Therefore in the post localized regime, the behavioural response of the element is modelled by introducing pseudo degrees of freedoms meant to enhance its deformational capabilities. As such, the location of the shear band inside the element must be determined as accurately as possible since any deviation from *reality* may cause drastic changes in the predictive behaviour of the element. This is why a scheme has to be found, based on stress values or state variables within the element. Thus in order to arrive at a sensible method, a proper understanding of shear band inception and physical meaning are needed.

The localization of deformation into a shear band is closely connected with the loss of ellipticity (bifurcation) of the governing equilibrium equation. The characteristic equations (surfaces) then indicate the location and shape of the localized zones, but leave the size undetermined. It bears emphasis to say that in this method, localization conditions are considered local, i.e. they can be ascertained into an elementary or point-wise fashion. Turning back to the finite element discretization by a displacement type of formulation, it can be seen that difficulties arise as to the accuracy of locating the band. As well established now, in a displacement type formulation, a displacement field which satisfies inter-element

compatibility is searched so that it makes the potential energy functional achieve a stationary value. As a result, equilibrium conditions will only be satisfied in an average sense, i.e. the computed stress field will be approximate.

Since the loss of ellipticity can be assessed in a discrete manner, i.e. at Gauss sampling points, the inclination predicted will not be representative of the actual ones because they have been determined from stress values which satisfy governing equations of equilibrium only on an average sense. This is the drawback which is usually inherited from a displacement type of formulation. Even if the shear band were to be found accurately, the continuity of stresses at the interface would not be fully satisfied—the analysis may be thereby questionable. However, these problems can be erased by adopting a stress or hybrid type of formulation. For a preliminary study, it is thought that the displacement based formulation can still give fairly accurate results. The hybrid formulation would require much more computational effort both from the analytical and computational standpoints.

It is logical to think about trying to determine the locus of points which will satisfy the bifurcation condition inside the element. The question is whether the shear band directions found for each point on the locus surface really coincide with the tangent to the same point. It is thought that they do not need to coincide since the locus surface can be crossed by an infinite number of shear bands. A reasonable scheme to locate the shear band would most probably involve finding an equivalent or mean value of all shear band inclinations computable along the locus surface. Once this has been found the locus has to be adjusted along the mean shear band inclination. However, the condition of bifurcation along the shear band might not be satisfied any more. This inevitably requires an iterative process similar to the location of a free surface in unconfined flow problems.

6.3. Computational aspects of localization

In the solution of a generalized elasto-plastic boundary value problem, the whole domain is viewed as being elastic at the very beginning of the deformation process. Moreover, as applied external loads are gradually increased, the state of stress at any generic point becomes progressively severe so as to cause a local instability (bifurcation) of the constitutive law which coincides with localization. This condition was mathematically derived in Chapter 3 and is recalled for clarity of exposition:

$$\det(n_i L_{ijkl} n_l) = 0, \tag{6.1}$$

in which the indices i, j, k, l range from 1 to 3 (summation implied upon repeated indices) for 3-D stress conditions, **n** is the unit normal vector to an incipient shear band, and L_{ijkl} is the fourth order tensor of the tangential constitutive operator.

Without losing too much generality, only 2-D stress configurations will be addressed in this thesis. Equations (3.4) and (3.11) gave respectively the relation between the tensor components of stress and strain, and the explicit form of the elasto-plastic tangential constitutive tensor which would have to be replaced in Eq. (6.1). For finite element analysis purposes, it is more convenient to express the relationship in matrix form, i.e., in 2-D situations:

$$\{\dot{\sigma}\} = [L]\ \{\dot{\varepsilon}\}, \tag{6.2}$$

where

$$\{\dot{\sigma}\} = \{\dot{\sigma}_{11}\ ,\ \dot{\sigma}_{22}, \dot{\sigma}_{12}\}, \tag{6.3a}$$

$$\{\dot{\varepsilon}\} = \{\dot{\varepsilon}_{11}\ ,\ \dot{\varepsilon}_{22}, \dot{\varepsilon}_{12}\}. \tag{6.3b}$$

Because of symmetry of the stress and strain tensors, interchanging i and j or k and l in Eq. (6.1) results in the same quantity, thus the matrix $[L]$ is related to tensor L_{ijkl} as follows:

$$[L] = \begin{bmatrix} L_{1111} & L_{1122} & L_{1112} \\ L_{2211} & L_{2222} & L_{2212} \\ L_{1211} & L_{1222} & L_{1212} \end{bmatrix} \tag{6.4}$$

While the solution of the bifurcation criterion given in Eq. (6.1) has to be checked during the numerical integration of the constitutive equation represented by (6.2), onset of localization will occur at the first point in the deformation history for which non trivial solutions of the determinant exist. Calling the tensor inside the determinant an *acoustic* tensor A_{jk} whose expression after partial expansion is

$$A_{jk} = n_1^2 L_{1jk1} + n_1 n_2 (L_{1jk2} + L_{2jk1}) + n_2^2 L_{2jk2}, \tag{6.5}$$

Eq. (6.1) reduces to

$$\begin{vmatrix} A_{11} & A_{12} \\ A_{21} & A_{22} \end{vmatrix} = 0, \tag{6.6}$$

in which

$$A_{11} = n_1^2 L_{1111} + n_1 n_2 (L_{1112} + L_{2111}) + n_2^2 L_{2112}, \tag{6.7a}$$

$$A_{22} = n_1^2 L_{1212} + n_1 n_2 (L_{1222} + L_{2212}) + n_2^2 L_{2222}, \tag{6.7b}$$

$$A_{12} = n_1^2 L_{1112} + n_1 n_2 (L_{1122} + L_{1212}) + n_2^2 L_{1222}, \tag{6.7c}$$

$$A_{21} = n_1^2 L_{1211} + n_1 n_2 (L_{1221} + L_{2211}) + n_2^2 L_{2212}. \tag{6.7d}$$

Expanding the determinant finally gives rise to a complete fourth order polynomial,

$$f(\theta) = b_0 + b_1 \tan\theta + b_2 \tan^2\theta + b_3 \tan^3\theta + b_4 \tan^4\theta = 0, \qquad (6.8)$$

where

$$\begin{aligned}
b_0 &= (L_{1111} L_{1212} - L_{1112} L_{1211}) \\
b_1 &= (L_{1111} L_{1222} + L_{1111} L_{2212} - L_{1112} L_{2211} - L_{1211} L_{1122}) \\
b_2 &= (L_{1111} L_{2222} + L_{1112} L_{1222} + L_{1211} L_{2212} - L_{1122} L_{1212} - L_{1122} L_{2211} - L_{1212} L_{2211}) \\
b_3 &= (L_{1112} L_{2222} + L_{1211} L_{2222} - L_{1222} L_{2211} - L_{2212} L_{1122}) \\
b_4 &= (L_{1212} L_{2222} - L_{1222} L_{2212}) \qquad (6.9)
\end{aligned}$$

and $\tan\theta = n_2/n_1$.

Once the shear band directions are determined, the *acoustic* tensor **A** is totally defined and its zero eigenvectors are found. If **a** is an eigenvector whose components are a_1 and a_2 in the Cartesian axes (x_1, x_2) then

$$\begin{bmatrix} A_{11} & A_{12} \\ A_{21} & A_{22} \end{bmatrix} \begin{Bmatrix} a_1 \\ a_2 \end{Bmatrix} = \begin{Bmatrix} 0 \\ 0 \end{Bmatrix}, \qquad (6.10)$$

and hence the bifurcation direction ω is given by

$$\frac{a_2}{a_1} = \tan\omega = \frac{-[L_{1111} + (L_{1112} + L_{1211})\tan\theta + L_{1212}\tan^2\theta]}{[L_{1112} + (L_{1122} + L_{1212})\tan\theta + L_{1222}\tan^2\theta]} \qquad (6.11)$$

The geometrical representation of the shear band direction with respect to the global reference axes (x,y), together with the corresponding bifurcation direction are given in Fig. 6.1.

6.3.1 Determination of a bifurcation point

Ideally in a finite element analysis, real roots of Eq. (6.8) must be sought to confirm localization conditions. In other words, the bifurcation point must be pin-pointed sometime during the evolution of the loading history. Solving for roots of the polynomial in Eq. (6.8) is tantamount to searching for the normals of the prospective fronts upon which the displacement field may be discontinuous.

Since the bifurcation criterion will have to be checked in a point wise fashion during the course of deformation at Gauss points where stress and strain are most accurately determined, an efficient numerical procedure has to be found. It is proposed to analytically solve the roots of $f(\theta)$ rather than resort to a standard numerical scheme which involves iterations.

Solving Eq. (6.8) is similar to finding the intersection of the quartic function with the θ axis, see Fig. 6.2. If all possible roots of $f(\theta)$ are complex, i.e minima of the quartic are positive, this implies that the solution regime is elliptic. Possible real solutions will only be obtained whenever one of the minima becomes zero or negative, i.e. tangent and past the θ axis respectively. As such, the possible solutions regimes will be obtained according to the stress dependent coefficients b_i given in Eq. (6.9) as the curve $f(\theta)$ moves continuously towards the θ axis. This can be extended to a 3-D situation in which a surface is instead obtained and its minima corresponding to points of tangency of the surface to a horizontal plane passing through the origin are sought.

Keeping the above observation in mind, one has the following algorithm for a 2-D situation, summarized in Table 6.1, which derives from Galois theory (see for example Hungerford [1974]).

Table 6 1. Solution Algorithm for Quartic Equation

Solve for the real roots of:

$$b_0 + b_1 \tan\theta + b_2 \tan^2\theta + b_3 \tan^3\theta + b_4 \tan^4\theta = 0$$

if $b_4 = 0$, then solve the corresponding cubic equation

else let $\lambda = \tan\theta$, $a = b_3/b_4$, $b = b_2/b_4$, $c = b_1/b_4$, $d = b_0/b_4$

solve

$$\lambda^4 + a\lambda^3 + b\lambda^2 + c\lambda + d = 0.$$

1. Form resolvant cubic:

$$\lambda^3 - b\lambda^2 + (ac - 4d)\lambda + (-a^2d + 4bd - c^2) = 0.$$

2. Let

$$p = (b/3)^2 - (ac - 4d)/3,$$
$$q = (b/3)^3 - b(ac - 4d)/6 + (a^2d - 4bd + c^2)/2.$$

3. If $q^2 - p^3 \geq 0$ (resolvant cubic has only one real root) then let

$$y = \sqrt[3]{q + \sqrt{q^2 - p^3}} + \sqrt[3]{q - \sqrt{q^2 - p^3}} + b/3$$

Else let

$$y = 2\sqrt{p}\cos\left(\tfrac{1}{3}\arccos\left(\frac{q}{p\sqrt{p}}\right)\right) + b/3.$$

4. Solution of two quadratics:
Let

$$Q = \sqrt{\frac{a^2}{4} - b + y}, \quad S = \frac{3a^2}{4} - 2b - Q^2.$$

5. If $Q \neq 0$ then let

$$T = \frac{4ab - 8c - a^2}{4Q}$$

Else let

$$T = 2\sqrt{y^2 - 4d}$$

6. If $T + S \geq 0$ then let the first two roots be

$$\lambda = -\frac{a}{4} + \frac{Q}{2} \pm \frac{\sqrt{S+T}}{2}$$

else if $S - T \geq 0$ then let the two other roots be

$$\lambda = -\frac{a}{4} - \frac{Q}{2} \pm \frac{\sqrt{S-T}}{2}$$

❑

6.3.2 Test problems

The algorithm used to locate shear band inception and its orientation in space is illustrated by examining a single quadratic 4 node element.

Figure 6.3 illustrates one single element whose configuration is such that three nodes are restrained to move in both x and y directions, while the fourth node is subjected to prescribed displacements. The loading condition is of particular interest because the prescribed displacements are consistent with a non uniform field very much prone to localization conditions. In contrast to loading conditions consistent with a constant strain field where all Gauss points bifurcate at the same time, the present configuration allows for non-simultaneous bifurcation of Gauss points due to a non-homogeneous field.

The material is assumed to obey simple J_2 flow plasticity behaviour with a hardening/softening stress-strain law. The material properties used and the explicit expression of the consistent tangent operator are summarized in Table 6.2. It is noted that a negative hardening modulus is used in the analysis to guarantee localization; a feature which has been discussed in Chapter 3.

As displacements are prescribed, the material progressively deforms until plastic yielding first occurs at Gauss point 1. Gauss point 4 subsequently follows while the other Gauss points 2 and 3 are essentially still elastic.

During the stress integration, the tangential operator for the stress-strain law is subjected to bifurcation analysis and the scheme described in the previous section is applied. A bifurcation analysis at an elemental level predicts inception of a shear band at Gauss point 1 with two distinct inclinations. It is understood there, that the two shear band configurations are kinematically possible since the bulk material is deformable and not rigid. Fig. 6.4 shows the force displacement curve for node 4 in the homogeneous situation with the corresponding bifurcation point. The evolution of the determinant of the acoustic tensor during the search of a prospective shear band is depicted in Fig. 6.5, while shear strains at the Gauss points for the homogeneous situation are plotted in Fig. 6.6.

At first, the governing field equations are elliptic in nature and this results into a positive determinant. As the loading conditions become more severe, the equations change regime from elliptic to parabolic. Two possible shear band inclinations are obtained. The analysis necessitates both inclinations to be equally possible since they would both satisfy conditions of statics and kinematics. However, the shear band inclination which dissipates the most energy, and which is fully compatible with loading and boundary conditions will prevail.

6.4 Numerical algorithm

The proposed model requires a special finite element algorithm for the solution of the localized problem. The non-linear problem is solved by applying the load incrementally. Within each load increment, several conditions are checked namely: plasticity, bifurcation and evolution of the shear band. The analysis goes through several iterations until all pertinent criteria—satisfaction of yield and slip conditions for the ambient material and the shear band respectively—are satisfied, and an equilibrium state is reached.

The different steps in the algorithm used are summarized in Table 6.3. For a typical pseudo-time interval of interest $[t_n, t_{n+1}]$, suppose that displacements $\mathbf{u}_n$, slip displacements $\mathbf{g}_n$, stresses $\boldsymbol{\sigma}_n$ and internal tractions $\mathbf{t}_n$ are perfectly known for the beginning of the step t_n. As an initial guess (iteration number i=1), all field variables are set to previous values as shown in step 2. The load vectors for both the continuous and discontinuous components are then computed. These are next compared with the internal work equivalent forces in order to check for global equilibrium of the system as given in step 5. Since there are two force equilibria to be satisfied, i.e one regarding the continuous displacements, and the other the slip displacements, each criterion has to be treated one at a time until the two conditions are approximately achieved.

The composite stiffness matrix is either updated or expanded (case there is a new band formed) in step 6 in order to evaluate the trial displacements in step 7. The strains are next computed using the standard procedure, except that now there is a contribution from the discontinuous displacement components. The traction forces along the shear band are checked against the Coulomb slip criterion. If slip occurs, the tangential traction forces are limited to the values tolerated by the frictional and cohesive characteristics of the interface. If the traction forces are tensile, then the opening of the interface at the shear band is kept to a limiting value. The analysis continues by incrementing the displacements as well as the slip displacements, and equilibrium is checked once again by going to step 4.

In the event that slip conditions are fulfilled along the shear band, together with equilibrium, bulk convergence is next verified. If yielding of the bulk material occurs, the analysis goes into a classical plasticity algorithm, and residual forces are evaluated iteratively until an equilibrium state is reached.

The next step is to check bifurcation conditions locally for each element. If any new Gauss point bifurcates, this will be taken into account in the next load increment when the stiffness matrix is calculated in step 6. Since there has been a change in configuration, pertinent information at Gauss points such as stresses, strains, plastic strains and other state variables are reset, and appropriate values for new Gauss points required by the new shear band element are found by extrapolation from original Gauss points.

Details on implemention with regards to calculation of the constituent stiffness matrices, load terms and shape functions are given in Appendix B to assist the reader.

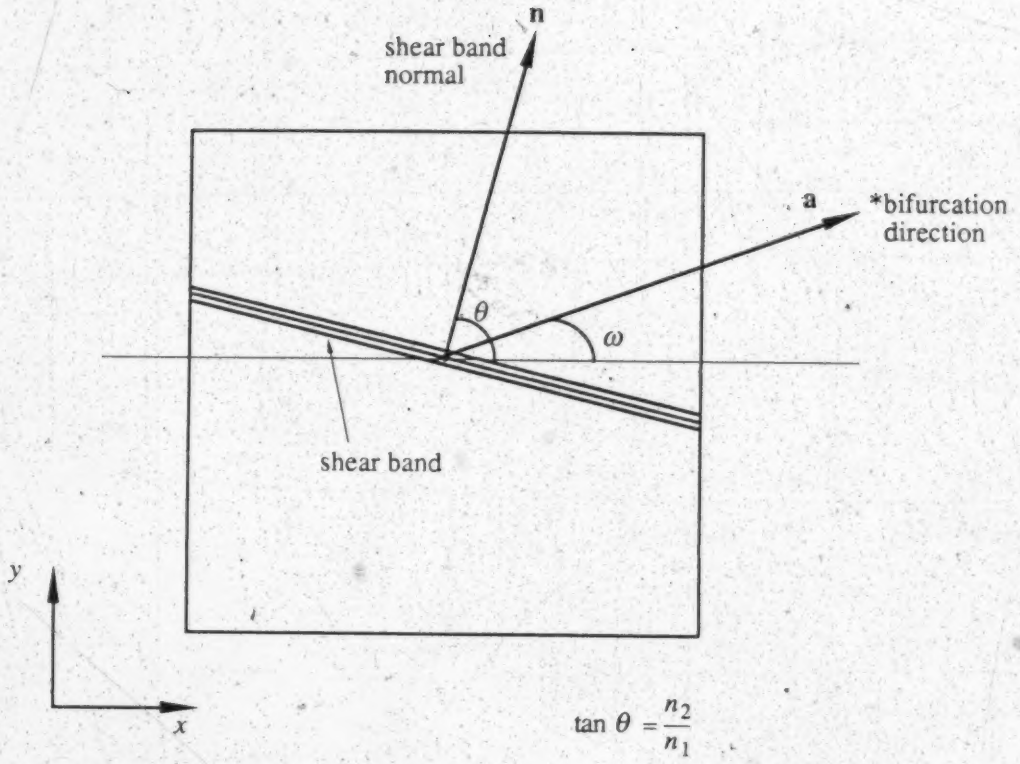

*bifurcation direction indicates the direction of relative displacement of points on the shear band.

Figure 6.1 Geometrical representation of shear band in 2-D situation

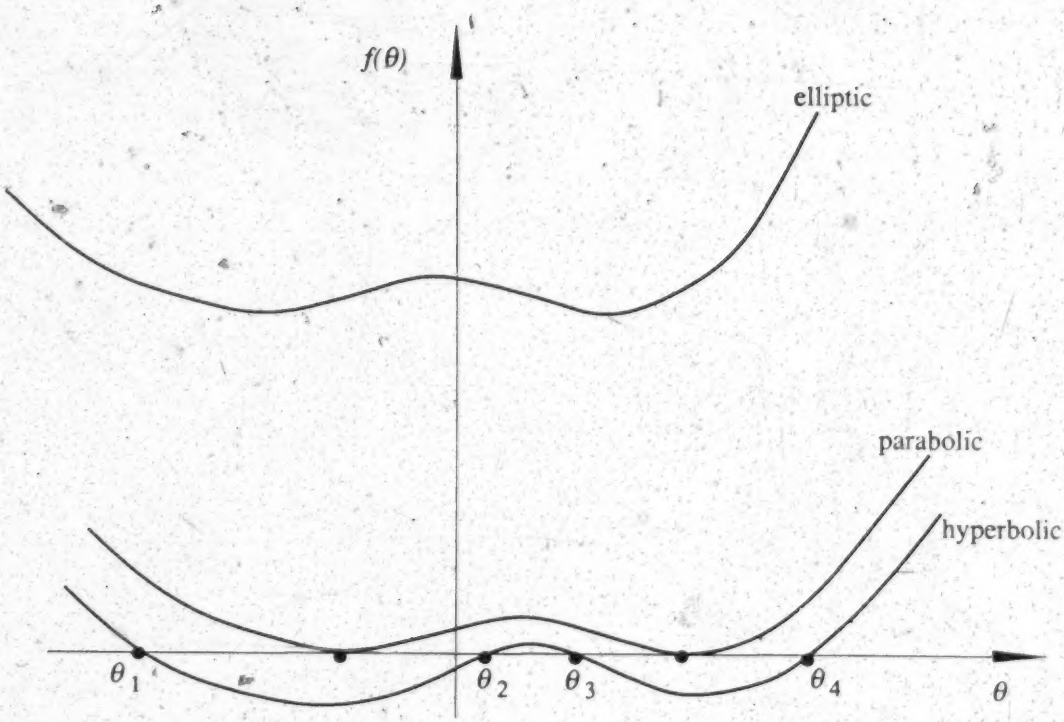

Figure 6.2 Schematic represention of finding shear band inclinations from bifurcation criterion

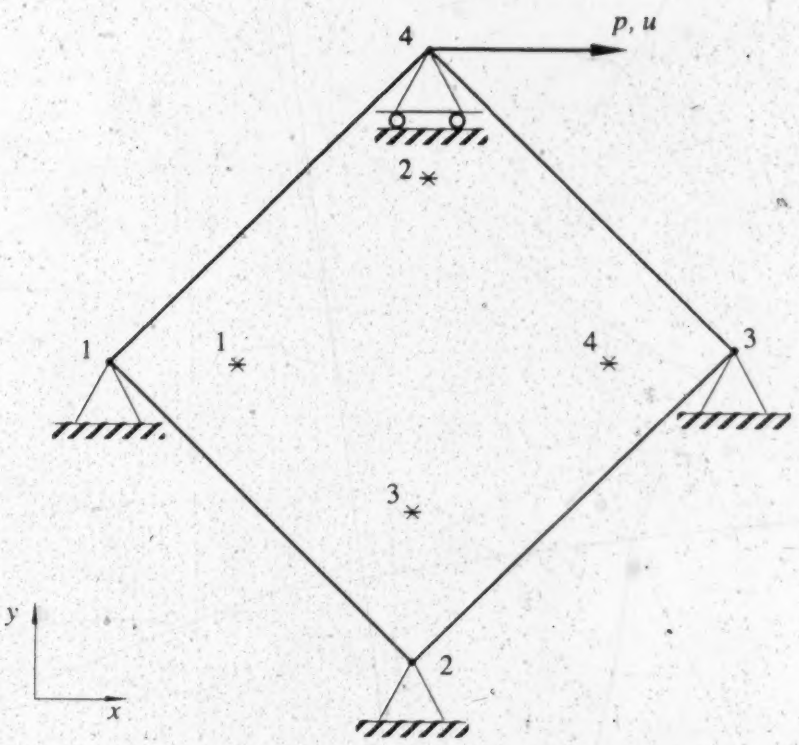

Figure 6.3 Non-uniform shear loading: One element test problem

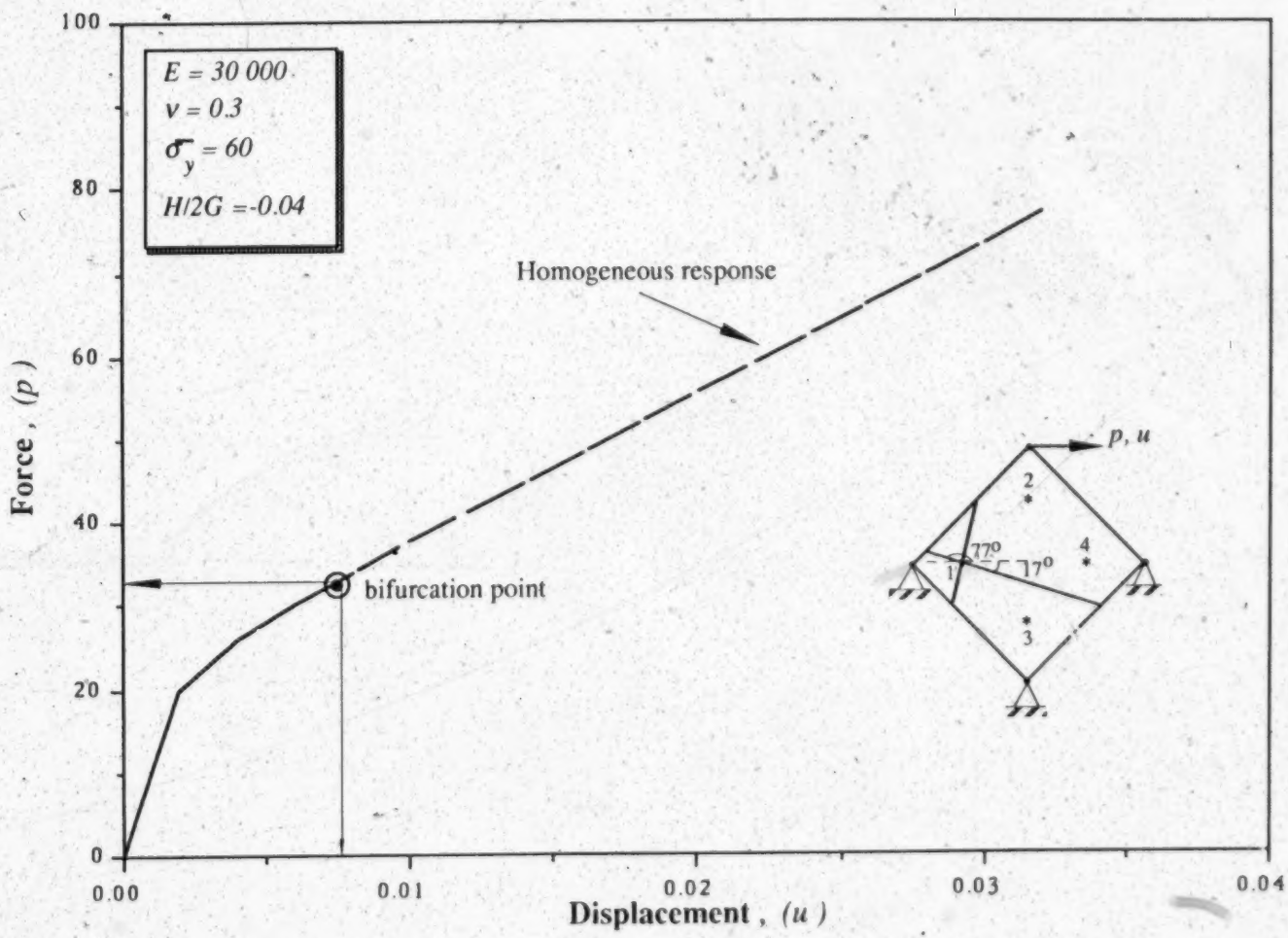

Figure 6.4 Force-Displacement curve for non-uniform shear loading

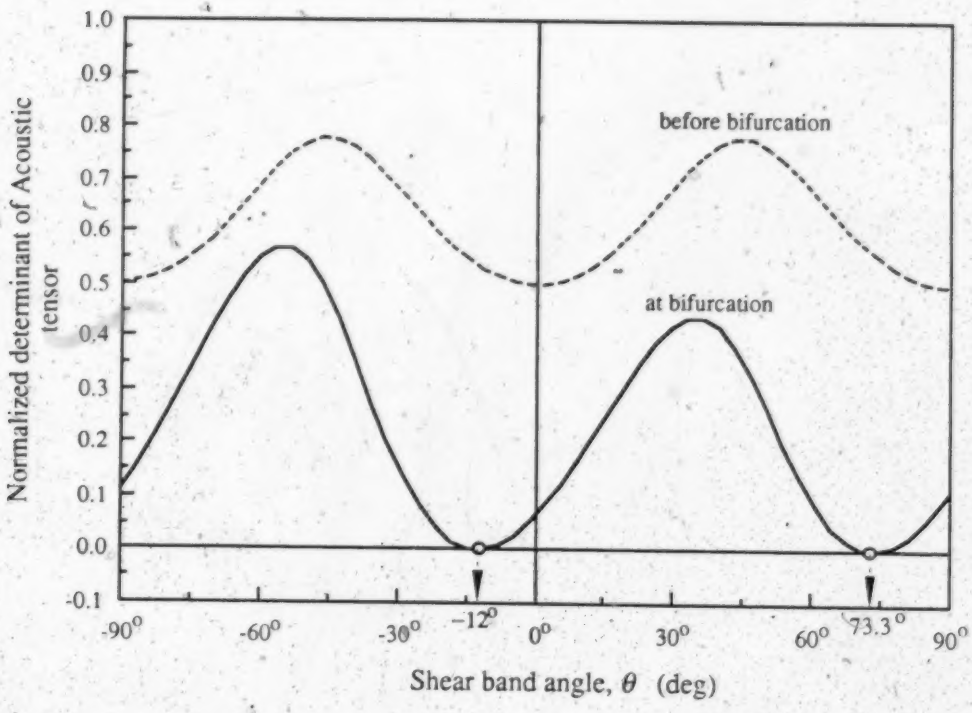

Figure 6.5 Evolution of the determinant of acoustic tensor with loading history

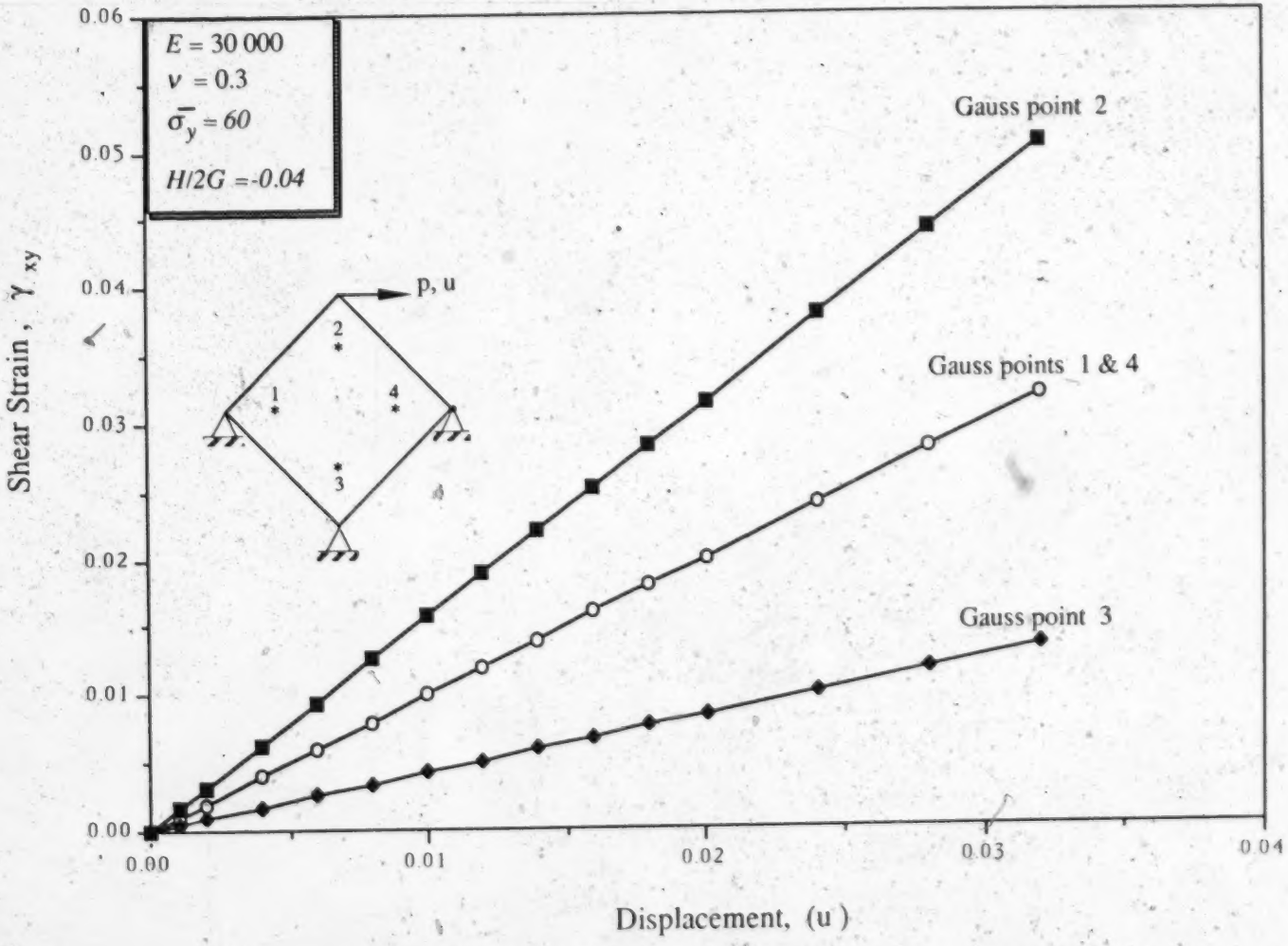

Figure 6.6 Evolution of shear strains at Gauss points for homogeneous analysis

Table 6.2 J_2 flow plasticity

Yield Function:

$$F = \sqrt{3J_2} - \kappa(\bar{\varepsilon}^p) = 0.$$

Hardening Rule:

$$\kappa(\bar{\varepsilon}^p) = \bar{\sigma}_y + H\bar{\varepsilon}^p.$$

Effective Plastic Strain Rate:

$$\dot{\bar{\varepsilon}}^p = \int_0^t \sqrt{\tfrac{2}{3}}\left[\dot{\mathbf{e}}^p : \dot{\mathbf{e}}^p\right]^{1/2} d\tau, \quad \dot{\mathbf{e}}^p = \dot{\boldsymbol{\varepsilon}}^p - \frac{1}{3}\text{trace}(\dot{\boldsymbol{\varepsilon}}^p)\mathbf{1}.$$

$J_2 = \sqrt{3}[\mathbf{s}:\mathbf{s}]^{1/2}$, $\mathbf{s} = \boldsymbol{\sigma} - \frac{1}{3}\text{trace}(\boldsymbol{\sigma})\mathbf{1}$ and $\mathbf{1}$ = Kronecker delta.

Incremental Stress - Strain Relationship:

$$\dot{\boldsymbol{\sigma}} = \mathbf{L} : \dot{\boldsymbol{\varepsilon}};$$

For a load step between times t_n and t_{n+1}, at iteration k, the consistent modulus becomes:

$$\mathbf{L}^k_{n+1} = K\,\mathbf{1}\otimes\mathbf{1} + 2G\beta(\mathbf{I} - \tfrac{1}{3}\mathbf{1}\otimes\mathbf{1}) - 2G\bar{\lambda}_{n+1}\hat{\mathbf{n}}\otimes\hat{\mathbf{n}}$$

where

$\mathbf{I}_{ijkl} = \frac{1}{2}(\mathbf{1}_{il}\mathbf{1}_{kj} + \mathbf{1}_{ik}\mathbf{1}_{jl})$, $\hat{\mathbf{n}} = \frac{\mathbf{s}^{tr}_{n+1}}{\|\mathbf{s}^{tr}_{n+1}\|}$, $\mathbf{s}^{tr}_{n+1}$ the trial deviatoric stress,

and $\beta = \sqrt{\frac{2}{3}}\frac{(\bar{\sigma}_y + H\bar{\varepsilon}^p_{n+1})}{\|\mathbf{s}^{tr}_{n+1}\|}$, $\bar{\lambda}_{n+1} = \frac{1}{1 + H/3G} - (1-\beta)$.

$\|\,.\,\|$ denotes a tensor norm and $\otimes$ the tensor product in the sense that $(\mathbf{a}\otimes\mathbf{b})_{ijkl} = (\mathbf{a})_{ij}(\mathbf{b})_{kl}$.

$E = 3.0\ 10^4$ units, $\nu = 0.3$, $\bar{\sigma}_y = 60.0$ and $H/2G = -0.04$

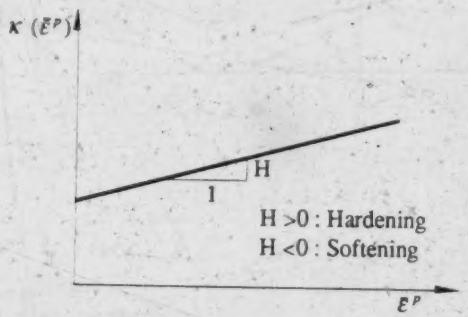

Table 6.3 Flow chart for localization problem algorithm

1. For increment $n+1$, set iteration number $i=1$

2. As initial guess, set : $\mathbf{u}^i_{n+1} = \mathbf{u}_n$, $\mathbf{g}^i_{n+1} = \mathbf{g}_n$, $\boldsymbol{\sigma}^i_{n+1} = \boldsymbol{\sigma}_n$, $\mathbf{t}^i_{n+1} = \mathbf{t}_n$.

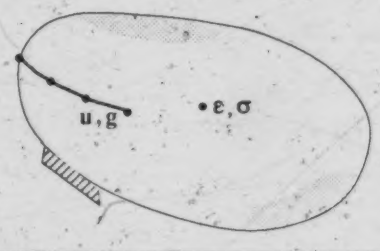

3. Set load level $(\mathbf{f}_\Omega)_{n+1} = \lambda^i_{n+1}\mathbf{f}_\Omega$, $(\mathbf{f}_s)_{n+1} = \lambda^i_{n+1}\mathbf{f}_s$, with $\lambda^i_{n+1} = 1$.

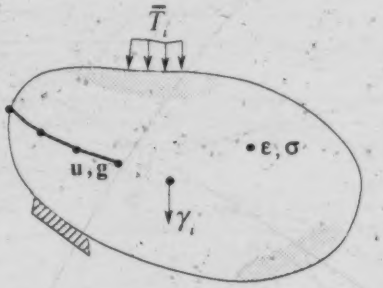

$$\mathbf{f}_\Omega = \int_\Omega \mathbf{N}^{(\alpha)} \cdot \boldsymbol{\gamma}\, d\Omega + \int_\Gamma \mathbf{N}^{(\alpha)} \cdot \bar{\mathbf{T}}\, d\Gamma,$$

$$\mathbf{f}_s = \int_\Omega \mathbf{N}^{(\beta)} \cdot \boldsymbol{\gamma}\, d\Omega + \int_\Gamma \mathbf{N}^{(\beta)} \cdot \bar{\mathbf{T}}\, d\Gamma.$$

4. Evaluate residual forces:

$$\boldsymbol{\psi}_\Omega(\mathbf{u}^i_{n+1}) = (\mathbf{f}_\Omega)_{n+1} - \int_\Omega \mathbf{B}^{(\alpha)^T} : \boldsymbol{\sigma}^i_{n+1}\, d\Omega,$$

$$\boldsymbol{\psi}_s(\mathbf{g}^i_{n+1}) = (\mathbf{f}_s)_{n+1} - \int_\Omega \mathbf{B}^{(\beta)^T} : \boldsymbol{\sigma}^i_{n+1}\, d\Omega - \int_{\Gamma_{sb}} \mathbf{N}^{(\beta)^T} \cdot \mathbf{t}^i_{n+1}\, d\Gamma.$$

5. Perform convergence check on norm of residual forces:

$$\left\| \begin{matrix} \boldsymbol{\psi}_\Omega \\ \boldsymbol{\psi}_s \end{matrix} \right\| \leq \varepsilon_L \left\| \begin{matrix} (\mathbf{f}_\Omega)_{n+1} \\ (\mathbf{f}_s)_{n+1} \end{matrix} \right\|.$$

...continued

Has solution converged?

NO

6. Set up stiffness matrix or update as required:

$$\begin{bmatrix} \mathbf{K}_{\Omega\Omega} & \mathbf{K}_{\Omega S} \\ \mathbf{K}_{S\Omega} & \mathbf{K}_{SS} \end{bmatrix}_{n+1}^{i}$$

7. Evaluate iterative displacements:

$$\begin{bmatrix} \mathbf{K}_{\Omega\Omega} & \mathbf{K}_{\Omega S} \\ \mathbf{K}_{S\Omega} & \mathbf{K}_{SS} \end{bmatrix}_{n+1}^{i} \begin{Bmatrix} \delta\mathbf{u}_{n+1}^{i+1} \\ \delta\mathbf{g}_{n+1}^{i+1} \end{Bmatrix} = \begin{Bmatrix} \boldsymbol{\psi}_{\Omega}(\mathbf{u}_{n+1}^{i}) \\ \boldsymbol{\psi}_{s}(\mathbf{g}_{n+1}^{i}) \end{Bmatrix}.$$

8. Evaluate iterative strains:

$\delta\boldsymbol{\varepsilon}_{n+1}^{i+1} = \mathbf{B}^{(\alpha)}.\delta\mathbf{u}_{n+1}^{i+1} + \mathbf{B}^{(\beta)}.\delta\mathbf{g}_{n+1}^{i+1}$,

$\delta\mathbf{g}_{n+1}^{i+1}$ = strains in shear band, i.e. slip displacements per unit thickness.

9. If relevant, check stress state on shear band:

$$\delta\mathbf{t}_{n+1}^{i+1} = \boldsymbol{\eta}^{e}.\delta\mathbf{g}_{n+1}^{i+1},$$

$$\mathbf{t}_{n+1}^{i+1} = \mathbf{t}_{n+1}^{i} + \delta\mathbf{t}_{n+1}^{i+1}.$$

Check following criteria:

$|t_s| \le |c_d s + t_n \tan\varphi_d| \rightarrow$ slip.

$t_n \ge -R_T s \rightarrow$ Tension.

R_T = Tensile strength,

s = surface area of band.

slip?

YES

Truncate $\mathbf{t}_{n+1}^{i}$ to tolerable values, *i.e.* $(t_s)_{n+1}^{i+1}$ $|c_d s \tan\varphi_d|$

NO

Tension?

YES

Set $\mathbf{t}_{n+1}^{i}$ 0, and $\delta\mathbf{g}_{n+1}^{i}$ in the normal direction to maximum aperture value.

NO

Update displacements: $\mathbf{u}_{n+1}^{i+1}$ $\mathbf{u}_{n+1}^{i}$ $\delta\mathbf{u}_{n+1}^{i+1}$,

$\mathbf{g}_{n+1}^{i+1}$ $\mathbf{g}_{n+1}^{i}$ $\delta\mathbf{g}_{n+1}^{i+1}$.

Update traction forces: $\mathbf{t}_{n+1}^{i+1}$ $\mathbf{t}_{n+1}^{i}$ $\delta\mathbf{t}_{n+1}^{i+1}$.

Go to 4 to evaluate $\boldsymbol{\psi}_s$ (g).

Bulk Convergence?

YES

Set:

$\mathbf{u}_{n+1} = \mathbf{u}_{n+1}^{i+1}$,

$\mathbf{g}_{n+1} = \mathbf{g}_{n+1}^{i+1}$,

$\boldsymbol{\sigma}_{n+1} = \boldsymbol{\sigma}_{n+1}^{i+1}$,

$\mathbf{t}_{n+1} = \mathbf{t}_{n+1}^{i+1}$.

- Check bifurcation locally for each element for converged state, i.e. $(\det(\mathbf{n}:\mathbf{L}:\mathbf{n})=0)$
- Go to next load increment with a change in configuration if bifurcation ever occurs.
- Reset information concerning element topology, bandwidth, gauss points etc. and go to 1.

NO

Calculate iterative strains

↓

Classical plasticity calculations

↓

calculate residual $\boldsymbol{\psi}_{\Omega}(\mathbf{u}_{n+1}^{i+1})$ on going to step 4.

Chapter 7

Numerical Results

7.1. Introduction

Many practical examples of application become amenable to analysis by means of the model formulated in Chapter 4. In a first stage, in order to pursue an investigation of fundamentals, a numerical assessment of the discontinuity element will be presented by an eigenvalue analysis and a patch test. Then, the model is applied to simple test problems in order to show exactly how it describes phenomena of localization. In a last stage, the numerical tests will shift over to a general boundary value problem. Comparison is made with the conventional continuous formulation in order to illustrate the method. It is important to underscore at this point that all the cases examined herein are restricted to a fairly elementary situation with no fluid flow regime.

7.2. Numerical assessment of the method

7.2.1 Eigenvalue analysis

The soundness and merit of the discontinuity interpolation functions described in Chapter 4 can be verified by an eigenvalue method approach which in other words gives a measure of

strain energy content associated with the element under several deformational modes. The decompositions of the element stiffness matrix into its consistent eigenvectors and associated eigenvalues are a necessary check on the validity of the element. This analysis was conducted to study the net effect of the discontinuous interpolation functions, their ability to reproduce localized modes and sensitivity towards convergence of the solution. The stiffness matrix as derived from the strain energy based upon the modified Principle of Virtual Work is used. A typical form of the element stiffness matrix for a QD4 element is recalled below for clarity of exposition:

$$[\mathbf{K}] = \begin{bmatrix} \mathbf{K}^{e}_{\Omega\Omega} = \int_{\Omega} \mathbf{B}^{(\alpha)^T} : \mathbf{L} : \mathbf{B}^{(\alpha)} \, d\Omega & \mathbf{K}^{e}_{\Omega S} = \int_{\Omega} \mathbf{B}^{(\alpha)^T} : \mathbf{L} : \mathbf{B}^{(\beta)} \, d\Omega \\ \mathbf{K}^{e}_{S\Omega} = \int_{\Omega} \mathbf{B}^{(\beta)^T} : \mathbf{L} : \mathbf{B}^{(\alpha)} \, d\Omega & \mathbf{K}^{e}_{SS} = \int_{\Omega} \mathbf{B}^{(\beta)^T} : \mathbf{L} : \mathbf{B}^{(\beta)} \, d\Omega \\ & \quad + \int_{\Gamma_{sb}} \mathbf{N}^{(\beta)^T} : \boldsymbol{\eta} : \mathbf{N}^{(\beta)} \, d\Gamma \end{bmatrix} \tag{7.1}$$

Two cases on discontinuity locations have been considered, namely the discontinuity cutting across two opposite sides of the QD4 element, denoted by option 1, and across two adjacent sides, denoted by option 2. The study has been performed on a master element of side length one unit in plane strain elasticity using a Young's modulus of 1.0 unit and Poisson's ratio of 0.3. The corresponding properties for the shear band were 1.0 unit for the shear stiffness and 1000.0 units for the normal stiffness to avoid any separation or penetration modes. Off-diagonal stiffness terms in the shear band matrix were set to zero, implying no coupling between normal and tangential slip displacements at the shear band interface.

Due to element configuration which consists of 8 displacement degrees of freedom at the external nodes and 4 slip displacement degrees of freedom at the localized nodes, the size of the stiffness matrix in Eq. (7.1) becomes a 12x12 matrix.

The eigenvalue problem is mathematically recalled. It states that for an element possessing non-zero eigenvalues, the eigenvectors of the stiffness can be found by solving

$$\begin{bmatrix} K_{\Omega\Omega} & K_{\Omega s} \\ K_{s\Omega} & K_{ss} \end{bmatrix} \begin{Bmatrix} X_\Omega \\ X_s \end{Bmatrix} = \lambda_i \begin{Bmatrix} X_\Omega \\ X_s \end{Bmatrix} = f_i, \tag{7.2}$$

in which X_Ω and X_s are nodal displacements for the continuous and discontinuous components respectively, and f_i are the nodal loads made proportional to the nodal displacements through the constant λ_i, namely the corresponding eigenvalue.

Three zero eigenvalue modes corresponding to the combination of translation and rotation of the continuum part were obtained. Relative displacements at the localized nodes were found to be zero in these particular instances in order to permit rigid body motion, refer to Section 4.9 for more details. From an energy point of view, this implies that the rigid body motion does not produce any straining, and hence stresses are zero.

The remaining nine non-zero eigenvalues and deformation modes emerge as a result of the amalgamation of modes belonging to the continuous and discontinuous components. These are illustrated in Figs. 7.1 and 7.2. with associated energy values. It is interesting to note that the five basic deformation modes pertaining to constant strain and linear strain rates are combined with those of the discontinuity surface.

The amount of strain energy related to the non-zero eigenvalue modes accounts for energies absorbed in deforming the continuum and the interface, as well as the continuum interface interaction. In other words, premultiplying both sides of Eq. (7.2) by the eigen vector results in the following:

$$\langle X_\Omega \quad X_S \rangle \begin{bmatrix} K_{\Omega\Omega} & K_{\Omega S} \\ K_{S\Omega} & K_{SS} \end{bmatrix} \begin{Bmatrix} X_\Omega \\ X_S \end{Bmatrix} = \lambda_i, \tag{7.3}$$

since the eigenvector is normalized as $\langle X_\Omega \quad X_S \rangle \langle X_\Omega \quad X_S \rangle^T = 1$. Further expansion of the above leads to:

$$\lambda_i = X_\Omega^T K_{\Omega\Omega} X_\Omega + X_S^T K_{SS} X_S + X_\Omega^T K_{\Omega S} X_S + X_S^T K_{\Omega\Omega} X_\Omega, \tag{7.4}$$

i.e, the eigen value corresponds to the sum of twice the continuum strain energy, twice the interface strain energy and continuum interface coupling energy components. This implies that, referring back to the eigen modes in Figs. 7.1 and 7.2, the strain energy associated with modes 11 and 12 in both cases are very high, thus suggesting that they are least likely to occur. Since in general the response of the element during an arbitrary loading will be a linear combination of eigen modes, then separation and penetration of nodes at the interface will not take place so long as the boundary conditions are not in accord with those particular modes.

7.2.2 Patch test

It was proven in Chapter 4 that the assumed strain operator does not reduce the order of convergence of the scheme and that the shear band element should pass the patch test.

In this section, a patch of elements (10 elements), see Fig. 7.3, is subjected to a constant strain field and one investigates if it reproduces exactly the constitutive behaviour of the material and correct stresses as the patch becomes infinitesimally small. Interior nodes have been included in the region and an irregular mesh has been chosen to avoid any fortuitous self correction by symmetry. A plane strain problem is considered on the patch with the material governed by linear isotropic elasticity whose properties are summarized in Fig. 7.3. The finite element procedure is based on the displacement formulation using

classical 4-noded and 3-noded isoparametric shape functions, and linear discontinuous shape functions for the shear band.

Since the stiffness computation includes only first derivatives of displacements, and no derivative for slip displacements, the formulation converges provided the patch test is satisfied for all linear polynomial solutions of displacements. The patch test is performed using a 2x2 Gaussian, standard quadrature to compute each element stiffness. Nodes 1 and 2 are restrained both horizontally and vertically, while nodal displacements values of -0.1 unit are prescribed at nodes 3 and 4. The patch of elements is compared with a one single element, using option 1 in which the shear band cuts across two opposite edges the same way as in the patch of elements.

The values of displacements, hence strains and stresses, computed for the interior of the patch verify a constant field and satisfy the patch test. The solution obtained for displacements u,v and slip displacements g_x and g_y are given as :

$$u = -0.18784\ 10^{-2}$$

$$v = 0.09962\ y + 0.37665\ 10^{-3}$$

$$\left.\begin{array}{l} g_x = -0.18784\ 10^{-2} \\ g_y = -0.37667\ 10^{-3} \end{array}\right\} \text{ uniform along shear band}$$

This displacement field with the accompanying slip displacement field (g_x and g_y), see also Table 7.1, produce zero body forces and zero stresses except for

$$\sigma_y = -0.09962$$

and interface traction forces

$$t_s^1 = -0.01916$$

$$t_n^1 = -0.09579$$

The same solution can be reproduced from the one element patch test which involves the use of discontinuous shape functions for a quadrilateral. Alternatively forces compatible with the state of stress obtained in the previous tests were applied to nodes 3 and 4 and exactly the same results for stresses and strains were recovered.

Table 7.1 Patch test solution for Figure 7.3

Nodes			Displacements		Slip displacements	
	x	y	u	v	g_x	g_y
1	0.0	0.0	0.0000000	0.000000		
2	0.0	0.0	0.0000000	0.000000		
3	1.0	1.0	-0.0018784	-0.100000		
4	0.0	1.0	-0.0018784	-0.100000		
5	0.31	0.69	-0.0018784	-0.069117		
6	0.80	0.80	-0.0018784	-0.080075		
7	0.20	0.25	0.0000000	-0.024906		
8	0.65	0.35	0.0000000	-0.034868		
9	0.0	0.40			-0.0018784	-0.00037665
10	0.152	0.430			-0.0018784	-0.00037665
11	0.250	0.450			-0.0018784	-0.00037665
12	0.50	0.50			-0.0018784	-0.00037665
13	0.714	0.543			-0.0018784	-0.00037665
14	0.857	0.571			-0.0018784	-0.00037665
15	1.000	0.600			-0.0018784	-0.00037665

7.3 Simple boundary value problems

Many practical examples of application become amenable to analysis by use of the foregoing special discontinuity element. However in order to pursue an investigation of fundamentals, the cases herein presented are restricted to fairly elementary configurations for a preliminary study.

7.3.1 Mini-footing problem

An initially homogeneously stressed region is made to succumb to localization phenomena by artificial generation of shear bands within it, see Figure 7.4. A uniformly distributed load is applied on the element edge denoted by nodes 4 and 5. The medium is considered elastic and all geometric and material non-linearity is assumed concentrated in the shear band.

Shear bands are artificially made to branch from different sites in the mesh involving elements 1, 3, 2 and 4. Initiation and orientation of the shear band are dictated by a Mohr-Coulomb type of criterion based on the principle of maximum stress obliquity. Furthermore, in the event of conjugate directions, the orientation compatible with prevailing kinematic constraints is chosen. In order to establish compatibility between discontinuous (shear band) elements and adjacent continuum elements, the tip of the band is prescribed as a *node* of zero slip in the computations. Figure 7.5 depicts the distribution of typical displacements in such situation when the shear band is not fully developed, with the tip located at the boundary of two elements.

The mobilized slippage tendency indicates that most of the movement occurs in the vicinity of the applied loads. Also the stress distribution with the shear band in place reveals a substantial difference from the one expected for the unfaulted case, i.e, stresses are released and principal stress rotations reduced in regions outside the band. For example the rotation of principal stresses adjacent to line 1-4 in Figure 7.4 may be noted. This suggests that loads tend to localize along the band leaving the surrounding areas in an

unloading state. Moreover, stresses in element 2 are very small in comparison with others while some tension develops in elements 1 and 4 as one segment of corresponding shear band elements tries to detach itself from the rest of the elements. Here the normal stiffness of the shear band has been prescribed at a high enough value that tensile opening or separation is prohibited although the shear band curves upwards or downwards. If the load were to be incremented further in the analysis, a new stress field would have to be found and a new equilibrium configuration established with the band penetrating further into element 5. However the shear band orientation in other elements would have to be adjusted until a new equilibrium state is reached. Finally the mobilized shear stresses plotted at Gauss integration points along the shear band typically show the well known trend of peak values at the leading tip with lesser values at sites where most movement has taken place.

7.3.2 Mini-embankment problem

The numerical example shown in Figure 7.6 relates to a slope problem involving an embankment subjected to loads at the crest. A very coarse mesh is used since the object of the analysis is to illustrate the effectiveness of the kinematics. An elastic analysis was performed. Based upon the principle of maximum stress obliquity or the bifurcation expression in equation (3.7), shear bands were artificially embedded in the mesh by activating the discontinuity shape functions which interpolate the slip displacements.

A noteworthy outcome of the analysis is the promotion of enhanced kinematics under shear band mode of deformation. By way of contrast, a conventional analysis does not capture the discontinuous behaviour since localization tends to be diffused and smeared out in the mesh, unless the latter is properly designed. Figure 7.7 shows the distribution of internal traction forces, hence mobilized shear stresses along the shear band. However, due to bending of the shear band as it daylights to the free surface, the element tends to lock itself at kinks. This explains the drop in internal traction distribution. In fact for a finer mesh, the distribution would smooth out. Figure 7.8 illustrates the levels of contours of

shear strains. It is observed that the gradient of shear strains becomes higher in the enhanced analysis when compared with a conventional continuum run in Figure 7.9. This demonstrates the promotion of localization and highlights the significance of such calculations.

7.4 Rigid punch problem

The classical punch problem is presented in this section. The material is the conventional incompressible isotropic elastic hardening/softening plastic Prandtl-Reuss material. Figure 7.10 shows the two-dimensional finite element representation of the problem geometry and notation. The punch is represented by a strip of elements ten thousand times stiffer than the supporting medium and loading is achieved by a central vertical force P. The strip footing elements correspond to a total width of B while the supporting medium extends $10B$ wide and $5B$ deep so as to preclude any boundary effects.

7.4.1 Continuous case

A perfectly plastic medium—plastic modulus H equals 0—is considered in the first case with the conventional finite element scheme. The load P was applied incrementally to the maximum failure load. In order to avoid problems of convergence, a consistent linearization of the finite element equations as proposed by Simo and Taylor[1985] is adopted. It has been proven that the use of a consistent tangent coefficient matrix derived consistently from the integrated constitutive equation—combined with a closest point projection—results in an iterative scheme which preserves the asymptotic rate of convergence of Newton's method.

The computed load-displacement curve is shown in Figure 7.11. The failure load is captured quite accurately by the numerical solution but one should note that no localization occurs because of the symmetry of the loading, geometry and homogeneity of the material properties. The development of the plastic zone under the punch with increasing settlement

is shown in Figure 7.12. The plastic growth spreads about 2.5B deep under the footing and extends one full width B on either side of the punch. It is seen that the plastic growth is slightly less extensive than the one postulated by Hill's slip mechanism.

An attempt to promote localization in the medium was done by making the medium initially inhomogeneous by placing a weak element with plastic modulus ratio $H/2G$=−0.048 beneath the left corner of the rigid footing. The elastic shear modulus is herein denoted by G and the material strength characterized by c, the cohesion, or σ_y^0 , the uniaxial yield strength. Figure 7.13 shows the constitutive relationship relevant to the weak element. It was found that the load-displacement curve basically remains identical to the one obtained for the homogeneous case. Also, the spreading of the yield zones follows sensibly the same trend shown in Fig. 7.12 for the homogeneous case. This shows that localization effects are difficult to capture using the classical finite element formulation—this even if artificial inhomogeneities such as a weak element are introduced.

7.4.2 Discontinuous case

The finite element method with the possibility of an internal discontinuity is next tried out to examine the performance of the proposed method.

The domain of interest is initially discretized with ordinary elements and the bifurcation criterion is checked at every loading step. Once bifurcation is detected, the standard element is replaced by the discontinuous one, and the stress-strain as well as the other history dependent state quantities must be then extrapolated from original Gauss points into the new integration points required by the new element. A detailed description of the integrating scheme is given in Appendix B. Alternatively, one could possibly find the band orientation and its location from a preliminary analysis, and then place the discontinuous element there from the beginning of the analysis. However, this alternative method does not represent the actual locations of the shear band segments as they develop

during loading because the determination of the path is history dependent. The direction the next band segment takes depends on the already in place previous bands in the mesh.

In the present study, as the developments are still at a preliminary stage, the complexities involved in locating and constructing the shear band, as it evolves in the mesh, are by-passed by using the simple discontinuous triangular element presented in Chapter 4. As such, it suffices only to check bifurcation criterion at the centroid (also single Gauss point) of the element. The very first shear band in the analysis is made to pass through the centroid of the element. For subsequent loadings, the newly formed shear band in the adjoining element is simply shifted and made to connect with the leading tip of the previous band since the stress-strain quantities are supposed to be constant over the element just prior to localization.

Bifurcation conditions which emerge from equation (3.7) are numerically checked at each Gauss integration point during the loading process. Details of the numerical procedure were previously covered in Section 6.3 of this thesis. A shear band is precisely located in the weak element, and an inclination of 4.5° with respect to the vertical is computed. Conjugate shear band directions are usually obtained. The direction which is consistent with the prevalent boundary conditions is chosen. However, in less obvious situations, the strain rate prior to localization and the one at the onset of bifurcation are compared. The direction which gives more or less the same strain rate at the point under consideration just before bifurcation is considered as the one the shear band will eventually follow. This should be equivalent to choosing the direction which produces the most dissipation through inelastic dissipation in the band, in other words, the one which minimizes the potential energy of the system.

As soon as the bifurcation criterion is satisfied the discontinuous shape functions are triggered with relative displacements along the shear band following a simple Coulomb contact law with a cohesive strength of 10 units, and no frictional resistance. The normal stiffness of the shear band is made of the order of 10^8 units to avoid separation of the band,

and a shear stiffness of 10^5 units is chosen, which is within the same magnitude of the modulus of the bulk material. The features of the governing constitutive relationship for the shear band is given in Fig. 7.14.

Figure 7.15 shows the progression of the shear band at three selected stages, as the footing load is gradually increased. At an early stage of the punch, Figure 7.15a, four elements have already bifurcated, and the shaded area shows the yield zone. It is clear that yielding localizes in the vicinity of the shear band, although some yielding also occurs beneath the right corner of the footing. This is probably due to stress concentrations at the corners.

As the load is further increased (Figure 7.15b), more yielding occurs and the plastic zone migrates to adjacent elements as the tip of the band penetrates further into the mesh. The resulting footing load must increase since plastic deformations can still take place—at least in the neighbourhood and in the shear band. There is a tendency for the ambient zone to plastify together with the shear band.

At an advanced stage of the loading (Figure 7.15c), the plastic zone has now become quite extensive, but is still clustered around the shear band. Consequently, this provokes a levelling-off of the load-displacement curve. Since, the achievement of a stable solution becomes more and more difficult, displacements are instead prescribed as opposed to loads. Figure 7.16 illustrates the kinematics of the problem with the shear band fully developed. Note the discontinuous nature of the displacement field, and the tilt of the footing to accommodate the rotational nature of the kinematics.

The curves of slip displacements along the shear band at selected normalized footing displacements are plotted in Fig. 7.17. The results show that the slip displacements are significantly affected by the presence of kinks between two connecting shear band segments. The slip displacement tends to drop at these kinks, but the general trend follows a gradual decrease of slip towards the tip of the band where there is no movement. As the tip advances in the mesh, the slip displacements generally increase as shown by the shift of

the curves. When the band has daylighted, it is noticed that very little slip occurs in the upper segment near the free surface. There is a phenomenon of locking of the mesh in the lower segment where the material is squeezed.

Figure 7.18a shows the fully developed shear band together with the Prandtl's slip lines. The shear band computed is very close to those slip lines, thus indicating that the model can capture similar mechanisms as postulated by Prandtl. The behaviour of the shear band can be elucidated by examining the distribution of traction forces along the interface, as shown in Fig. 7.18b. It is noted that the force distribution trend is consistent with the strength of the shear band. In regions of the shear band located near point A, considerable slip has occurred such that the corresponding traction force is kept to a limiting value of 10 units, the strength of the shear band. However, the segments of the shear band near point B undergo less slippage, to such an extent that the corresponding traction forces are low. It is observed that this phenomenon is somewhat disturbing due to the fact that slippage should have been uniform throughout the shear band as it daylights. This is attributed to the fact that there are kinks at the connections of the shear band segments at locations with an abrupt change in orientation. These kinks seem to hinder slippage such that further deformation in the form of plastic flow spread in the ambient region instead of in the band itself. The phenomenon apparently produces a spurious plastification which appears to lead to an unrealistically high footing load.

The new load-displacement curve is finally shown in Figure 7.19. The bearing capacity is marginally lower than the one obtained without any shear band because of the allowance made for a discontinuous displacement field and the tilt of the footing. Also, it is thought that the low cohesive strength of the shear band may be a contributing factor which led to such a low bearing capacity value. It seems that a substantially lower value should have been obtained considering the low resistance of the shear band compared to the ambient material strength. This is partly due to the problem of locking of slippage at kinks between two shear band segments, which makes the surrounding material yield instead of

constricting plasticity into the band. Thus, the introduction of this error together with the nature of the analysis lead to a bearing capacity which is higher than the theoretical limit load and this is consistent with an upper bound solution.

The load-displacement relation seems to show some softening in the ultimate range, but this may be apparent and purely due to the switching of scheme from loading to prescription of displacement. The last point on the load-displacement curve in Figure 7.19 represents an equilibrium state which has not fully converged, most probably due to the shear band having daylighted.

The effective plastic strain history for a point 'A' in the element number 44 (see Fig. 7.18) found just below the left hand corner of the footing is given in Figure 7.20. During the initial phase, both the strain fields in the localized and non-localized zones are identical since there is no shear band. During subsequent deformation, the effective plastic strain for a point in the shear band increases steadily, while plasticity is less extensive for a point outside the localized zone. In the localized zone, the increase in effective plastic strain indicates a continuous plastification. On the other hand, in the non-localized zone, the effective plastic strain increases slowly but remains at a relatively low value when compared with the extent of plasticity in the shear band. It seems that one would expect very low plastic strains or values close to zero in the non-localized zone so as to produce an unloading phenomenon with a decrease in effective stresses. However, in this present analysis, there is still some residual plastic strains in the non-localized zone due to the locking phenomenon occurring at kinks. Even though this shortcoming may look serious in the sense that it may mask the influence of localization, Fig. 7.20 certainly illustrates the general tendency of having higher plastic strains in the band and less extensive plasticity in the ambient region. This is a definite improvement over the conventional (continuous) analysis in which the plastic strains would steadily increase in a diffuse way with loading history.

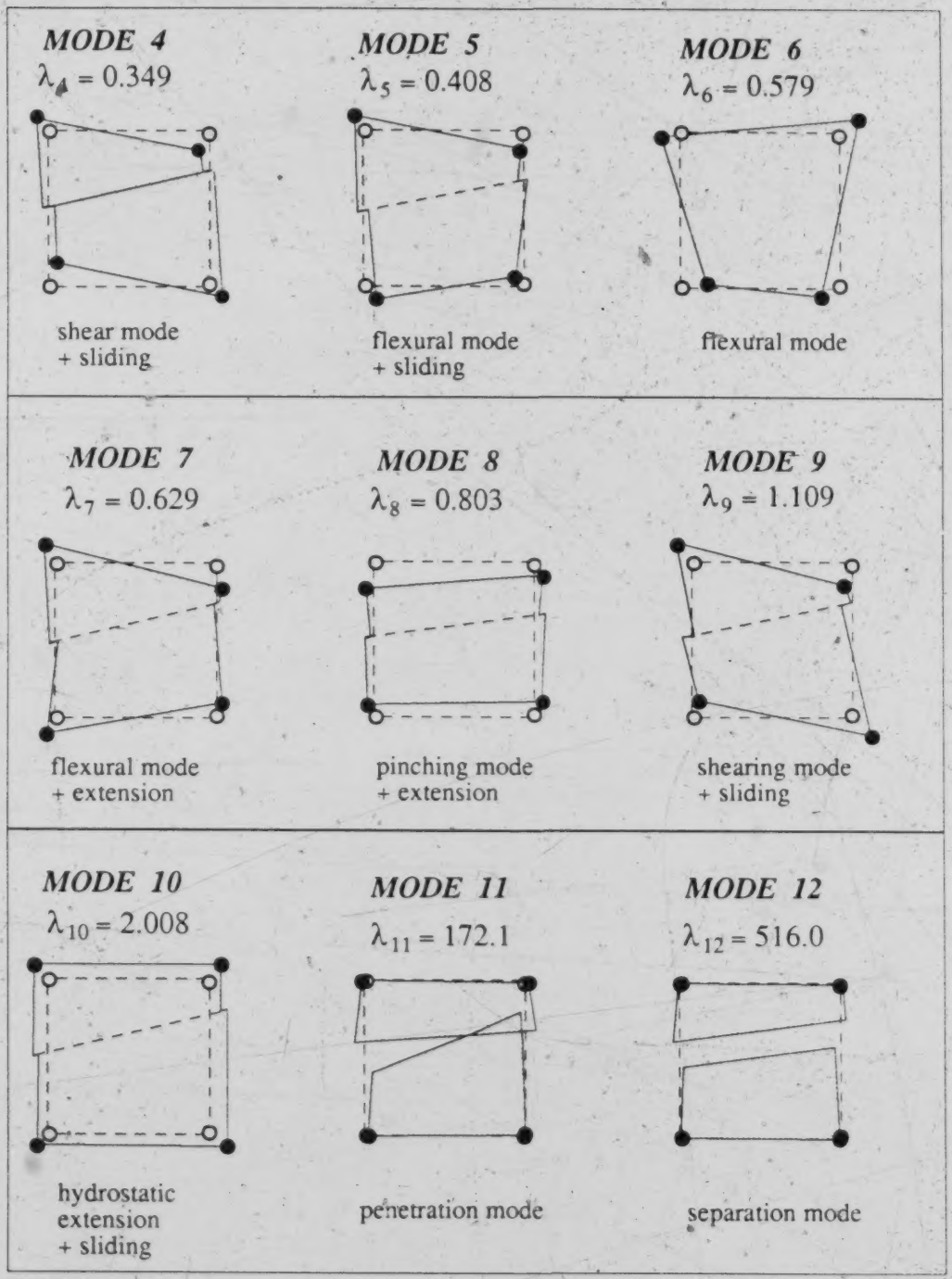

Figure 7.1 Non-zero eigen-modes for Shear Band Element QD4 (option 1) in plane strain

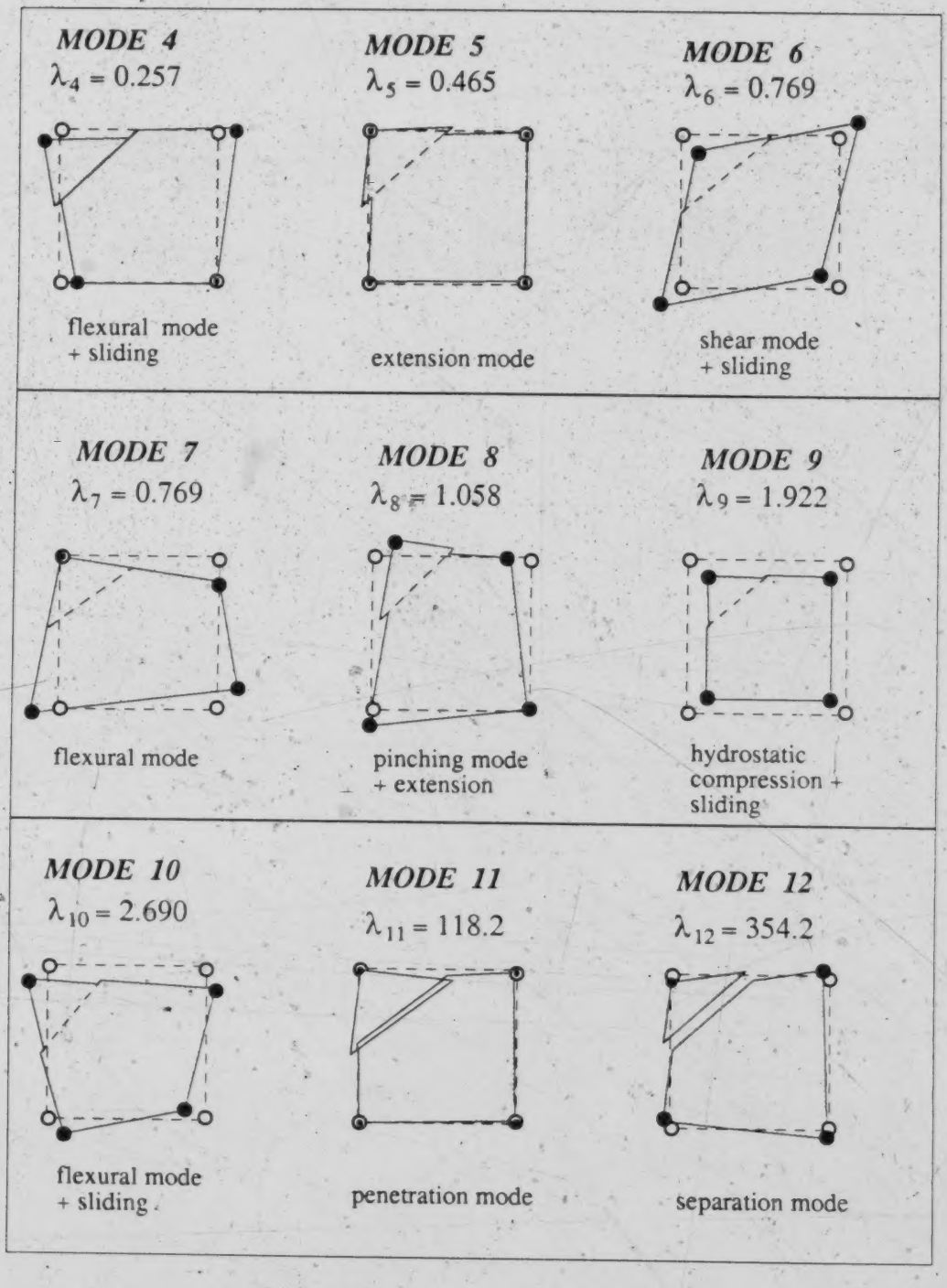

Figure 7.2 Eigen-modes for Shear Band Element QD4 (option 2)

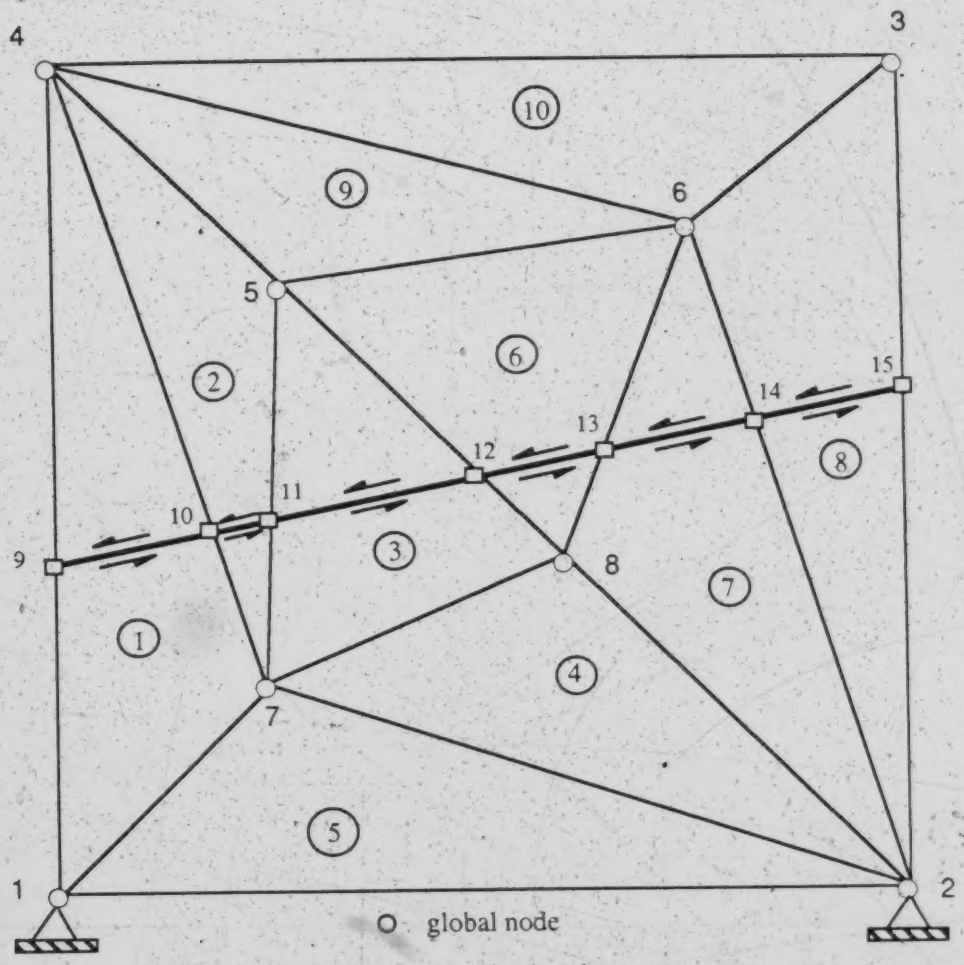

$E = 10^3$ units, $\nu = 0.0$

Shear band stiffnesses:

$\eta_{nn} = 10^5$ units, $\eta_{ss} = \eta_{sn} = 0.0$

$\eta_{tt} = 10$ units.

Figure 7.3 Patch of triangular discontinuous elements

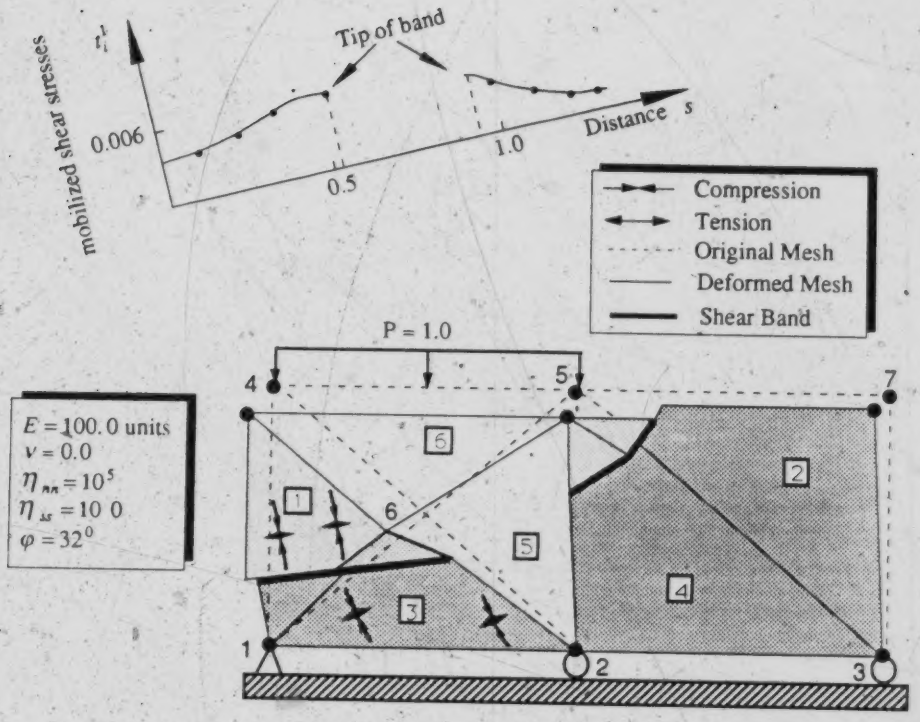

Figure 7.4. Finite element schematization of slippage along shear band

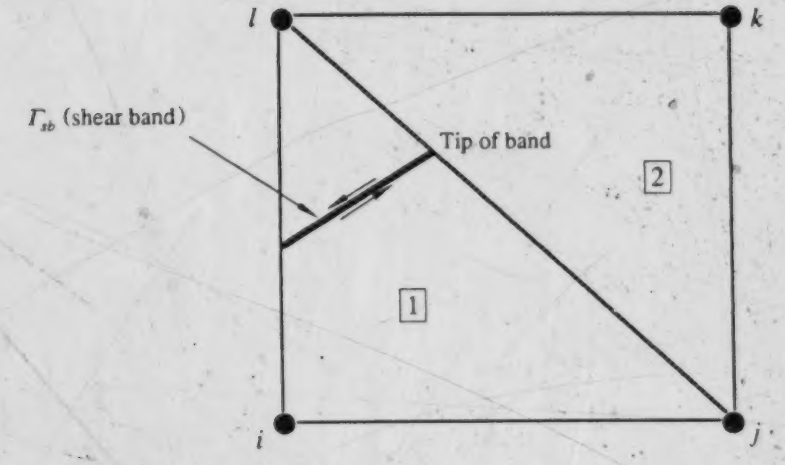

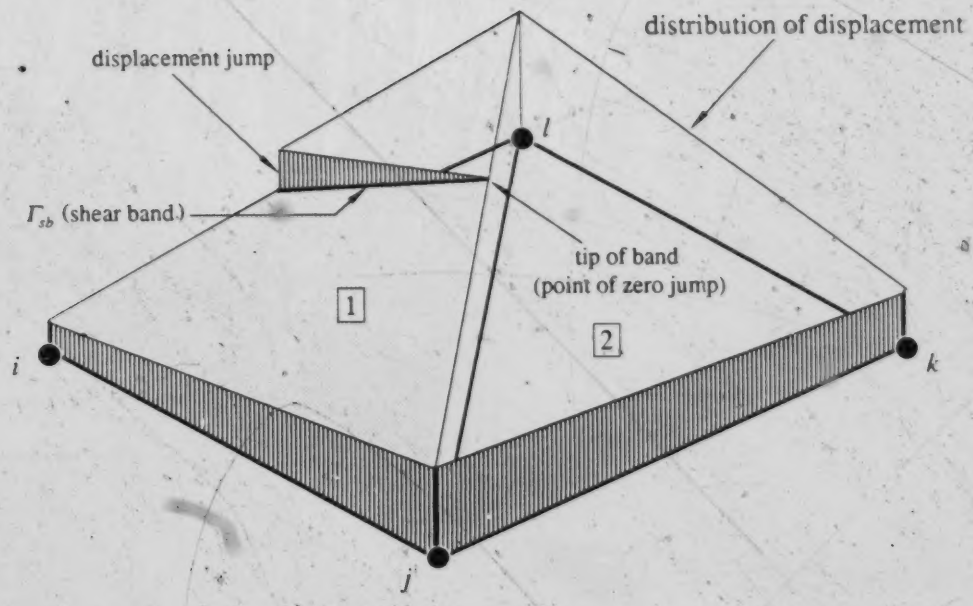

Figure 7.5 Condition of displacement field compatibility at the junction between discontinuous and continuum elements

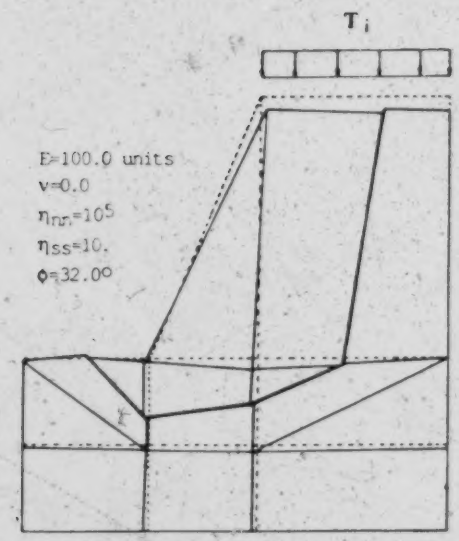

Figure 7.6 Kinematics of embankment under shear band mode of deformation

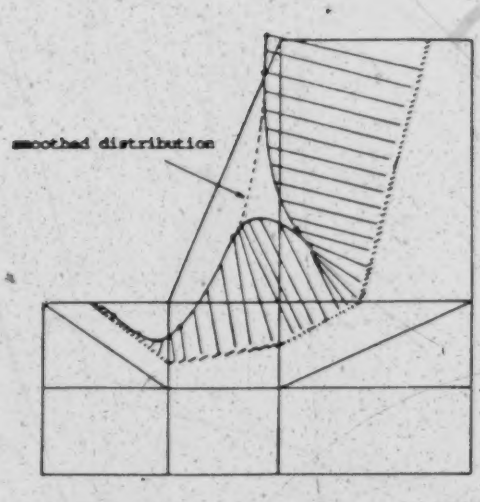

Figure 7.7 Distrubution of internal tractions along shear band

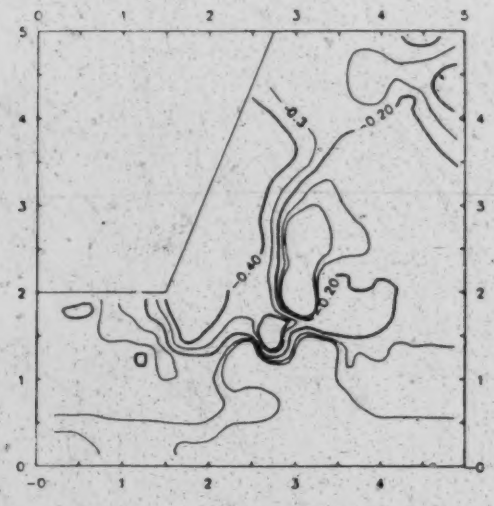

Figure 7.8 Contours of shear strains (%) as computed from proposed formulation

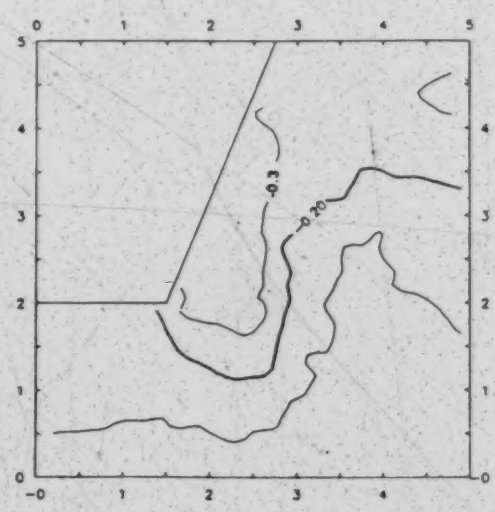

Figure 7.9 Contours of shear strains (%) as computed from conventional finite element method formulation

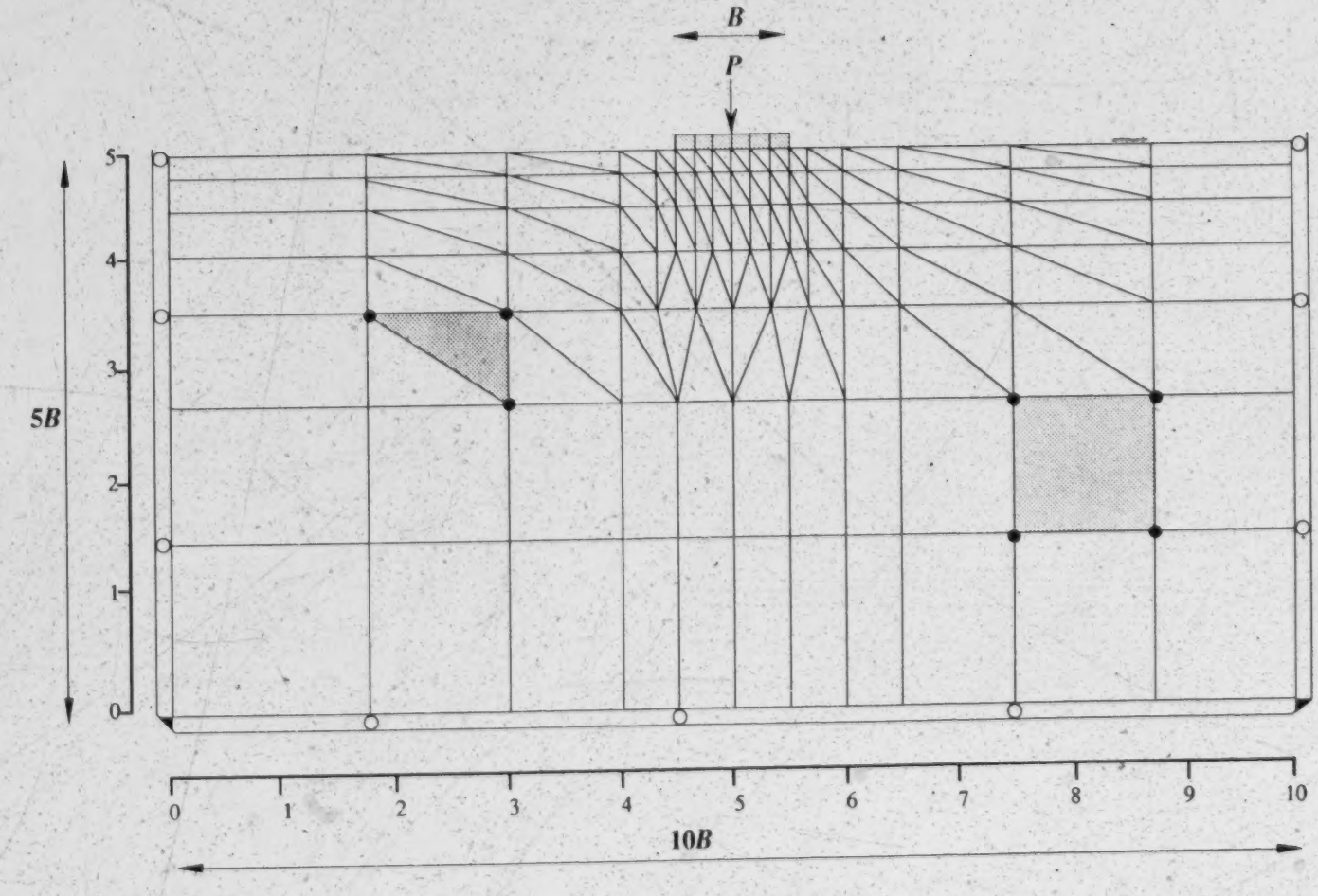

Figure 7.10 Rigid punch problem: finite element mesh

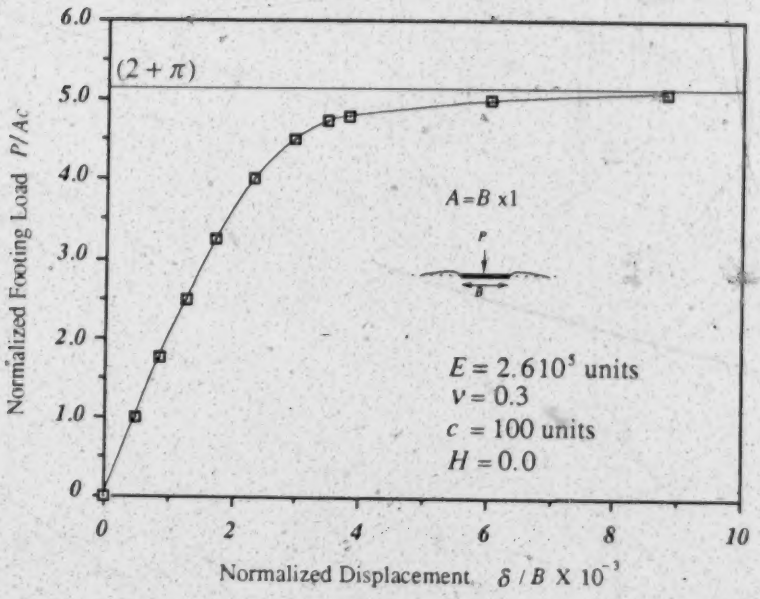

Figure 7.11 Load-displacement curve for rigid footing

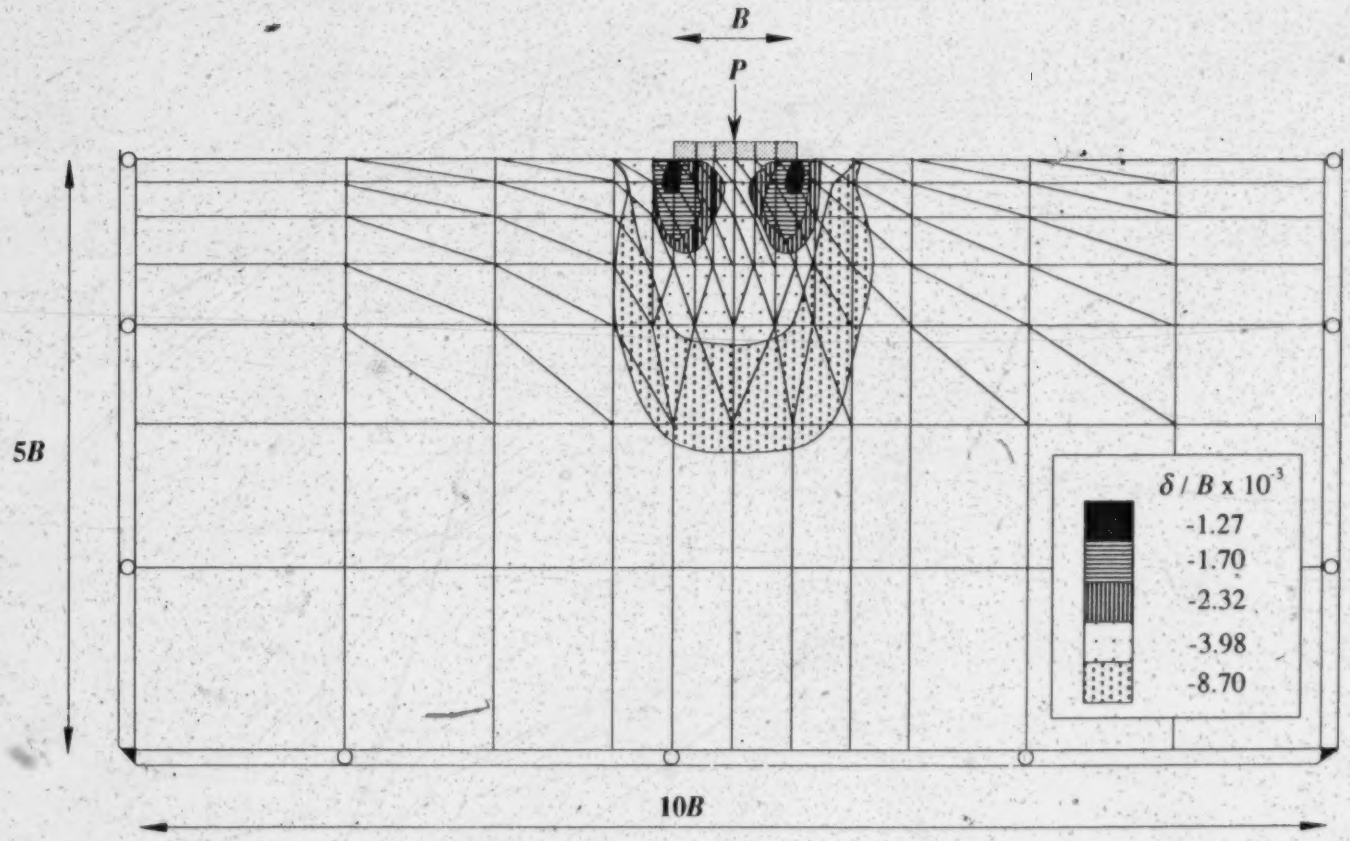

Figure 7.12 Rigid punch problem: growth of plastic zone

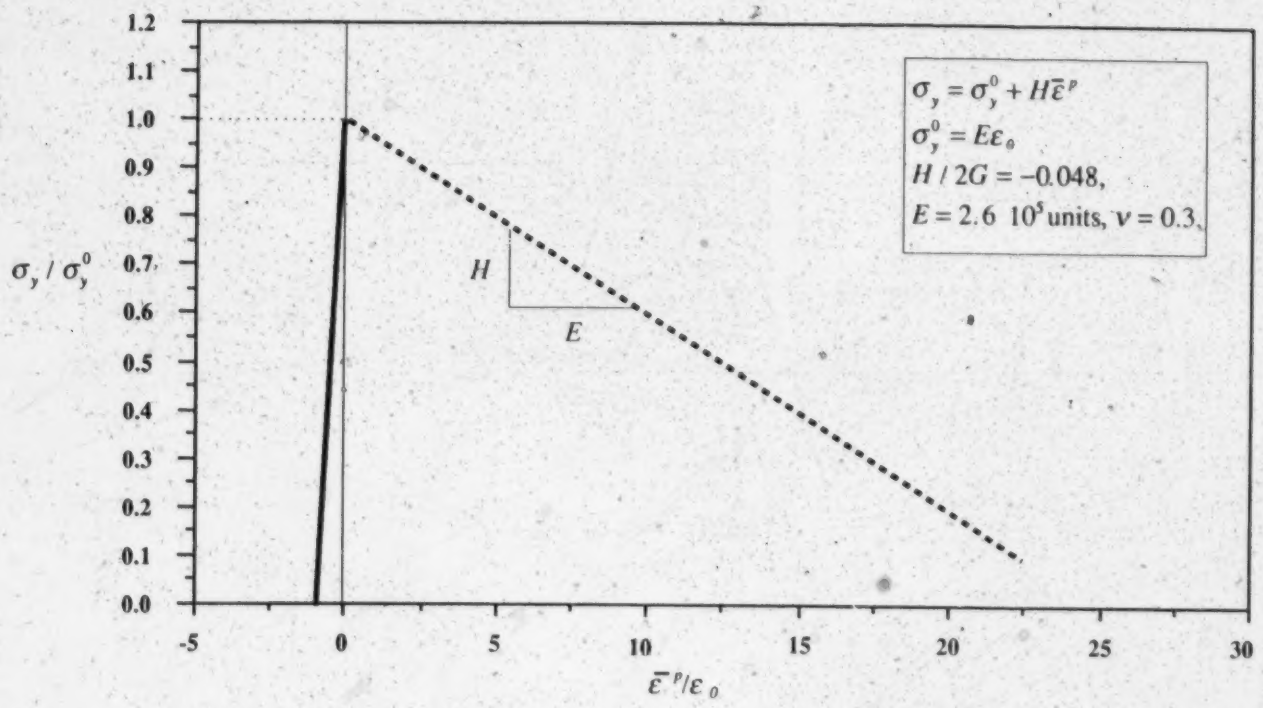

Figure 7.13 Constitutive relationship for strain-softening behaviour

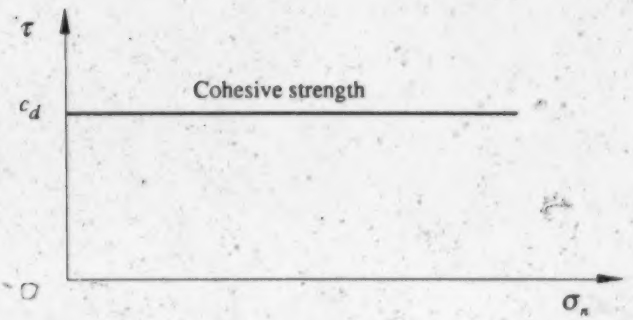

(a) Shear stress versus normal stress

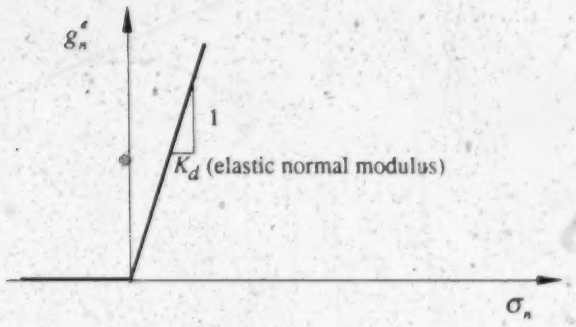

(b) elastic closing versus normal stress

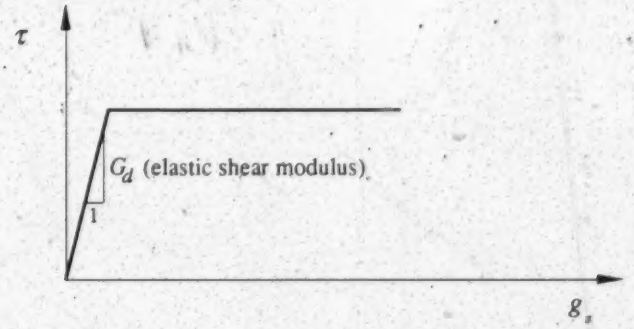

(c) shear stress versus tangential slip displacement

Figure 7.14 Constitutive law for shear band

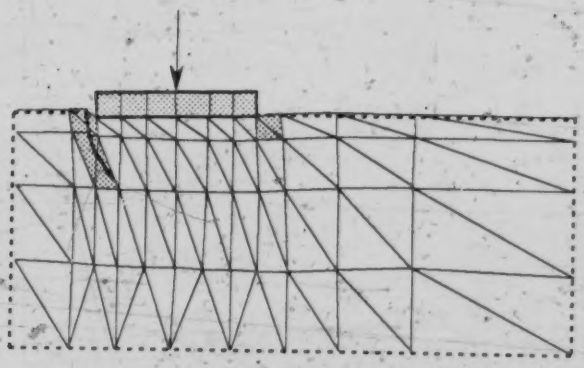

(a) $\delta / B = 2.105\ 10^{-3}$

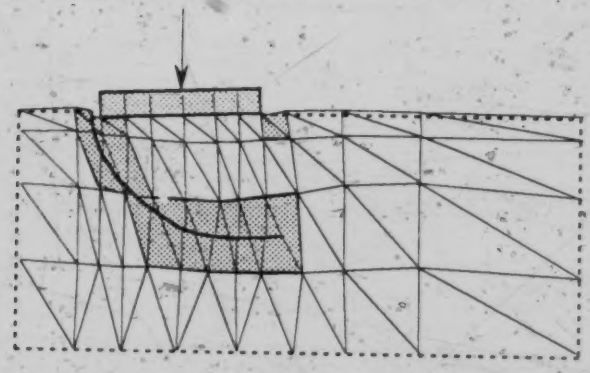

(b) $\delta / B = 3.680\ 10^{-3}$

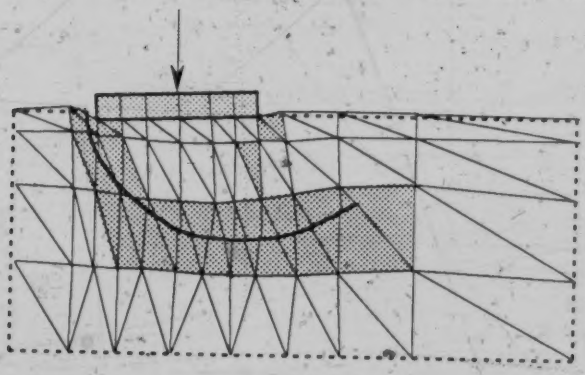

(c) $\delta / B = 4.842\ 10^{-3}$

Note that only part of the whole mesh is shown in all three diagrams

Figure 7.15 Progression of shear band during loading history

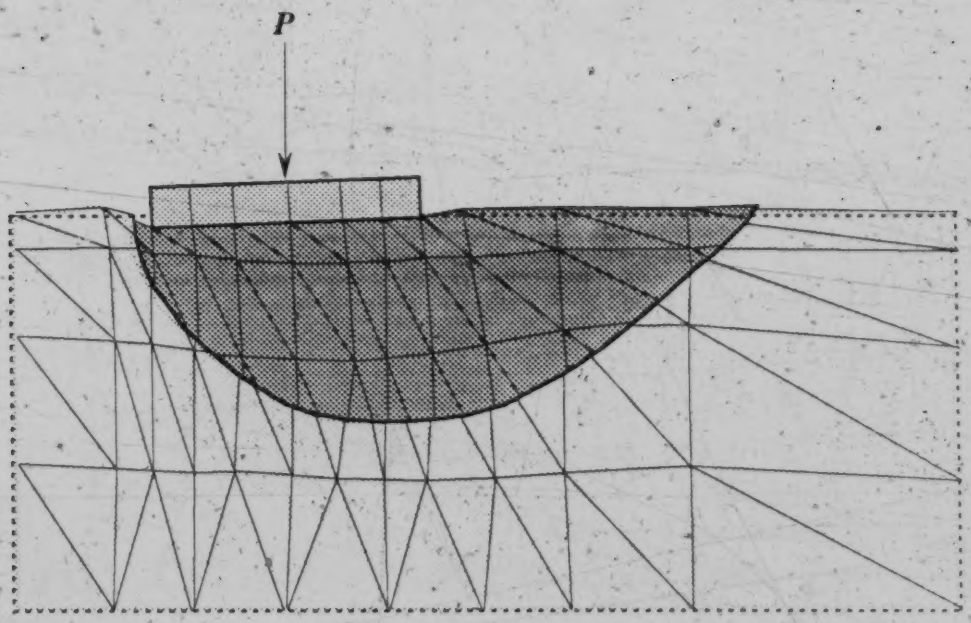

Note that only part of the whole mesh is shown

Figure 7.16 Kinematics of rigid punch problem using proposed method

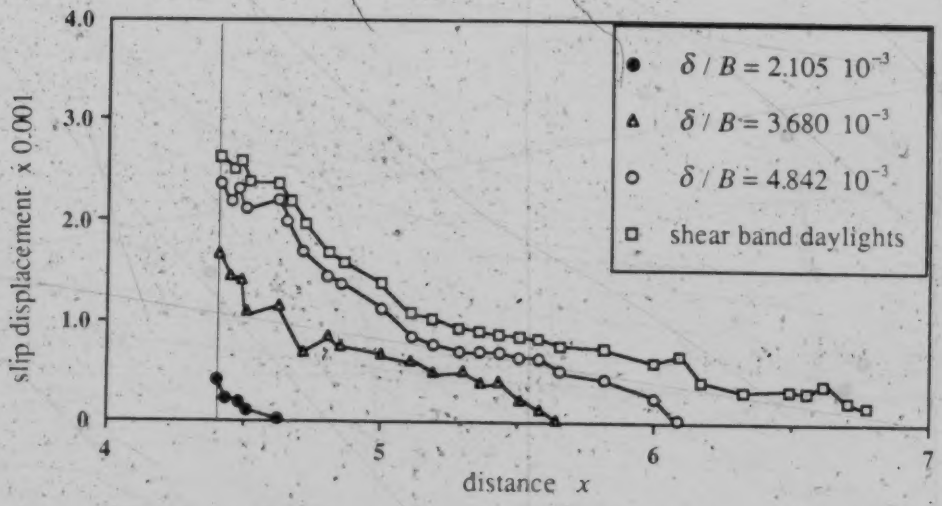

Figure 7.17 Evolution of slip displacement along shear band with loading history

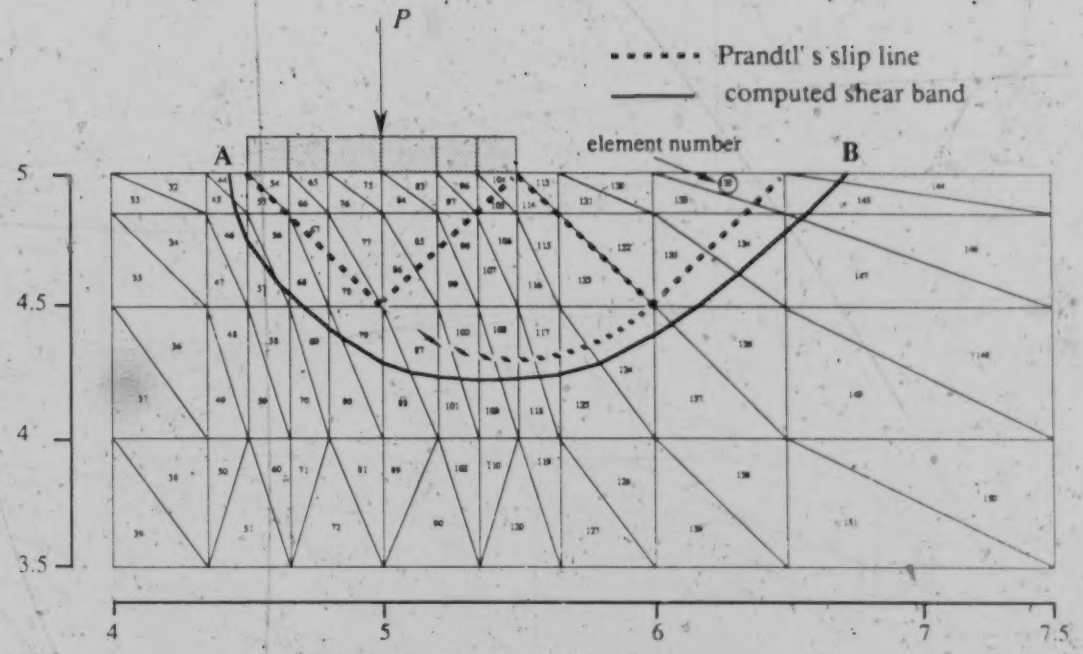

(a) part of finite element mesh with fully developed shear band

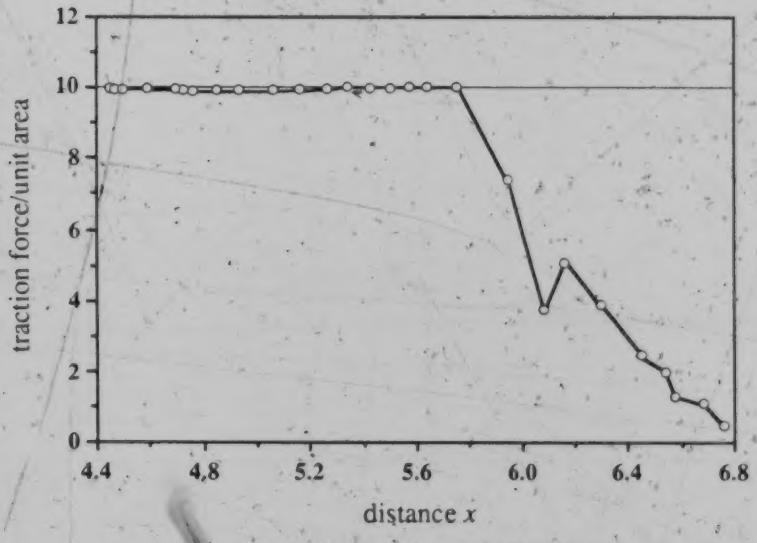

(b) shear resistance along shear band AB

Figure 7.18 Variation of shear resistance along shear band

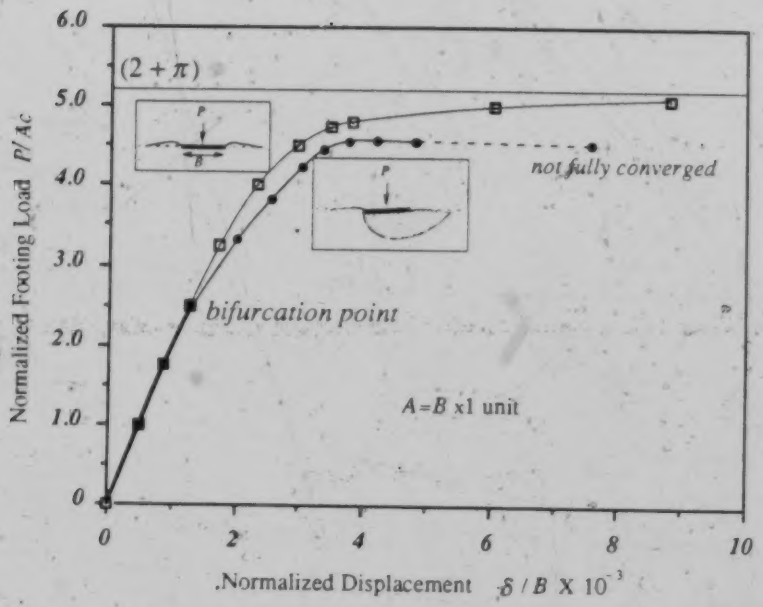

Figure 7.19 Load-displacement curve for rigid footing with localization

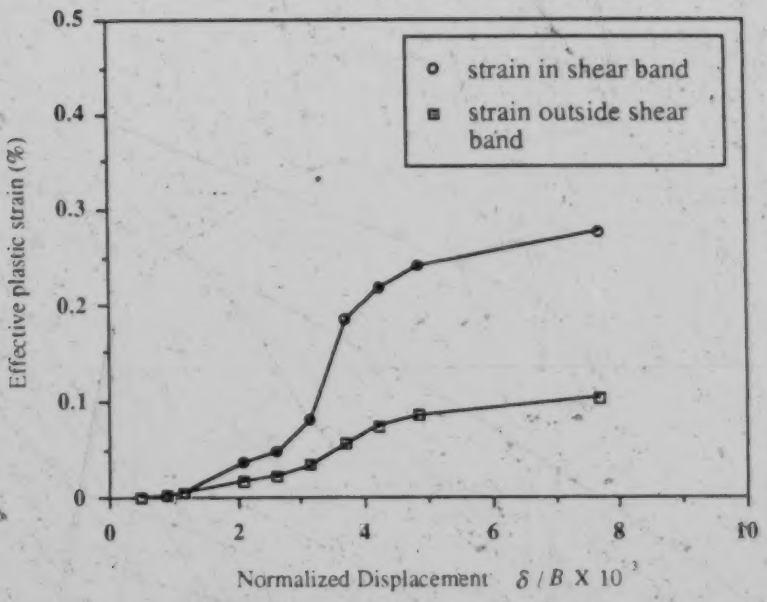

Figure 7.20 Effective plastic strain for element 44 below left hand corner of footing

Chapter 8

Conclusions and Recommendations

8.1 Conclusions

A method has been developed by which a shear band in a soil medium can be adequately modelled in a numerical analysis. The approach consisted of writing a modified principle of virtual work equation which accounts for discontinuities in the domain of interest. The formulation was then supplemented with governing fluid flow equations for a fluid saturated porous medium. Controlling field variables in the variational principle became continuous displacement, discontinuous displacement and pore fluid pressure. The finite element discretization led to the development of a special 2-D element with implicit discontinuity in its interpolation function to obviate the need to update the mesh topology during progression of an internal discontinuity surface.

The derived formulations were implemented into a finite element code to demonstrate the validity of the proposed modelling technique. In this thesis, only the drained case has been implemented—fluid pressures were excluded, and only global and slip displacements were retained as principal variables. The plasticity equations—J_2 plasticity—for the bulk material have been solved by a Newton Raphson algorithm using

the notion of consistent tangent operator for rate independent elasto-plasticity which resulted in an asymptotically quadratic convergence rate. Post peak failure—engendered by the spreading of the shear band—was governed by a simple interface relationship for rupture with constant cohesive strength. In the special shear band element developed in this study, the stresses at the shear band interface were made continuous and therefore equilibrium of internal tractions was satisfied. This feature, due to the superiority of the shape functions used, has a definite advantage over the traditional joint element where stresses being not continuous often lead to instability in convergence.

According to the various numerical examples presented, the following conclusions could be derived from the results. First of all, the developed formulation for the simulation of a discontinuous body is theoretically sound. It was shown from an eigen value analysis in elasticity that the specially developed elements were very conducive in capturing the slip mechanism produced by an internal shear band. Also, the patch test ensured the stability of the shape functions fot an assembly of arbitrarily arranged elements. It was further demonstrated that discontinuous behaviour could be captured whenever shear banding occurred with deformations subsequently localized in a restricted zone. Besides modelling shear bands, the convergence of the elasto-plastic solution obtained for the bulk material by using the consistent tangent operator was found to be very efficient and proved to be quadratically convergent.

Secondly, the model provides a framework for incorporating bifurcation concepts for the inception of shear bands. A procedure has been devised for the detection of shear bands by which the equations can be solved analytically in the program in an efficient fashion. The classical punch problem was analyzed, and the model demonstrated that the possibility of a shear band spreading into the supporting medium can lead to a consistently lower bearing capacity. This bears an important consequence on the validity of the classical finite element method analysis of structures undergoing localization. The approximation to a diffuse type of yielding may lead to an over-estimation of the bearing capacity in contrast

to a more realistic case in which yielding, taking place in a localized fashion, leads to a lower collapse load.

Thirdly, the model accounts for dissipation of energy even with a vanishing zone of localization because of the consistency of the variational principle. It is notorious that classical models, fail to do so and consequently tend to make the localization analysis mesh dependent—different levels of mesh refinements would give different localization patterns with different amounts of dissipation. Since the proposed formulation avoids this shortcoming, it can be regarded as a non-local model—prescribing an arbitrary thickness for the band in the equations provides the internal characteristic length. In this research work, a shear band thickness of unity was used. It is difficult to determine this parameter experimentally: anyway its evolution with loading history is not fully known. Finally, it is emphasized that even though the model is non-local, mesh dependency inherited from the finite element discretization/linearization of the variational principle for the evaluation of stresses cannot be avoided.

The above developments and results are significant because for the first time, to the knowledge of the author, a consistent numerical approach has been established to account for the development of a shear band in a discrete manner (not in a smeared fashion) in a soil medium.

8.2 Recommendations for future work

The modelling technique developed in this research represents a starting basis for the analysis of shear bands in geological media. However, the model is still in an embryonic state, and in order to fully realize its potential application to real engineering problems, a number of additional issues should be addressed. It is necessary to include in the analysis, the formulation of an element with an internal curvilinear shear band to better describe the geometry, and hence the kinematics of the shear band. In this research effort, the shear

band is approximated by linear segments along which the slip displacements (jumps in displacement) vary linearly. This restricts the formation of a shear band for which slip displacements are zero at both tips—the situation occurs for an isolated shear band in the interior of the finite element mesh. Also, linear shear band elements tend to produce a locking phenomenon at kinks produced at the junction of two adjoining tips of the band. This locking problem may prevent plastic deformations to develop extensively in the shear band by forcing the ambient material to plastify rather than unload elastically. An expedient solution to the above shortcoming is to refine the mesh or resort to a higher order shear band element.

A possible avenue of research leading to the improvement of the model is to contemplate the possibility of formulating a stress-displacement or hybrid shear band element. It is well-known that using a displacement type of formulation does not ensure continuity of stresses at the element boundaries. Since at the interface formed by the shear band, the stress vector has to be continuous, the displacement type of formulation may be awkward. The solution lies in writing a hybrid formulation, or imposing some internal constraint in the form of continuity in displacement gradient in a certain direction at the discontinuity front. The latter technique was employed in this research.

Stress and localization induced anisotropy are not included in the model. In other words, as the shear band forms, the bulk material surrounding the shear band does not become anisotropic due to damage. This could be partially solved by considering a damage based formulation. Also, the model is restricted to proportional loading conditions under which the behaviour of the structure changes smoothly, and not in a chaotic manner.

Although the herein algorithm—by which the shear band position once determined from trial stresses, is not corrected as the stress regime changes—works for simple cases, the model still needs considerable enhancements with regard to the correction of the shear band position with loading history. It seems that the problem of self correction for the shear band position is very similar to the search of a free surface in the analysis of unconfined

flow. However, it is thought that the propagation of the shear band cannot be fully automatized and has still to be carried out manually in the sense that at each load step, the shear band evolution has to be visually checked. Problems specially arise when there are conjugate directions for the shear band orientation. In this thesis, the orientation which is more obvious to the boundary conditions is chosen. However, it seems that the use of a more profound criterion for the choice of the correct orientation is preferable. One possibility could be evaluating the entropy of the mechanical system according to the second law of thermodynamics: for a change in state the second order change in work or entropy must to be positive. Therefore to achieve a stable state, the second order entropy change must be negative. Using this concept, the shear band direction which maximizes the entropy or energy dissipation—thus minimizes the Helmholtz free energy—will be the one which prevails.

Another issue which is worth examining is the consideration of the possibility of unifying the concepts of shear banding with tensile fracture. In this research work, it has to be emphasized that the fracture aspect, i.e possibility of the shear band opening in a tensile mode, has been overlooked and tacitly solved by prescribing a very high normal stiffness to the shear band. In the case of fracture, the driving mechanism which establishes the crack advance is the tip where the material undergoing degradation provokes a release of energy whose magnitude is congruous with the one involved in extending the crack by a certain length. In contrast, the mechanism behind the shear band mode of failure is rather associated with a material instability phenomenon.

In closure, the development of a more robust algorithm for the search of equilibrium states could result in better solutions. In this thesis, close to ultimate loads, displacements are prescribed instead in order to achieve a solution. Perhaps, a solution strategy such as the arc length method could be used. This treatment would seemingly give better results for more difficult problems than the ones examined in this thesis.

REFERENCES

Arthur, J.R.F., and T. Dunstan, [1982], "Rupture layers in granular media", *IUTAM Symposium on Deformation and Failure of Granular Materials*, Delft, pp. 453-459.

Bazant, Z.P and Feng-Bao Lin, [1988], "Non-local yield limit degradation", *Int. J. Num. Meth. Engng.*, 26, pp. 1805-1823.

Bazant, Z.P and G. Pijaudier-Cabot, [1987], "Modelling of distributed damage of non-local continuum with local strain", In *Numerical Methods in Fracture Mechanics, Proceedings of the 4th. International Conference held at San Antonio, Texas, USA*, A.R Luxmoore, D.R. Owen, Y.P.S Rajapakse and M.F Kanninen, Editors, pp. 411-432.

Bazant, Z.P and G. Pijaudier-Cabot, [1988], "Non-local continuum damage, localization instability and convergence", *J. Applied Mechanics*, **55**, pp. 287-293.

Belytschko, T., J. Fish, and B.E Englemann, [1988], "A finite element with embedded localization zones", *Comp. Meth. in Appl. Mech. and Eng.*, **70**, pp. 59-89.

Bicanic, N., E. Pramono, S. Sture and K.J William, [1985], "On numerical prediction of concrete fracture localization", *Proceedings of the NUMETA Conference*, Ed. J. Middleton and G.N Pande, Balkema, Rotterdam, pp. 385-391.

Biot, M.A., [1941], "General theory of three dimensional consolidation", *Journal of Applied Physics*, **12**, pp. 155-164..

Bishop, A.S., G.E. Green, V.K Garga, A. Andersen, and J.D Brown, [1971], "A new ring-shear apparatus and its application to the measurement of residual strength", *Geotechnique*, **21**, No. 4, pp. 273-328.

Boulon, M., and C. Plytas, [1986], "Soil structure directionally dependent interface constitutive equation application to the prediction of shaft friction along piles", In

2nd. Int. Symp. on Num. Models in Geom., ed. G.N Pande and W.F Van Impe, M. Jackson & Sons, Cornwall, England, pp. 43-54.

Burridge, P. B [1987], *Failure of Slopes*, Ph. D thesis, California Institute of Technology, Pasadena, California, USA.

Chaboche, J.L., [1981], "Continuous damage mechanics—A tool to describe phenomena before crack initiation", *Nucl. Eng. Des.*, 64, pp. 233-247.

Chan, D.H.K, [1985], *Finite Element Analysis of Strain-Softening Material*, Ph.D thesis, University of Alberta, Edmonton, Alberta.

Chazy, C., and P. Habib, [1961], "Les piles du quai de Floride", *5ème. Congrès International de Mécanique des Sols*, Paris, Com. 6/27, 669.

Coulomb, C.A., [1773], "Essai sur une application des règles de maximis et minimis à quelques problèmes de statique relatifs a l'architecture", *Mém. Académie Royale des Sciences*, Paris, **3**, p.38.

Eringen, A.C., and D.G.B Edelen, [1972], "On non local elasticity"; *International Journal of Engineering Science*, **10**, pp. 233-248.

Goodman, R.E., R.L Taylor and T.L Brekka, [1968], "A model for the mechanics of jointed rocks", *Journal of the Soil Mechanics and Foundation Engineering Division, ASCE*, **94**, SM3, pp.637-659.

Hadamard, J., [1903], "Leçons sur la propagation des ondes et les équations de l'hydrodynamique", Paris.

Hansen, B., [1958], "Lines ruptures regarded as narrow rupture zones, basic equations based on kinematic considerations", *Proceedings of Conference on Earth Pressure Problems*, Brussels, Belgium, pp. 39-51.

Hill, R., [1958], "A general theory of uniqueness and stability in elastic-plastic solids"; *Journal of the Mechanics Physics and Solids*, **6**, pp. 236-249.

Hill, R., [1962a], "Acceleration waves in solids"; *Journal of the Mechanics Physics and Solids*, **10**, pp. 1-16.

Hill, R., [1962b], "Constitutive laws and waves in rigid-plastic solids"; *Journal of the Mechanics Physics and Solids*, **10**, pp. 89-98.

Hoeg, K., [1972], "Finite element analysis of strain softening clay", *Journal of the Soil Mechanics and Foundation Engineering Division, ASCE*, **98**, SM1, pp. 43-58.

Hungerford, T.W., [1964], *Algebra*, Springer-Verlag, New-York.

Ichikawa, Y., T. Kyoya, and T. Kawamoto, [1985], "Incremental theory of plasticity for rocks", *Proceedings of the 5th. International Conference on Numerical Methods in Geomechanics*, T. Kawamoto and Y. Ichikawa, Editors, pp. 451-462.

Kroner, E., [1967], "Elasticity theory of materials with long range cohesive forces", *International Journal of Solid and Structures*, **3**, pp. 731-742.

Lade, P., R. Nelson, and M. Ito, [1987], "Non-associated flow and stability of granular materials", *Journal of Engineering Mechanics, ASCE*, **113**, No. 9, pp. 1302-1318.

Leroy, Y., A. Needleman, and M. Ortiz, [1988], "An overview of finite element methods for the analysis of strain localization", In Cracking and Damage: Strain localization and size effect", Ed. J. Mazars and Z.P Bazant, Elsevier Applied Science, pp. 269-294.

Lo, K.Y., and C.F Lee, [1973], "Stress analysis and strain softening materials", *Geotechnique*, **23**, No. 1, pp. 1-11.

Malvern, L.E., [1969], *Introduction to the Mechanics of a Continuous Medium*, Prentice-Hall, New-Jersey.

Mandel, J., [1966], "Conditions de stabilité et postulat de Drucker"; *Proceedings of the IUTAM Conference on Rheology on Soil Mechanics*, J. Kravtchenko and P. Sirieys, Ed. Springer-Verlag.

Melan, E., [1938] "Zur Plastizitat des Zaumlichen Kontinuums", *Ingenieur-Archiv*, **9**, pp.116-126.

Morgenstern, N.R., and J.S Tchalenko, [1967], "Microscopic structures in kaolin subjected to direct shear", *Geotechnique*, **17**, pp. 309-328

Muhlhaus, H.B., Vardoulakis, I., [1987], "The thickness of shear bands in granular materials", *Geotechnique*, **37**, No. 3 pp. 271-283.

Nayak, G.C., and O.C Zienkiewicz, [1972], "Elasto-plastic stress analysis: A generalization of various constitutive relations inducing strain-softening", *Int. J. Num. Meth. Engng.*, **5**, pp. 113-135.

Needleman, A., [1987], "Material rate dependence and mesh sensitivity in localization problems", *Computer Methods in Applied Mechanics and Engineering*, **67**, pp.68-85.

Ortiz, M., Y. Leroy and A. Needleman, [1987], "A finite element method for localized failure analysis", *Comp. Meth. in Appl. Mech. and Engng.*, **61**, pp. 189-214.

Peck, R.B., [1967], "Stability of natural slopes", *Journal of the Soil Mechanics and Foundation Engineering Division, ASCE*, **93**, SM4, pp. 403-417.

Pietruszczak, S.T., and Z. Mroz, [1981], "Finite element analysis of deformation of strain softening materials", *Int. J. Num. Meth. Engng.*, **10**, No. 17, pp. 327-334.

Pietruszczak, S.T., and D.F.E Stolle, [1987], "Deformation of strain-softening materials, Part II: Modelling of strain softening response", *Computers and Geotechnics*, **4**, pp. 109-123.

Prevost, J.H., and K. Hoeg, [1975a], "Effective stress-strain-strength model for soils", *Journal of the Geotechnical Engineering Division, GT3, ASCE*, pp. 259-278.

Prevost, J.H., and K. Hoeg, [1975b], "Soil mechanics and plasticity analysis of strain softening", *Geotechnique*, **25**, No. 2, pp. 279-297.

Rankine, W.J.M., [1857], "On the stability of loose earth", *Phil. Trans. Roy. Soc.*, London, **147**, Part 1, pp. 9-27.

Read, H.E and G.P Hegemier, [1984], "Strain softening of rock, soil and concrete—a review article", *Mechanics of Materials*, **3**, No. 4, pp. 271-294.

Rice, J.R., [1976], "The localization of plastic deformation", In *Theoretical and Applied Mechanics*, Ed. W.T Koiter, North-Holland, Amsterdam, pp. 207-220.

Roscoe, K.H., [1970], "The influence of strains in soil mechanics", Tenth Rankine Lecture, *Geotechnique*, **20**, No. 2, pp. 129-170.

Rosso, R., [1976], "A comparison of joint stiffness measurements in direct shear, triaxial and in-situ", *International J. Rock. Mech. Min. Sci. and Geomech. Abstr.*, **13**, pp. 167-172.

Rowe, P.W., [1962], "The stress dilatancy relation for static equilibrium of an assembly of particles in contact.", *Proceedings of the Royal Society, Series A*, **269**, pp. 500-527.

Rudnicki, J.W and J.R Rice,.[1975], "Conditions for the localization of deformation in pressure sensitive dilatant material", *J. Mech. Phys. Solids*, **23**, pp. 371-394.

Rudnicki, J.W., [1977], "The inception of faulting in a rock mass with a weakened zone", *Journal of Geophysical Research*, 82, No. 5, pp. 844-854.

Sandler, I and J. Wright, [1984], "Summary of strain softening", *Theoretical foundations for large scale computations of non-linear material behaviour*, DARPA-NSF workshop, Ed. S. Nemat-Nasser, North Western University.

Scarpelli, G., and D.M Wood, [1982], "Experimental observations of shear band pattern in direct shear tests", *IUTAM Symposium on Deformation and Failure of Granular Materials*, Delft, pp. 473-484.

Schreyer, H.L, Z. Chen, [1986], "One-Dimensional softening with localization", *ASME Journal of Applied Mechanics*, **53**, No. 4, pp 791-797.

Simo, J.C and R.L Taylor, [1985], "Consistent tangent operators for rate-independent elasto-plasticity", *Comp. Meth. in Appl. Mech. and Eng.*, **48**, pp.101-118.

Simo, J.C., [1988], "Strain softening and dissipation: A unification of approaches", In Cracking and Damage: Strain localization and size effect", Ed. J. Mazars and Z.P Bazant, Elsevier Applied Science, pp. 440-461.

Skempton, A.W., [1964], "Long-term stability of clay slopes", *Geotechnique*, **14**, N0. 2, pp. 77-101.

Sokolovski, V.V., [1965], *Statics of Granular Media*, London, Pergamon.

Tanaka, T., Kawamoto, O., [1989], "Plastic collapse analysis of slopes of strain softening materials", *Proceedings of the 3rd. International Symposium on Numerical Models in Geomechanics [NUMOG III]*, Ed. S. Pietruszczak and G.N Pande, Elsevier Applied Science, pp.667-674.

Tatsuoka, F., S. Nakamura, C.C Huang and K. Tani, [1990], "Strength anisotropy and shear band direction in plane strain tests of sand", *Soils and Foundations*, **30**, No. 1, pp. 35-54.

Terzaghi, K., [1923], "Die Berechnung der Durchlassig Keitsziffer des Tones aus dem Verlauf der Hydrodynamishen Spannungserscheinungen", *Sitzber. Akad. Wiss. Wien*, **132**, 125.

Thomas, T.Y., [1961], *Plastic Flow and Fracture in Solids*, Academic Press, New York.

Triantafyllidis, N., and E.C. Aifantis, [1986], "A gradient approach to localization of deformation, I: Hyperelastic Materials", *Journal of Elasticity*, **16**, pp. 225-237.

Truesdell, C. and R. Toupin, [1960], *The Classical Field Theories of Mechanics*, Handbuch der Physik, vol III/1, Springer.

Vardoulakis, I., [1979], "Bifurcation analysis of the triaxial test on sand samples", *Acta Mechanica*, **32**, pp. 35-54.

Vardoulakis, I., [1980], "Shear band inclination and shear modulus of sands in biaxial tests", *Int. J. Num. Anal. Meth. in Geomechanics*, **4**, pp. 103-119.

Vardoulakis, I., M. Goldshieder, and G. Gudehus, [1978], "Formation of shear bands in sand bodies as a bifurcation problem", *Int. J. Num. Anal. Meth. in Geomechanics*, **2**, pp. 99-128.

Vermeer, P.A., [1982], " A simple shear band analysis using compliances", *IUTAM Symposium on Deformation and Failure of Granular Materials*, Delft, pp. 493-499.

Yatomi, C., A, Yashima, A. Iizuka, and I. Sano, [1989], "General theory of shear bands formation by a non-coaxial Cam-Clay model", *Soils and Foundations*, **29**, No. 3, pp. 41-53.

Yoshimi, Y., and T. Kishida, [1981], "A ring torsion apparatus for evaluation of friction between soil and metal surfaces", *Geotechnical Testing Journal*, GTJODJ, **4**, No. 4, pp.145-152.

Zienkiewicz, O.C and K. Morgan, [1982], *Finite Elements and Approximation*, John Wiley and sons, New-York.

Zienkiewicz, O.C and R.L Taylor, [1989], *The Finite Element Method*, Fourth Edition, Volume 1, Mc-Graw-Hill, New-York.

Appendix A

Derivation of Flow and Deformation Equations

A.1. Theory of mixtures

Consider a 2-phase medium in which the 2 phases interact so that their behaviours give an average response. Let ρ_s and ρ_f represent respectively the density of the solid and fluid phases, $\rho^{(s)}$ and $\rho^{(f)}$ the corresponding relative densities (the ones we actually measure experimentally). Thus, the total density ρ can be defined as the sum of the densities of each constituent phase, i.e.

$$\rho = \rho^{(s)} + \rho^{(f)}, \tag{A.1}$$

$$\rho^{(s)} = \frac{dM_s}{dV} = \frac{dM_s}{dV_s}\frac{dV_s}{dV} = \frac{dM_s}{dV_s}\frac{dV - dV_f}{dV} = (1-n)\rho_s \tag{A.2}$$

$$\rho^{(f)} = \frac{dM_f}{dV} = \frac{dM_f}{dV_f}\frac{dV_f}{dV} = n\rho_f \tag{A.3}$$

Each constituent phase has to satisfy the mass balance equation, i.e.

$$\dot{\rho}^{(\alpha)} + \rho^{(\alpha)} \frac{\partial v_i^{(\alpha)}}{\partial x_i} = 0, \tag{A.4}$$

in which (α) stands for the fluid phase and the superimposed dot represents the material derivative. This mass balance or continuity condition written for the solid phase becomes:

$$\frac{\partial (1-n)\rho_s}{\partial t} + \frac{\partial (1-n)\rho_s v_i^{(s)}}{\partial x_i} = 0. \tag{A.5}$$

Expanding Eq. (A.5) and using the operator $\frac{\mathrm{d}(.)}{\mathrm{d}t} = \frac{\partial(.)}{\partial t} + v_i \frac{\partial(.)}{\partial x_i}$ the following is obtained:

$$\frac{dn}{dt} = \frac{(1-n)}{\rho_s}\left[\frac{d\rho_s}{dt} + \frac{\partial v_i^{(s)}}{\partial x_i}\right], \text{ for} \rho_s \neq 0. \tag{A.6}$$

Let's define a bulk relative fluid velocity q_i as

$$v_i = n(v_i^{(f)} - v_i^{(s)}). \tag{A.7}$$

The continuity equation for the fluid phase can be written as

$$\frac{\partial (n\rho_f)}{\partial t} + \frac{\partial (n\rho_f v_i^{(f)})}{\partial x_i} = 0. \tag{A.8}$$

Using Eq. (A.7) to eliminate $v_i^{(f)}$ and with the aid of Eq. (A.6), one gets after some algebra

$$-\frac{1}{\rho_f}\frac{\partial (\rho_f v_i)}{\partial x_i} = (1-n)\frac{1}{\rho_s}\frac{d\rho_s}{dt} + n\frac{1}{\rho_f}\frac{d\rho_f}{dt} + \frac{\partial v_i^{(s)}}{\partial x_i} \tag{A.9}$$

But

$$\frac{\partial v_i^{(s)}}{\partial x_i} = \frac{\partial}{\partial x_i}\frac{du_i}{dt} = \frac{d}{dt}\left(\frac{\partial u_i}{\partial x_i}\right) = \dot{\varepsilon}_{ii}. \tag{A.10}$$

Darcean flow can be written as

$$v_i = -k_{ij}\left[\frac{\partial \pi}{\partial x_j} + \rho_f g_j\right], \tag{A.11}$$

in which π is the pore fluid pressure and g_j is the j th. component of gravity. When Eq. (A.11) is substituted into (A.9), one gets:

$$\frac{1}{\rho_f}\frac{\partial}{\partial x_i}\rho_f\left[k_{ij}\frac{\partial \pi}{\partial x_j} + \rho_f g_j\right] = (1-n)\frac{1}{\rho_s}\frac{d\rho_s}{dt} + n\frac{1}{\rho_f}\frac{d\rho_f}{dt} + \dot{\varepsilon}_{ii}. \tag{A.12}$$

For incompressible solid and fluid phases, Eq. (A.13) obviously reverts to the following well-known form:

$$\frac{\partial}{\partial x_i}\left[k_{ij}\frac{\partial \pi}{\partial x_j} + \rho_f g_j\right] - \dot{\varepsilon}_{ii} = 0. \tag{A.13}$$

A.2. Flow equations

• Strong form

Consider the fluid flow described in Chapter 4 for a discontinuous medium as previously illustrated in Figure 4.2. The strong form (**S**) or the classical statement of the flow problem is mathematically represented by physical laws that govern the phenomenon , i.e.

• ***Mass conservation:***

$$v_{i,i} + \dot{u}_{i,i} = 0. \tag{A.14}$$

• ***Darcean flow:***

$$v_i = -k_{ij}(\pi_{,j} + \gamma_j). \tag{A.15}$$

• ***Boundary conditions:***

$$\pi(\mathbf{x}) = \overline{\pi}(\mathbf{x}) \text{ on } \Gamma_\pi, \tag{A.16}$$

$$\overline{q} = v_i n_i \text{ on } \Gamma_q, \tag{A.17}$$

$$\left[v_i^{(1)} - v_i^{(2)}\right] n_i^{(1)} = -\dot{g}_i n_i^{(1)} + \overline{q}_{sb} \text{ on } \Gamma_{sb}. \tag{A.18}$$

If poré fluids are principal unknowns, then the equation of mass balance combined with Darcean flow becomes:

$$\left[k_{ij}(\pi_{,j} + \gamma_j)\right]_{,i} - \dot{u}_{i,i} = 0 \text{ in } \Omega_1 \cup \Omega_2, \tag{A.19}$$

$$\pi(\mathbf{x}) = \overline{\pi}(\mathbf{x}) \text{ on } \Gamma_\pi, \tag{A.20}$$

$$-k_{ij}(\pi_{,j} + \gamma_j) n_i = \overline{q}, \tag{A.21}$$

$$\left[k_{ij}^{(2)}(\pi_{,j}^{(2)} + \gamma_j) - k_{ij}^{(1)}(\pi_{,j}^{(1)} + \gamma_j)\right] n_i^{(1)} = -\dot{g}_i n_i^{(1)} + \overline{q}_{sb} \text{ on } \Gamma_{sb}. \tag{A.22}$$

• **Weak form : Problem statement:**

The weak form (**W**) or the variational counterpart of (**S**) involves the following: find $\pi(\mathbf{x})$ such that Eq. (A.19) is satisfied everywhere inside $\Omega = \Omega_1 \cup \Omega_2$ with boundary conditions specified by Eqs. (A.20) to (A.22). Note that the pore fluid π is discontinuous across the shear band interface.

Variational statement:

A Galerkin approximation of the problem is obtained by posing the variational problem on a finite dimensional subspace $\mathcal{H}$ of the space of hydraulically admissible functions, i.e. those which satisfy the homogeneous essential boundary conditions and are smooth enough. In particular, $\mathcal{H}$ is defined as

$$\mathcal{H} = \left\{ \pi^* = \pi^*(\mathbf{x}) / \overline{\pi}^* = 0 \text{ on } \Gamma_\pi \right\}. \tag{A.23}$$

The differential equation in (A.6) with associated boundary conditions can be cast in an integral form by multiplying it by the admissible pore fluid field $\pi^*(\mathbf{x})$ in order to obtain a weak form. By virtue of the weighted residual method which aims at minimizing the error on an average weighted sense,

$$\int_\Omega \left[k_{ij}(\pi_{,j} + \gamma_j) \right]_{,i} \delta\pi^* \, d\Omega + \int_\Omega \dot{u}_{i,i} \, \delta\pi^* \, d\Omega = 0. \tag{A.24}$$

Noting that

$$\left[k_{ij}(\pi_{,j} + \gamma_j) \right]_{,i} \delta\pi^* = \left[k_{ij}(\pi_{,j} + \gamma_j)\delta\pi^* \right]_{,i} - k_{ij}(\pi_{,j} + \gamma_j)\delta\pi^*_{,i}, \tag{A.25}$$

integration by parts yields:

$$\int_\Omega k_{ij}(\pi_{,j} + \gamma_j)\delta\pi^*_{,i} \, d\Omega + \int_\Omega \dot{u}_{i,i} \, \delta\pi^* \, d\Omega = \int_{\Gamma_q \cup \Gamma_{sb}} k_{ij}(\pi_{,j} + \gamma_j) n_i \, d\Gamma. \tag{A.26}$$

This boundary integral on the right hand side of the above equation can be broken down into the following components, with the aid of Eq.(A.15)

$$-\int_{\Gamma_q} v_i n_i \, \delta\pi^* \, d\Gamma + \int_{\Gamma_{sb}} \left[v_i^{(1)} n_i^{(1)} + v_i^{(2)} n_i^{(2)} \right] \delta\pi^* \, d\Gamma. \tag{A.27}$$

Considering $n_i^{(1)} = -n_i^{(2)}$, the above integral becomes

$$-\int_{\Gamma_q} \bar{q} \, \delta\pi^* \, d\Gamma - \int_{\Gamma_{sb}} \left[-g_i n_i^{(1)} + \bar{q}_{sb} \right] \delta\pi^* \, d\Gamma, \tag{A.28}$$

which yields boundary conditions (A.17) and (A.18). The final form of the Galerkin expression emerges as:

$$\int_\Omega k_{ij} \pi_{,j} \, \delta\pi^*_{,i} \, d\Omega + \int_\Omega \dot{u}_{i,i} \, \delta\pi^* \, d\Omega - \int_{\Gamma_{sb}} \dot{g}_i n_i^{(1)} \, d\Gamma = -\int_\Omega k_{ij} \gamma_j \, \delta\pi^*_{,i} \, d\Omega - \int_{\Gamma_q} \bar{q} \, \delta\pi^* \, d\Gamma - \int_{\Gamma_{sb}} \bar{q}_{sb} \, \delta\pi^* \, d\Gamma. \tag{A.29}$$

Appendix B

Numerical Implementation

B.1. Evaluation of composite element stiffness matrix

Consider the expanded form of the stiffness matrix as obtained from the discretization of the variational principle in Chapter 4. Fig. B.1. shows the typical size of the stiffness matrix for a QD4 type of element and the different partitions which have to be computed during a numerical analysis.

Explicit forms of the compatibility matrices $\mathbf{B}^{(\alpha)}$, $\mathbf{B}^{(\beta)}$, constitutive tensors $\mathbf{L}$ and η as well as the geometrical location of the discontinuity are required for the numerical integration of the various stiffnesses in the composite stiffness matrix. In plane strain conditions, the compatibility matrix $\mathbf{B}^{(\alpha)}$ is traditionally given by

$$\left[\mathbf{B}_i^{(\alpha)}\right]^{(e)} = \begin{bmatrix} \left(\dfrac{\partial N_i^{(\alpha)}}{\partial x}\right)^{(e)} & 0 \\ 0 & \left(\dfrac{\partial N_i^{(\alpha)}}{\partial y}\right)^{(e)} \\ \left(\dfrac{\partial N_i^{(\alpha)}}{\partial y}\right)^{(e)} & \left(\dfrac{\partial N_i^{(\alpha)}}{\partial x}\right)^{(e)} \end{bmatrix} \text{ with } i = 1, \text{ node}, \tag{B.1}$$

in which node takes the value of 4 for a quadrilateral element and 3 for a constant strain triangular element.

If one envisions a linear variation of slip displacement along the shear band by having two localized nodes, the compatibilty matrix $\mathbf{B}^{(\beta)}$ for the discontinuity is

$$\left[\mathbf{B}_i^{(\beta)}\right]^{(e)} = \begin{bmatrix} \left(\dfrac{\partial N_i^{(\beta)}}{\partial x}\right)^{(e)} & 0 \\ 0 & \left(\dfrac{\partial N_i^{(\beta)}}{\partial y}\right)^{(e)} \\ \left(\dfrac{\partial N_i^{(\beta)}}{\partial y}\right)^{(e)} & \left(\dfrac{\partial N_i^{(\beta)}}{\partial x}\right)^{(e)} \end{bmatrix} \quad \text{for which } i = 1,\ 2. \tag{B.2}$$

The *discontinuous* shape functions $N_i^{(\beta)}$ whose derivatives exist on either side of the discontinuity front were defined in Chapter 4. The form of the shape matrix $\left(\mathbf{N}^{(\beta)}\right)^e$ which is suitable for a numerical implementation is

$$\left(\mathbf{N}^{(\beta)}\right)^e = \begin{bmatrix} N_1^{(\beta)} & 0 & N_2^{(\beta)} & 0 \\ 0 & N_1^{(\beta)} & 0 & N_2^{(\beta)} \end{bmatrix}. \tag{B.3}$$

For plane strain elasticity, the constitutive tensor $\mathbf{L}$ and $\boldsymbol{\eta}$ are simply

$$\mathbf{L} = \frac{E}{(1+\nu)(1-2\nu)} \begin{bmatrix} (1-\nu) & \nu & 0 \\ \nu & (1-\nu) & 0 \\ 0 & 0 & \dfrac{(1-\nu)}{2} \end{bmatrix}; \tag{B.4}$$

$$\boldsymbol{\eta}_{\alpha\beta} = \begin{bmatrix} \eta_{\alpha\beta} & \eta_{\alpha n} \\ \eta_{n\beta} & \eta_{nn} \end{bmatrix}. \tag{B.5}$$

In a more general case, the tensors $\mathbf{L}$ and η would take the classical elasto-plastic form similar to that presented in Eq. (3.11).

B.2. Quadrature rule for element stiffness integration

A numerical quadrature scheme that accommodates for the proposed displacement and strain fields must be considered in order to achieve accurate results and handle the effect of the localized zone as well. A standard quadrature scheme, say 2x2 Gauss integration will not capture the presence of the jump inside the element provided a large number of quadrature points is used.

Consider the QD4 element with the embedded shear band as shown in Fig. B.2. The sought effect is to have strains localized along the shear band and non-localized strains in regions outside the band. A normal 2x2 Gauss integration scheme will result in the smearing of the displacement field jump over the element so that a bilinear distribution similar to the classical Q4 element will be obtained rather than a distribution with an intrinsic jump.

The integration scheme adopted herein guarantees accuracy in capturing the jump inside the element by using standard numerical integration over separate domains demarcated by the shear band boundary, see Fig. B.3. This procedure inevitably introduces a large number of integration points, i.e. 10 in all for a QD4 element (4 over each domain adjacent to the shear band and 2 other ones along the shear band itself).

A typical integral over the area of the element for a discontinuous function $f(\mathbf{x})$ is given by

$$I = \int_{\Omega} f(\mathbf{x})\, d\Omega. \tag{B.6}$$

Since $f(\mathbf{x})$ takes up different values depending on whether $\mathbf{x}$ is in region Ω^{e+} or Ω^{e-}, the integral has to be discretized over each separate domain, i.e.

$$I = \sum_{i=1}^{NGAUS}\sum_{j=1}^{NGAUS} f^{+}(r_i,s_j)(\det J)_{ij}(\det J^{*})_{ij}\, w_i w_j + \sum_{i=1}^{NGAUS}\sum_{j=1}^{NGAUS} f^{-}(r_i,s_j)(\det J)_{ij}(\det J^{*})_{ij}\, w_i w_j. \tag{B.7}$$

(ξ_i,η_j) are the coordinates in the local reference system, (r_i,s_j) the coordinates in the sub-local reference system, J the Jacobian of the transformation between the local and global systems, J^* the Jacobian of the transformation between the sub-local and local coordinates and w_i the weights, see Fig. B.3 for details.

The different constituent stiffnesses of the composite matrix given in Fig. B.3 are evaluated on the basis of the foregoing scheme.

- **Bulk stiffness** $\mathbf{K}^{(e)}_{\Omega\Omega}$

$$\begin{aligned}\mathbf{K}^{(e)}_{\Omega\Omega} &= \int_{\Omega^e} \mathbf{B}^{(\alpha)T}(x,y):\mathbf{L}(x,y):\mathbf{B}^{(\alpha)}(x,y)\, dx\, dy \\ &= \int_{\Omega^{e+}} \mathbf{B}^{(\alpha)+T}(\xi,\eta):\mathbf{L}(\xi,\eta):\mathbf{B}^{(\alpha)+}(\xi,\eta)\, \det J\, d\xi\, d\eta \\ &\quad + \int_{\Omega^{e-}} \mathbf{B}^{(\alpha)-T}(\xi,\eta):\mathbf{L}(\xi,\eta):\mathbf{B}^{(\alpha)-}(\xi,\eta)\, \det J\, d\xi\, d\eta\end{aligned} \tag{B.8}$$

When integrated in the local system,

$$\mathbf{K}^{(e)}_{\Omega\Omega} = \sum_i\sum_j \mathbf{B}^{(\alpha)T}(\xi_i,\eta_j):\mathbf{L}(\xi_i,\eta_j):\mathbf{B}^{(\alpha)}(\xi_i,\eta_j)(\det J)_{ij} w_i w_j. \tag{B.9}$$

Note that $\mathbf{B}^{(\alpha)+}$ and $\mathbf{B}^{(\alpha)-}$ are the same and the integration may be accomplished in the (ξ,η) space.

- **Bulk - shear band interaction stiffnesses $\mathbf{K}_{\Omega S}^{(e)}$ and $\mathbf{K}_{S\Omega}^{(e)}$**

The numerical integration of stiffness terms $\mathbf{K}_{\Omega S}^{(e)}$ and $\mathbf{K}_{S\Omega}^{(e)}$ is performed in the same fashion as in Eq. (B.6). It is noted that the symmetry $\mathbf{K}_{\Omega S}^{(e)} = \mathbf{K}_{S\Omega}^{(e)^T}$ is destroyed as soon as $\mathbf{L}$ ceases to be symmetric.

$$\mathbf{K}_{\Omega S}^{(e)} = \sum_i \sum_j \mathbf{B}^{(\alpha)+T}(r_i,s_j):\mathbf{L}(r_i,s_j):\mathbf{B}^{(\beta)+}(r_i,s_j)(\det J)_{ij}(\det J^{*+})_{ij} w_i w_j$$

$$+ \sum_i \sum_j \mathbf{B}^{(\alpha)-T}(r_i,s_j):\mathbf{L}(r_i,s_j):\mathbf{B}^{(\beta)-}(r_i,s_j)(\det J)_{ij}(\det J^{*-})_{ij} w_i w_j,$$

$\forall (r_i,s_j) \in \Omega^{e+}$ or Ω^{e-}.

(B.10)

- **Global shear band stiffness $\mathbf{K}_{SS}^{(e)}$**

$$\mathbf{K}_{SS}^{(e)} = \sum_i \sum_j \mathbf{B}^{(\beta)+T}(r_i,s_j):\mathbf{L}(r_i,s_j):\mathbf{B}^{(\beta)+}(r_i,s_j)(\det J)_{ij}(\det J^{*+})_{ij} w_i w_j$$

$$+ \sum_i \sum_j \mathbf{B}^{(\beta)-T}(r_i,s_j):\mathbf{L}(r_i,s_j):\mathbf{B}^{(\beta)-}(r_i,s_j)(\det J)_{ij}(\det J^{*-})_{ij} w_i w_j$$

$$+ \int_{\Gamma^e} \mathbf{N}^{(\beta)T}[\eta]_{n-} \, d\Gamma.$$

(B.11)

B.3. Calculation of cartesian derivatives of shape functions

The dual transformation described in the previous section, i.e.

$$(x,y) \xrightarrow{J} (\xi,\eta) \xrightarrow{J^*} (r,s)$$

requires the evaluation of two Jacobians which are

$$J = \begin{bmatrix} \frac{\partial x}{\partial \xi} & \frac{\partial y}{\partial \xi} \\ \frac{\partial x}{\partial \eta} & \frac{\partial y}{\partial \eta} \end{bmatrix} \quad , J^* = \begin{bmatrix} \frac{\partial \xi}{\partial r} & \frac{\partial \eta}{\partial r} \\ \frac{\partial \xi}{\partial s} & \frac{\partial \eta}{\partial s} \end{bmatrix} \tag{B.12}$$

The cartesian derivatives of the shape functions are calculated by multiplying the local derivatives by the appropriate Jacobian matrices. Typically in the local (ξ,η) reference axes

$$\frac{\partial N_i^{(j)}}{\partial x} = \frac{\partial N_i^{(j)}}{\partial \xi}\frac{\partial \xi}{\partial x} + \frac{\partial N_i^{(j)}}{\partial \eta}\frac{\partial \eta}{\partial x}, \tag{B.13}$$

$$\frac{\partial N_i^{(j)}}{\partial y} = \frac{\partial N_i^{(j)}}{\partial \xi}\frac{\partial \xi}{\partial y} + \frac{\partial N_i^{(j)}}{\partial \eta}\frac{\partial \eta}{\partial y}, \tag{B.14}$$

or

$$\begin{Bmatrix} \frac{\partial N_i^{(j)}}{\partial x}(\xi,\eta) \\ \frac{\partial N_i^{(j)}}{\partial y}(\xi,\eta) \end{Bmatrix} = \begin{bmatrix} \frac{\partial \xi}{\partial x} & \frac{\partial \eta}{\partial x} \\ \frac{\partial \xi}{\partial y} & \frac{\partial \eta}{\partial y} \end{bmatrix} \begin{Bmatrix} \frac{\partial N_i^{(j)}}{\partial \xi} \\ \frac{\partial N_i^{(j)}}{\partial \eta} \end{Bmatrix}, \tag{B.15}$$

in which $j = \alpha$ or β refers to continuous and discontinuous components respectively. The cartesian derivatives in the (r,s) space are obtained by evaluating the Jacobian and shape function derivatives at points $\xi(r,s)$ and $\eta(r,s)$, i.e.

$$\begin{Bmatrix} \dfrac{\partial N_i^{(j)}}{\partial x}(r,s) \\ \dfrac{\partial N_i^{(j)}}{\partial y}(r,s) \end{Bmatrix} = \begin{bmatrix} \dfrac{\partial \xi}{\partial x}(r,s) & \dfrac{\partial \eta}{\partial x}(r,s) \\ \dfrac{\partial \xi}{\partial y}(r,s) & \dfrac{\partial \eta}{\partial y}(r,s) \end{bmatrix} \begin{Bmatrix} \dfrac{\partial N_i^{(j)}}{\partial \xi}(\xi(r,s),\eta(r,s)) \\ \dfrac{\partial N_i^{(j)}}{\partial \eta}(\xi(r,s),\eta(r,s)) \end{Bmatrix}$$

$$= [J]^{-1}_{\xi(r,s),\eta(r,s)} \begin{Bmatrix} \dfrac{\partial N_i^{(j)}}{\partial \xi} \\ \dfrac{\partial N_i^{(j)}}{\partial \eta} \end{Bmatrix}. \qquad \text{(B.16)}$$

It is noted that J and J^* describe the geometry of the element and may be evaluated using different shape functions such that the transformation does not need to be isoparametric in the true sense. It would indeed be either sub-parametric, i.e the geometric mapping is of a lower degree basis or a subset of the interpolant for displacement, or super-parametric if the geometric map is of a higher order than the interpolant as in the case of a linear variation of slip displacements along a curved shear band.

B.4. Calculation of interface stiffness

Consider the geometrical representation of the shear band oriented in an arbitrary manner inside the element as shown in Fig. B.4. Call θ the inclination of the shear band axis with respect to the global x axis. The local coordinate system attached to the shear band are defined by (n,s).

Since during the discretization process, a linear variation of slip displacement $\mathbf{g}$ was prescribed within the element and along the discontinuity line Γ_s, i.e

$$\mathbf{g}(\xi) = \frac{(1-\xi)}{2}\overline{\mathbf{g}}_1 + \frac{(1+\xi)}{2}\overline{\mathbf{g}}_2, \quad \xi \in \Gamma_s, \qquad \text{(B.17)}$$

with $\overline{\mathbf{g}}_1$ and $\overline{\mathbf{g}}_2$ the slips vector at localized nodes 1 and 2 respectively. The incremental slip displacement vector in the *(n,s)* system anywhere along Γ_s becomes

$$\begin{Bmatrix} \Delta g_s \\ \Delta g_n \end{Bmatrix} = \frac{1}{2}\begin{bmatrix} (1-\xi) & 0 & (1+\xi) & 0 \\ 0 & (1-\xi) & 0 & (1+\xi) \end{bmatrix} \begin{Bmatrix} \Delta \overline{g}_{s1} \\ \Delta \overline{g}_{n1} \\ \Delta \overline{g}_{s2} \\ \Delta \overline{g}_{n2} \end{Bmatrix} \tag{B.18}$$

In compact form, the incremental slip displacements in the *(n,s)* axes is

$$\Delta \mathbf{g} = \mathbf{N}^{*} \Delta \overline{\mathbf{g}} \tag{B.19}$$

The interface stiffness term $\mathbf{K}^{*}_{ss}$ in the discretized FEM equations, see last term in Eq.(B.11), refers to the global axes *(x,y)* . Since the contact constitutive tensor $\boldsymbol{\eta}$ is expressed in *s-n* axes, it has to be pre and post multiplied by the appropriate transformation matrix **A** which is

$$\mathbf{A} = \begin{bmatrix} [\mathbf{a}] & [0] \\ [0] & [\mathbf{a}] \end{bmatrix} \tag{B.20}$$

with

$$[\mathbf{a}] = \begin{bmatrix} \cos\theta & \sin\theta \\ -\sin\theta & \cos\theta \end{bmatrix} \tag{B.21}$$

Since for a linear shear band, **A** remains constant, then the interface stiffness $\mathbf{K}^{*}_{ss\,(x\text{-}y)}$ in the *x-y* reference frame is simply

$$K^{*}_{ss(x-y)} = \int_{\Gamma^{*}} \mathbf{N}^{(\beta)T} : \boldsymbol{\eta} : \mathbf{N}^{(\beta)} \; d\Gamma = \mathbf{A}^{T}\left[\int_{\Gamma^{*}} \mathbf{N}^{*T} : \boldsymbol{\eta}_{(s-n)} : \mathbf{N}^{*} \, d\Gamma\right]\mathbf{A}. \qquad \text{(B.22)}$$

B.5. Evaluation of load vectors

The load terms in the discretized variational principle comprise two basic components, namely:

- **Load emanating from the continuous component**

$$\begin{aligned}\Delta \mathbf{f}_{\Omega} &= \int_{\Omega^{e}} \mathbf{N}^{(\alpha)T} \Delta \mathbf{f} \, d\Omega + \int_{\Gamma_{\sigma}^{e}} \mathbf{N}^{(\alpha)T} \Delta \overline{\mathbf{T}} \, d\Gamma \\ &= \sum_{i=1}^{NGAUS} \sum_{j=1}^{NGAUS} \mathbf{N}^{(\alpha)T}(\xi_i, \eta_j) \Delta \mathbf{f}(\xi_i, \eta_j) w_i w_j (\det J)_{ij} \\ &\quad + \sum_{j=1}^{NGAUS} \mathbf{N}^{(\alpha)T}(\xi_i) \Delta \overline{\mathbf{T}}(\xi_i) \left[\left(\frac{\partial N_j^{(\alpha)}}{\partial \xi} x_j\right)^2 + \left(\frac{\partial N_j^{(\alpha)}}{\partial \xi} y_j\right)^2\right]^{1/2} w_i .\end{aligned}$$

The computations involved in the above expression are straightforward since they do not include any discontinuous shape functions.

- **Load emanating from the discontinuous component**

$$\Delta \mathbf{f}_{s} = \int_{\Omega^{e}} \mathbf{N}^{(\beta)T} \Delta \mathbf{f} \; d\Omega + \int_{\Gamma_{\sigma}^{e}} \mathbf{N}^{(\beta)T} \Delta \overline{\mathbf{T}} \; d\Gamma .$$

The above load expression describes the discontinuous contribution term which has to be added to the boundary loads. It effectively connects the boundary to the discontinuity surface as long as the boundary is part of a shear band element.

The first contribution, i.e. the volume integral over the element domain is integrated by means of the quadrature rule introduced in Section B.2 and results in

$$\int_{\Omega^*} \mathbf{N}^{(\beta)^T} . \Delta \mathbf{f} \; d\Omega = \sum_i \sum_j \mathbf{N}^{(\beta)^+}(r_i, s_j)\, \Delta \mathbf{f}(r_i, s_j)(\det J^{*+})_{ij} w_i w_j$$

$$+ \sum_i \sum_j \mathbf{N}^{(\beta)^-}(r_i, s_j)\, \Delta \mathbf{f}(r_i, s_j)(\det J^{*-})_{ij} w_i w_j .$$

The second contribution which is a surface integral will have to be evaluated whenever the load is applied along an edge which is crossed by the shear band, see Fig. B.5. Accordingly,

$$\int_{\Gamma_\sigma^*} \mathbf{N}^{(\beta)^T} . \Delta \overline{\mathbf{T}} \; d\Gamma = \int_{\Gamma_\sigma^{*+}} \mathbf{N}^{(\beta)+^T} . \Delta \overline{\mathbf{T}} \; d\Gamma + \int_{\Gamma_\sigma^{*-}} \mathbf{N}^{(\beta)-^T} . \Delta \overline{\mathbf{T}} \; d\Gamma$$

$$= \sum_{i=1}^{NGAUS} \mathbf{N}^{\beta+}(r_i(\xi_p, \eta_p)) \Delta \overline{\mathbf{T}}(r_i) \left[\left(\frac{\partial N_j^*}{\partial \xi} x_j \right)^2 + \left(\frac{\partial N_j^*}{\partial \xi} y_j \right)^2 \right]^{1/2} w_i$$

$$+ \sum_{i=1}^{NGAUS} \mathbf{N}^{\beta-}(r_i(\xi_p, \eta_p)) \Delta \overline{\mathbf{T}}(r_i) \left[\left(\frac{\partial N_j^*}{\partial \xi} x_j \right)^2 + \left(\frac{\partial N_j^*}{\partial \xi} y_j \right)^2 \right]^{1/2} w_i ,$$

where N_j^* is either a linear or quadratic interpolation function for the mapping of (x,y) onto local coordinates ξ. x_i and y_j are the coordinates which define the boundary of the domains along the edge.

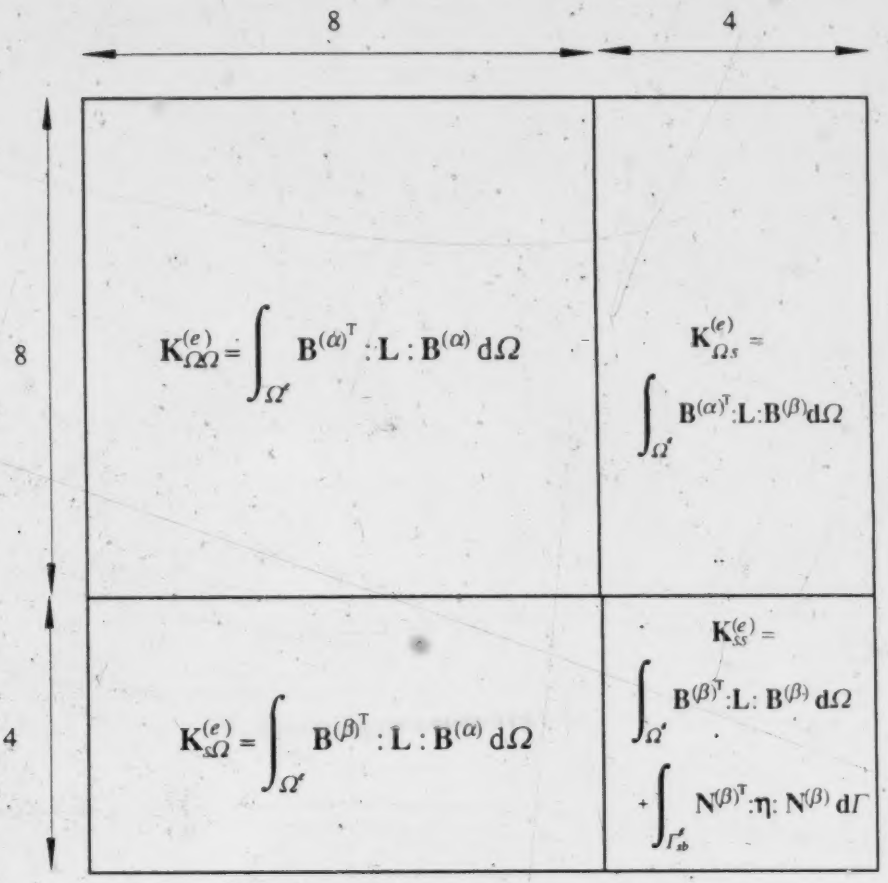
8
4
8
4
$\mathbf{K}^{(e)}_{\Omega\Omega} = \int_{\Omega'} \mathbf{B}^{(\alpha)^T} : \mathbf{L} : \mathbf{B}^{(\alpha)}\, d\Omega$
$\mathbf{K}^{(e)}_{\Omega s} = \int_{\Omega'} \mathbf{B}^{(\alpha)^T} : \mathbf{L} : \mathbf{B}^{(\beta)} d\Omega$
$\mathbf{K}^{(e)}_{s\Omega} = \int_{\Omega'} \mathbf{B}^{(\beta)^T} : \mathbf{L} : \mathbf{B}^{(\alpha)}\, d\Omega$
$\mathbf{K}^{(e)}_{ss} = \int_{\Omega'} \mathbf{B}^{(\beta)^T} : \mathbf{L} : \mathbf{B}^{(\beta)}\, d\Omega + \int_{\Gamma'_{sb}} \mathbf{N}^{(\beta)^T} : \boldsymbol{\eta} : \mathbf{N}^{(\beta)}\, d\Gamma$

Figure B.1 Structure of typical stiffness matrix for a shear band element

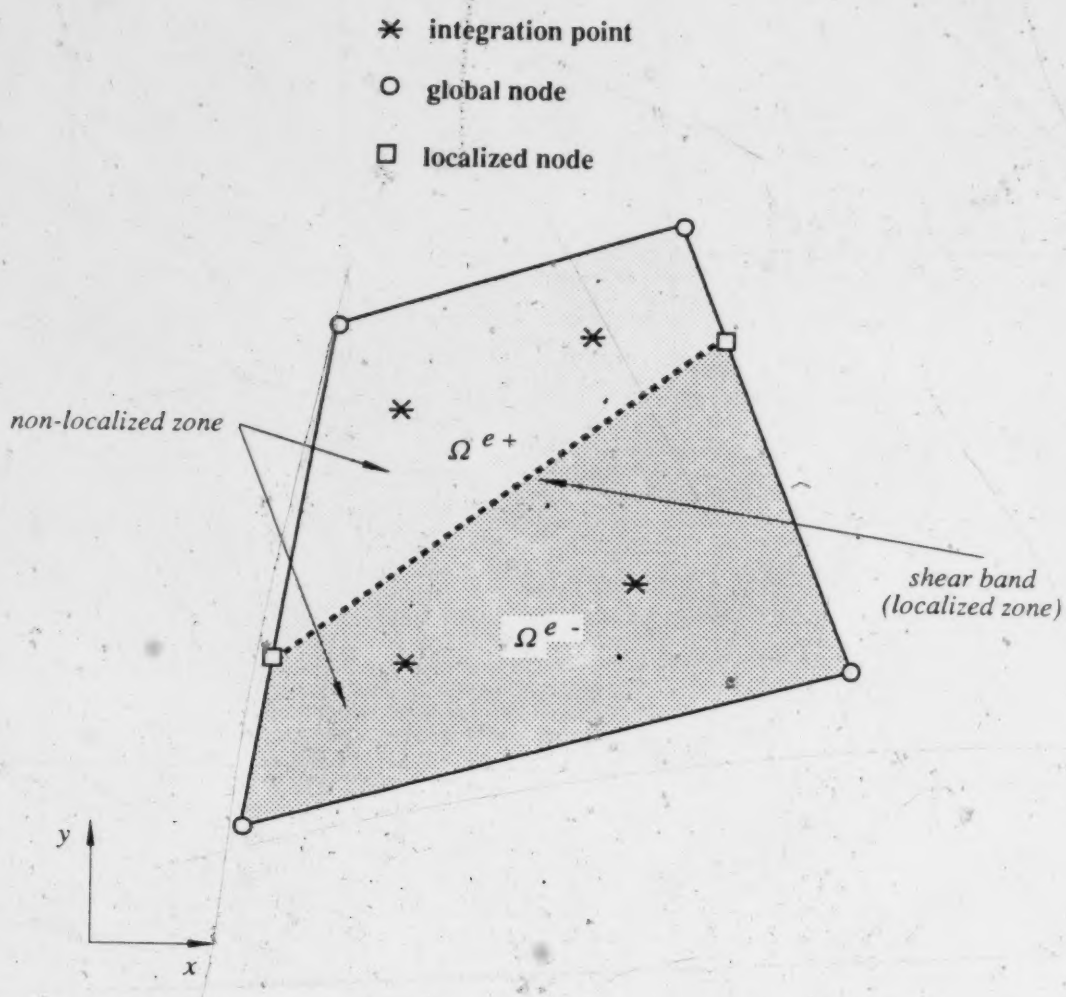

Figure B.2 Smearing effect for normal quadrature rule

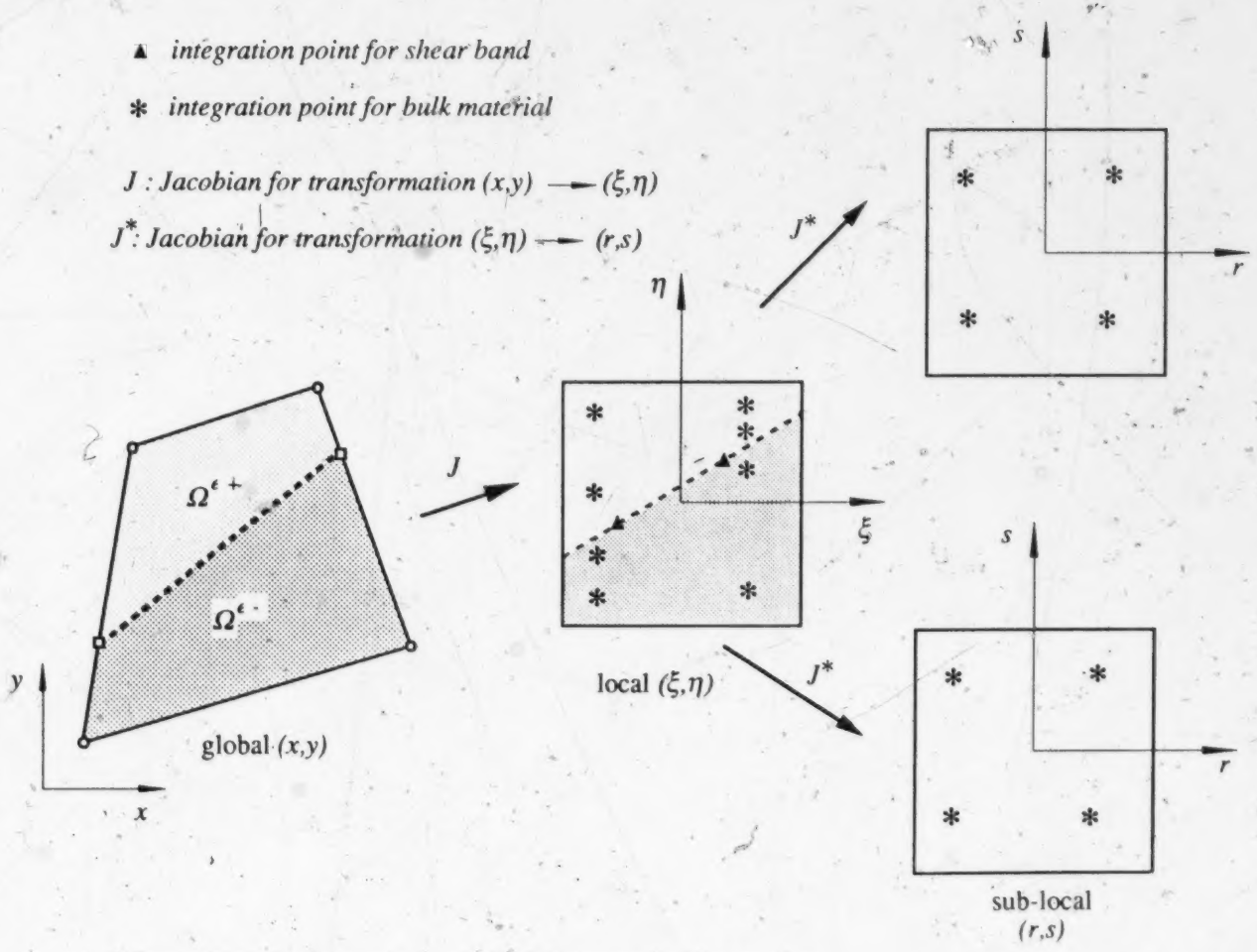

Figure B.3 Dual mapping technique for numerical integration

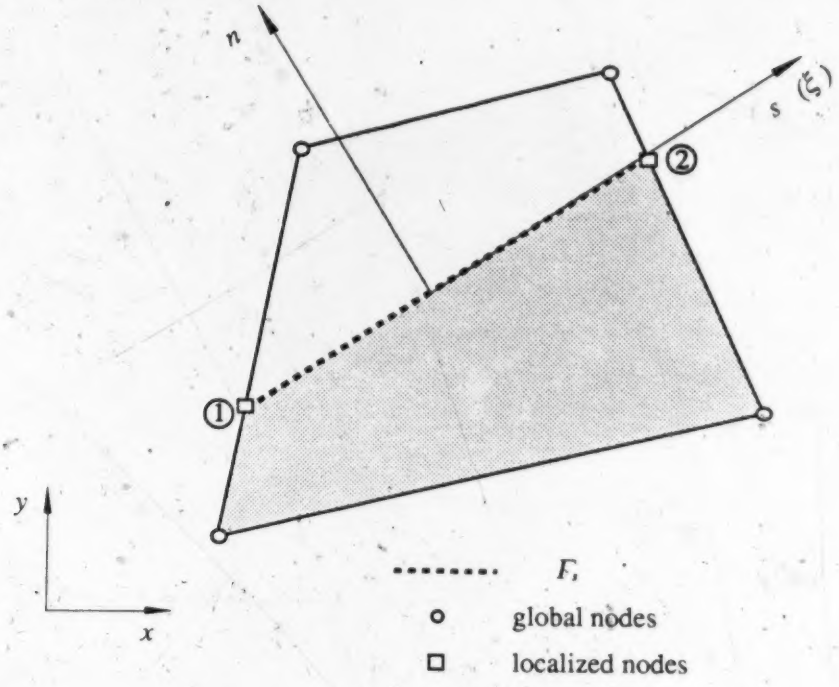

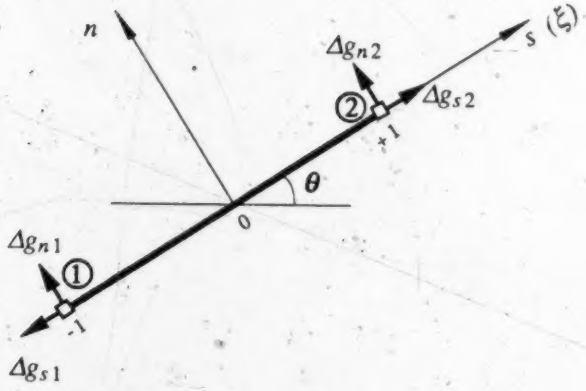

Figure B.4 Shear band geometry in global and local coordinate systems

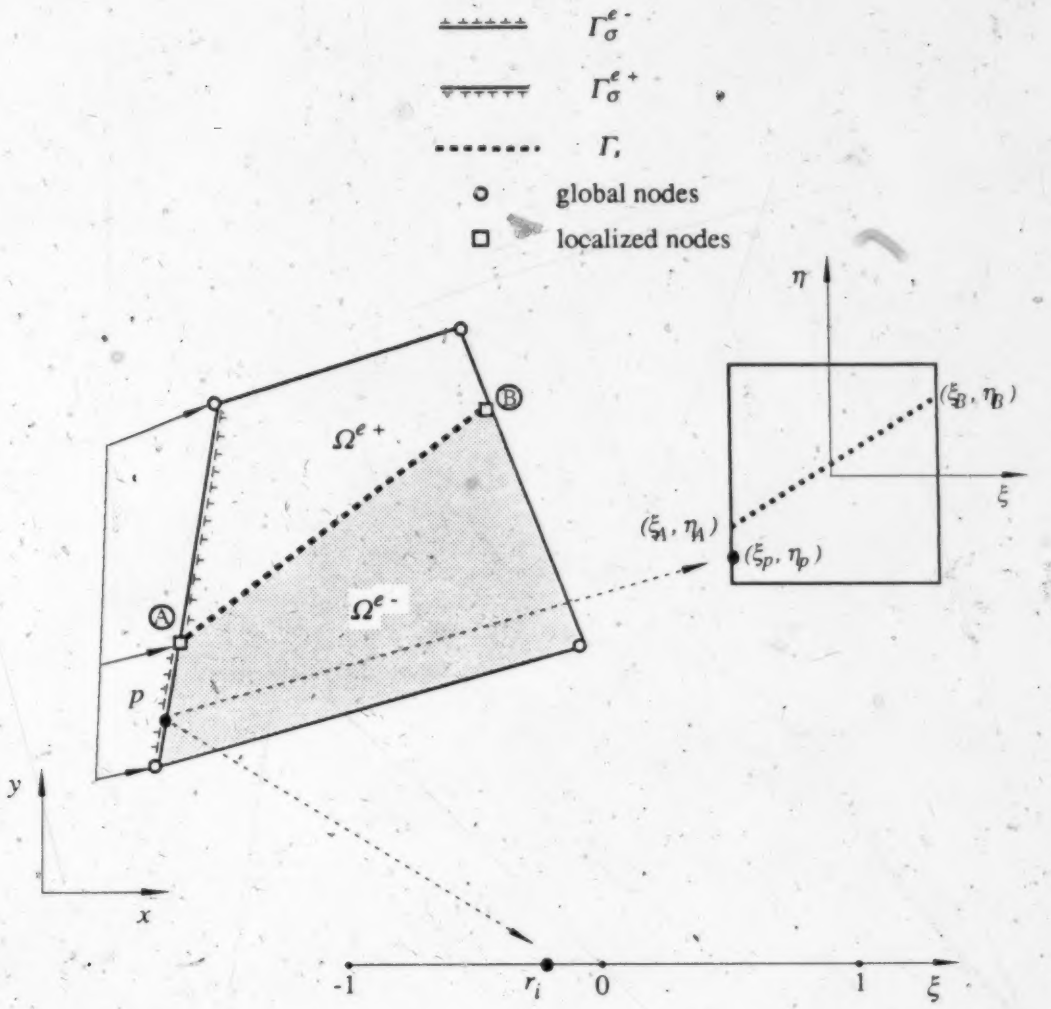

Figure B.5 Integration of loads along a discontinuous edge